npj Precision Oncology

https://doi.org/10.1038/s41698-026-01338-9

Article in Press

COL3A1^{high} cancer-associated fibroblasts orchestrate metabolic and immune microenvironments to confer chemoresistance in breast cancer

Received: 29 July 2025

Accepted: 12 February 2026

Cite this article as: Jiang, P., Li, X., Wang, Z. *et al.* COL3A1^{high} cancer-associated fibroblasts orchestrate metabolic and immune microenvironments to confer chemoresistance in breast cancer. *npj Precis. Onc.* (2026). https://doi.org/10.1038/s41698-026-01338-9

Peicheng Jiang, Xinyan Li, Ziyi Wang, Su Li, Yonglian Huang, Ye-Xiong Li, Yuqiong Chen & Xiangyu Sun

Title page

COL3A1^{high} Cancer-associated Fibroblasts Orchestrate Metabolic and Immune Microenvironments to Confer Chemoresistance in Breast Cancer

Peicheng Jiang[1#], Xinyan Li[2#], Ziyi Wang[3], Su Li[4], Yonglian Huang[5], Ye-Xiong Li[1*], Yuqiong Chen[6#,*], Xiangyu Sun[5*]

[#] These authors contributed equally to this work.
[*] CORRESPONDENCE
Ye-Xiong Li[*]
yexiong112@163.com
Yuqiong Chen[*]
cosmoscyq@163.com
Xiangyu Sun[*]
sxycmu@163.com

Affiliations
[1] State Key Laboratory of Molecular Oncology and Department of Radiation Oncology, National Cancer Center/National Clinical Research Center for Cancer/Cancer Hospital, Chinese Academy of Medical Sciences and Peking Union Medical College, Beijing, China.
[2] Center for Precision Cancer Medicine & Translational Research, Tianjin Medical University Cancer Institute and Hospital, National Clinical Research Center for Cancer, Key Laboratory of Cancer Prevention and Therapy, Key Laboratory of Breast Cancer Prevention and Therapy, Tianjin Medical University, Ministry of Education, Tianjin's Clinical Research Center for Cancer, Tianjin, China
[3] Department of Surgical Oncology and General Surgery, First Hospital of China Medical University, Shenyang, Liaoning Province, 110001, China
[4] Department of Cardiology, Zhongshan Hospital, Fudan University, Shanghai Institute of Cardiovascular Diseases, China
[5] Department of Breast Surgery, Cancer Hospital of China Medical University, Liaoning Cancer Hospital and Institute, Shenyang, China
[6] Department of Cardiology, The Affiliated Suzhou Hospital of Nanjing Medical University, Suzhou Municipal Hospital, Gusu School, Nanjing Medical University, Suzhou 215000, China

Abstract

Chemoresistance remains a critical challenge in breast cancer (BC) treatment. By integrating multi-omics (single-cell, spatial, and bulk transcriptomics) with clinical validation, we identified a specific $COL3A^{high}$ CAF subset that drives BC chemoresistance. Mechanistically, these CAFs undergo lipid metabolic reprogramming, secreting excess oleic acid via SCD. This oleic acid binds to ENO1 on tumor cells, activating the PI3K/Akt pathway and inhibiting chemotherapy-induced apoptosis. Simultaneously, $COL3A^{high}$ CAFs orchestrate an immunosuppressive niche by recruiting regulatory T cells and impairing cytotoxic $CD8^{+}$ T cells. Our findings establish $COL3A^{high}$ CAFs as key mediators of resistance through metabolic symbiosis and immune evasion. The strong correlation between $COL3A^{high}$ CAF abundance and clinical poor response highlights their potential as both predictive biomarkers and therapeutic targets to overcome chemoresistance in BC patients.

Keywords: Breast cancer, Chemoresistance, Cancer-associated fibroblasts, Immune evasion, Tumor microenvironment.

1. Introduction

Breast cancer (BC) is the malignancy with the highest incidence rate in women worldwide and constitutes a major driver of cancer-associated deaths in the female population[1]. Chemotherapy remains a cornerstone of BC treatment, significantly improving survival and reducing recurrence risk[2]. However, chemoresistance severely limits therapeutic efficacy and contributes to disease relapse[3]. Although extensive researches have focused on tumor cell-intrinsic mechanisms, such as drug efflux activation, apoptotic evasion, and metabolic reprogramming[4], accumulating evidence substantiate the significance of the tumor microenvironment (TME) as a key mediator of chemoresistance in BC[5].

As an essential constituent of TME, cancer-associated fibroblasts (CAFs) exhibit significant functional heterogeneity, playing both pro-tumorigenic and anti-tumorigenic roles[6]. Despite progress in elucidating these dual functions, therapeutic strategies targeting CAFs have yielded inconsistent results in preclinical and clinical studies[7], largely due to gaps in comprehending their functional diversity[8]. Emerging evidence highlights that metabolic reprogramming is a critical driver of chemoresistance[9], with CAFs actively contributes to this process by remodeling tumor cell metabolism to foster metabolic symbiosis within the TME[10]. Additionally, CAFs promote tumor cell survival under stress through cytokine-mediated suppression of apoptosis in various cancers, and further investigations are required to clarify thespecific mechanisms involved[11–13].

In the TME, dysregulated collagen deposition and remodeling play crucial roles in facilitating tumor progression and metastasis[8,14]. As the most abundant components of

extracellular matrix (ECM), collagens exhibit diverse structural and functional characteristics that are increasingly recognized for their impact on cancer progression and therapeutic resistance[14-17]. Beyond structural support, collagens contribute to immune evasion and act as physical barriers against drug penetration[18,19]. CAFs serve as the dominant collagen producers in tumors, with their collagen-secreting capacities varying across subtypes and leading to distinct modifications of TME[20]. Type III collagen (COL3A1) has emerged as a pivotal player due to its overexpression in various cancers, correlating with advanced tumor stages and unfavorable prognosis[21]. Paradoxically, emerging evidence suggests COL3A1 may also exert tumor-suppressive effects by regulating ECM physical properties including stiffness and topology[22]. Notably, a recent study indicated a direct correlation between elevated COL3A1 expression and cisplatin resistance in lung cancer[23].

Although both CAFs and collagens play pivotal roles in chemoresistance, the role of CAF subtypes with distinct collagen-secreting profiles remains poorly understood, primarily due to the inherent heterogeneity of CAFs and the diverse functional roles of collagens within the TME. Given the context-specific activity of COL3A1 and its predominant production by CAFs, differences in collagen production across CAF subtypes may significantly regulate chemoresistance. Therefore, elucidating how CAF subtypes with differential COL3A1-secreting capacities modulate chemoresistance is essential for deepening our understanding of TME-mediated regulation of therapeutic resistance.

In this study, we conducted a comprehensive analysis integrating bulk microarray,

single-cell RNA sequencing, and spatial transcriptomic analyses, supplemented by experimental validation and clinical correlation studies. We identified a subset of COL3A1^{high} CAFs that critically mediate chemoresistance in BC. Mechanistically, COL3A1^{high} CAFs promote chemoresistance through cytokine secretion and metabolic reprogramming of lipid pathways, which ultimately reshape the immunosuppressive tumor niche and inhibit apoptosis of tumor cells to mediate chemoresistance in BC.

2. Results

2.1 The response of BC to chemotherapy is significantly associated with CAFs, with COL3A1 identified as a key mediator.

We performed immune infiltration analysis on BC patients receiving neoadjuvant chemotherapy. Immune infiltration analysis, assessed by different methods across multiple datasets, indicated a close correlation between CAFs and chemotherapy response (Figure 1A-D, Supplementary Figure 1A-D). To explore the relationship between the collagen family and CAFs, we evaluated correlations between collagen genes and CAF abundance, as well as their relationship with chemosensitivity (Figure 1E-F). Among the top six genes most correlated with both CAF infiltration and chemotherapy response, COL1A2 and COL3A1 were identified as overlapping candidate (Figure 1G). Further validation using GDSC drug sensitivity data revealed that COL3A1 exhibited stronger correlation with drug sensitivity of BC than COL1A2 (Figure 1H-I). Survival analysis revealed that elevated COL3A1 expression was

significantly associated with poorer overall survival (OS) and recurrence-free survival (RFS) in all patients (Figure 1J-K) or those receiving chemotherapy (Figure 1L-M). Analysis of tumor hallmarks in BC patients demonstrated distinct in multiple oncogenic characteristics based on COL3A1 expression status (Figure 1N). Subsequently, GSEA identified significant enrichment of chemoresistance-related pathways, including epithelial-mesenchymal transition (EMT) and hypoxia that were significantly enriched in COL3A1-high tumors, strongly implicating COL3A1 as a key mediator of chemoresistance (Figure 1O). Overall, integrated analyses revealed that CAF infiltration is closely associated with chemotherapy response in BC, with COL3A1 emerging as a key collagen gene related to both CAF abundance and chemoresistance.

2.2 COL3A1^{high} CAFs influence BC chemotherapy efficacy

In order to dissect the cellular contributors underlying chemoresistance of BC, we performed scRNA-seq analysis and identified sub-clusters from scRNAseq data (Figure 2A, Supplementary Figure 1E). The CAF population was further stratified into three subsets according to COL3A1 expression levels (Figure 2B). Using the Scissor algorithm, we established a robust association between specific cell subtypes and chemosensitivity (Figure 2C, Supplementary Figure 1F). Quantitative assessment revealed a significantly increased proportion of chemoresistant tumor cells in post-treatment samples compared to treatment-naïve specimens, validating the reliability of the Scissor analysis (Figure 2D). Extending this analysis to CAFs, we observed that both chemoresistant CAFs and COL3A1^{high} CAFs were substantially enriched in patients who had received chemotherapy (Figure 2E). Notably, the COL3A1^{high} subset

constitutes a markedly higher proportion of chemoresistance-associated CAFs compared to the COL3A1^{low} and COL3A1^{neg} subsets among CAFs (Figure 2F). Consistently, differential gene expression analysis further confirmed that COL3A1 was significantly upregulated in chemoresistance-associated CAFs (Figure 2G). Together, these results provide compelling evidence that chemotherapy induces the expansion of a COL3A1^{high} CAF subset that plays a pivotal role in promoting chemoresistance.

AUCell scoring demonstrated that COL3A1^{high} CAFs displayed enhanced EMT and oxidative phosphorylation (Figure 2H). Chemoresistant tumor cells exhibited impaired drug metabolism and displayed biological signatures remarkably similar to COL3A1^{high} CAFs (Figure 2I, Supplementary Figure 2A). GSEA further characterized COL3A1^{high} CAFs with activation of ECM organization and response to TGF-β, as well as downregulated immune responses (Supplementary Figure 2B). Ro/e analysis comparing treatment-naïve and chemotherapy-treated cohorts demonstrated significant enrichment of: COL3A1^{high} CAFs, chemoresistant tumor cell populations and immunosuppressive cells (particularly Tregs) were enriched in patients receiving chemotherapy, while CD8^{+} IFNG were depleted in these patients (Figure 2J, Supplementary Figure 2C).

Trajectory analysis of CAFs indicated that COL3A1^{high} CAFs were positioned at the later stages of differentiation. Furthermore, treated patients exhibited a higher proportion of these COL3A1^{high} CAFs (Figure 2K, S2D). Analysis of COL3A1 expression revealed a significant positive correlation with pseudotime (Figure S2E). Chemoresistant CAFs were also predominantly observed at later differentiation stages,

indicating that resistance traits are acquired during CAF differentiation (Supplementary Figure2F). Pseudotime trajectory analysis of EMT progression demonstrated a positive correlation between EMT activation (Supplementary Figure 2G). In cellular assays, we observed that BC cells co-cultured with CP-H172^{shCOL3A1} exhibited upregulation of epithelial marker E-cadherin and downregulation of mesenchymal markers (Snail, N-cadherin, and Vimentin). Upon PTX treatment, the inhibitory effect of COL3A1 knockdown on EMT progression became more pronounced (Figure 2L, Supplementary Figure 2H-J). To further validate the functional impact of COL3A1^{high} CAFs on the EMT of BC cells, we performed both in vitro and in vivo assays. Transwell migration assays showed that tumor cells co-cultured with CP-H172^{shNC} CAFs exhibited significantly enhanced migratory capacity compared with those co-cultured with CP-H172^{shCOL3A1} CAFs (Figure 2M-N; Supplementary Figure S2K-2L). Consistently, in a mouse lung metastasis model, CP-H172^{shNC} CAFs markedly promoted BC cell metastasis in vivo compared with CP-H172^{shCOL3A1} CAFs (Figures 2O–Q).

To assess the impact of COL3A1^{high} CAFs on chemoresistance, MDA-MB-231 and MDA-MB-453 were cocultured with either CP-H172^{shCOL3A1} or CP-H172^{shNC} and treated with PTX. Compared to coculture with CP-H172^{shNC}, coculture with CP-H172^{shCOL3A1} resulted in decreased IC_{50} (Figure 2R, Supplementary Figure 2M) and elevated proliferation rate in response to paclitaxel treatment (Figure 2S, Supplementary Figure 2N). Herein, integrated single-cell transcriptomic and functional studies demonstrate that chemotherapy drives the enrichment of a distinct COL3A1^{high} CAF subpopulation, which orchestrates chemoresistance through ECM remodeling and

immune evasion.

2.3 Oleic Acid metabolism mediates chemoresistance in COL3A1^{high} CAFs

Considering the pivotal contribution of metabolic reprogramming to chemoresistance and our observation of enhanced oxidative phosphorylation in both chemoresistant tumor cells and COL3A1^{high} CAFs, we conducted systematic metabolic profiling analysis (Figure 3A, Supplementary Figure 3A). The analysis revealed that resistant tumor cells exhibited a distinct metabolic phenotype characterized by significantly upregulated oxidative phosphorylation, downregulated glycolysis, and enhanced fatty acid metabolism. This metabolic shift is consistent with previous reports. In chemoresistant tumor cells, we observed arachidonic acid (AA) production (Supplementary Figure 3B), consistent with established mechanisms of therapy resistance. However, COL3A1^{high} CAFs exhibited no significant association with ELOVL5-mediated AA synthesis (Supplementary Figure 3C). Instead, COL3A1 expression was strongly correlated with stearoyl-CoA desaturase (SCD), the key enzyme regulating oleic acid synthesis in CAFs (Figure 3B). Sun et al. demonstrated through molecular docking and experimental validation that ENO1 functions as a cell-surface receptor for oleic acid in tumor cells[24]. And our analysis revealed that chemoresistant tumor cells exhibited upregulated expression of oleic acid receptor ENO1 (Figure 3C) and suppressed apoptosis (Figure 3D). Knockdown of COL3A1 in CP-H172 significantly downregulated SCD expression within CP-H172 at mRNA and protein levels, and concurrently reduced ENO1 levels in co-cultured BC cells (Figure 3F-F, Supplementary Figure 3E-F). Meanwhile, BODIPY staining and TEM revealed a

substantial decrease in lipid droplet accumulation in co-cultured BC cells following COL3A1 depletion (Figure 3G, 3H).

Considering the established role of PI3K/Akt signaling in oleic acid–mediated regulation of apoptosis, we examined the relationship between COL3A1 expression and key components of the PI3K/Akt pathway. The results showed that phosphorylation levels of JAK, PI3K, and AKT were reduced in MDA-MB-231 and MDA-MB-453 cells co-cultured with CP-H172^{shCOL3A1}, indicating impaired PI3K/AKT pathway activation. This suppression of PI3K/AKT pathway was further enhanced upon PTX treatment (Figure 3I-—J, Supplementary Figure S3G-H).

Given the observed correlations between COL3A1 expression and the levels of SCD and ENO1, as well as the association between oleic acid content and the functional roles of SCD and ENO1, we hypothesized that oleic acid serves as a critical mediator linking COL3A1^{high} CAFs to ENO1 expression and activation of the PI3K/AKT pathway in BC cells. To test this hypothesis, we performed additional functional assays. The results demonstrated that oleic acid treatment markedly increased SCD expression in CP-H172 cells and ENO1 expression in BC cells (Figure 3K-L, Supplementary Figure 3I). Moreover, oleic acid activated the PI3K/AKT signaling pathway in BC cells, whereas knockdown of ENO1 attenuated oleic acid–induced PI3K/AKT pathway activation (Figure 3M-N, Supplementary Figure 3J-K). Taken together, these findings suggest that COL3A1^{high} CAFs promote ENO1 expression in BC cells via the secretion of OA, which subsequently triggers the activation of the PI3K/AKT signaling axis.

Consistently, the results of flow cytometry revealed a significant increase in

apoptosis in BC cells co-cultured with CP-H172^{shCOL3A1} following PTX treatment (Figure 3O-P, Supplementary Figure 3L-M). Metabolic profiling uncovered a coordinated metabolic reprogramming axis between chemoresistant tumor cells and COL3A1^{high} CAFs. COL3A1 promotes a chemoresistant microenvironment through regulating oleic acid synthesis and PI3K/Akt signaling.

2.4 Interaction of COL3A1^{high} CAFs with cells in the TME

Due to the significant role of intercellular interactions in tumor progression, we further evaluated the differential interactions of COL3A1^{high} and COL3A1^{low} CAFs with diverse cell types of TME. At the global level, substantial differences in signal output were detected among various cell types, suggesting that intercellular communication activity is highly cell-specific (Figure 4A). In addition to the significantly higher LAMININ and FN1 signaling pathways associated with EMT in COL3A1^{high} CAFs compared to COL3A1^{low} CAFs, the signal intensity of CD39 and CD99 pathways was notably stronger in COL3A1^{high} CAFs than in COL3A1^{low} CAFs (Figure 4B, Supplementary Figure 4A), whereas pathways like CXCL, ANGPTL, and COMPLEMENT showed the opposite trend. And COL3A1^{high} CAFs had stronger input and output signals, indicating more active communication between COL3A1^{high} CAFs and other cells (Supplementary Figure 4B). Further ligand-receptor interaction analysis revealed that COL3A1^{high} CAFs interact with multiple cell types via the CD39_TMIGD3 axis in the CD39 signaling pathway, whereas such interactions were absent in COL3A1^{low} CAFs (Supplementary Figure 4C). In the CD99 pathway, the interaction between CD99_PILRA ligands was stronger in COL3A1^{high} compared to

COL3A1^{low}(Figure 4C).

Our analysis of CAF-tumor cell interactions revealed COL3A1^{high} CAFs exhibited denser and more complex signaling networks with chemoresistant tumor cells, reinforcing their role in promoting chemoresistance (Figure 4D). COL3A1^{high} CAFs exhibited stronger capacity to drive EMT and immunosuppression than COL3A1^{low} CAFs through enhanced ligand-receptor signaling (e.g., THBS2-CD47, MDK-NCL) (Figure 4E, Supplementary Figure 4D-E). Correlation profiling of CAF signatures demonstrated strong co-expression of COL3A1 with FN1, CD99, MDK and THBS2 (Figure 4F). Knockdown of COL3A1 in CP-H172 cells led to reduced expression of CD39 and CD99, accompanied by a marked decrease in the secretion of THBS2, MDK, and FN1(Figure 4G, Supplementary Figure 4F-G). These results imply that COL3A1^{high} CAFs drive EMT and foster an immunosuppressive niche MDK-NCL and THBS2-CD47 pathways to promote chemoresistance.

2.5 Inference of transcription factors regulating COL3A1^{high} CAFs

To identify transcription factors associated with chemotherapy response, we integrated pySCENIC analysis with variance decomposition, pinpointing transcription factors that were both cell-type specific and treatment-induced (Supplementary Figure 5A). Through analysis of COL3A1^{high} CAFs in post-treatment samples, we found that DBX2 was significantly upregulated (Figure 5A-B). To further investigate the underlying mechanisms of BC chemoresistance, differential transcriptomic analysis of treated versus naive COL3A1^{high} CAFs showed that the TNFα/NF-κB pathway was the most significantly enriched in the treated group (Figure 5C). We next sought to identify

the upstream transcription factors regulating the TNFα/NF-κB pathway of COL3A1^{high} CAFs (Figure 5D). SPI1 and FOS are identified as key TFs of this pathway in COL3A1^{high} CAFs, all of which were upregulated post-treatment (Figure 5D-E). Finally, by assessing expression across CAF subsets and tumor cell subsets, we found that SPI1 and DBX2 expression was highly specific to COL3A1^{high} CAFs, implicating them as key potential mediators of chemoresistance in this celltype (Figure 5F, Supplementary Figure 5B). A TF signature score was generated to functionally link SPI1 and DBX2 to chemoresistance in COL3A1^{high} CAFs. Notably, chemoresistant CAFs showed a significantly higher score than other CAF subsets, indicating that the transcriptional programs regulated by SPI1/DBX2 are positively correlated with chemoresistance (Figure 5G). Taken together, the transcription factors SPI1 and DBX2 are key regulators that may mediate chemoresistance in COL3A1^{high} CAFs.

2.6 Spatial validation of COL3A1^{high} CAFs-mediated chemoresistance

To map spatial distributions of CAFs and tumor cells in BC, we performed spatial transcriptomics analysis. COL3A1 expression patterns across tissues are depicted in Figure 6A. Our analysis revealed a strong concordance between COL3A1^{high} CAFs abundance and COL3A1 expression, with chemoresistant tumor cells exhibiting closer proximity to COL3A1^{high} CAFs (Figure 6B). Co-localization probability analysis further demonstrated distinct interaction patterns between COL3A1^{high} and COL3A1^{low} CAFs (Figure 6C). Spatial transcriptomic analysis across four samples confirmed that COL3A1^{high} CAFs exhibited significantly stronger interactions with chemoresistant tumor cells compared to chemosensitive cells (Figure 6D). Additionally, COL3A1^{high}

CAFs showed enhanced interactions with immunosuppressive Tregs, while their interactions with cytotoxic $CD8^{+}IFN\text{-}\gamma^{+}$ T cells were markedly reduced (Supplementary Figure 5C-D). To validate the findings from spatial transcriptomics, mxIF staining was employed to examine the co-localization of CAFs and immune cells in tissue samples from patients with different chemoresistance. The analysis revealed that, compared to chemoresistant patients, chemosensitive ones had significantly lower infiltration levels of both $COL3A1^{high}$ CAFs and Tregs, alongside a markedly increased abundance of $CD8^{+}$–IFN-γ T cells (Figure 6E-F). Beyondcell scoring for chemotherapy sensitivity revealed that chemoresistant tumor cells had significantly lower drug sensitivity than chemosensitive cells, suggesting the robustness of our cell classification. Furthermore, $COL3A1^{high}$ CAFs were found to exert negative regulatory effects on chemosensitivity (Figure 6E, Supplementary Figure 5E). Collectively, these spatial and drug sensitivity analyses suggest that $COL3A1^{high}$ CAFs foster a chemoresistant niche through direct spatial interactions with tumor cells.

2.7 $COL3A1^{high}$ CAFs enhance predictive accuracy for chemoresistance

To assess the clinical relevance of the $COL3A1^{high}$ CAFs, we performed deconvolution analysis to estimate their proportions in bulk transcriptomic data. As anticipated, chemoresistant tumor cells were significantly less abundant in chemosensitive patients (Figure 7A-B). Notably, $COL3A1^{high}$ CAFs abundance was also significantly lower in chemosensitive patients than chemoresistant patients (Figure 7C-D). Conversely, $COL3A1^{low}$ CAFs and chemosensitive tumor cells were enriched in chemosensitive patients (Supplementary Figure 6A-B). And there was significantly

negative correlation between chemosensitive tumor cells and COL3A1^{high} CAFs (Figure 7E-F), suggesting a functional divergence between COL3A1^{high} CAFs and COL3A1^{low} CAFs in chemotherapy response. Next, we evaluated the predictive power of tumor cell subtypes for treatment response. A ROC (receiver operating characteristic) curve constructed using the abundance of chemoresistant tumor cells alone yielded AUC (Area Under Curve) values of 0.762 and 0.715 in the two datasets, respectively (Figure 7G, Supplementary Figure 6C). Importantly, when a composite model was built by incorporating the abundance of COL3A1^{high} CAFs, the AUC values significantly improved (Figure7H, Supplementary Figure 6D). In contrast, combining chemoresistant tumor cells with COL3A1^{low} CAFs did not lead to a significant increase in AUC (Figure 7I, S5E). These findings further highlight the correlation between COL3A1^{high} CAFs and chemoresistance in BC.

To examine the relationship between COL3A1^{high} CAFs and patient prognosis, we performed survival analysis. A lower abundance of COL3A1^{high} CAFs was significantly correlated with OS and RFS (Figure 7J, 7K). Furthermore, analysis of PAM50 molecular subtypes revealed that chemosensitive basal-like tumors dominated in COL3A1^{high} CAFs low-abundance groups, whereas chemotherapy-resistant luminal A tumors prevailed in COL3A1^{high} CAF high-abundance groups (Figure 7L). Expanding our investigation beyond breast cancer, we evaluated the prognostic significance of COL3A1^{high} CAFs abundance in pan-cancer. It revealed that high COL3A1^{high} CAFs levels correlated with adverse clinical outcomes in the majority of cancer types (Figure 7M-O, Supplementary Figure 6F-H). This association with poor prognosis was

consistent with the pattern identified in breast cancer.

Taken together, COL3A1^{high} CAFs were negatively associated with chemosensitivity and patient prognosis. Incorporating COL3A1^{high} CAFs abundance into predictive models significantly improves the accuracy of chemotherapy response prediction, further supporting their key role in mediating chemoresistance in BC. The detrimental prognostic impact of COL3A1^{high} CAFs extended beyond BC to most solid tumors, indicating conserved protumorigenic functions across pan-cancer.

2.8 COL3A1^{high} CAFs mediate chemoresistance in BC *in vivo*

To further evaluate the clinical relevance of COL3A1^{high} CAFs in BC chemoresistance, MDA-MB-231 cells were subcutaneously co-injected with either CP-H172^{NC} or CP-H172^{shCOL3A1} (Figure 8A). Tumor growth status demonstrated that COL3A1 knockdown in CP-H172 significantly inhibited tumor growth, indicating an enhanced cytotoxic effect of PTX (Figure 8B-E). IHC analysis of tumor sections demonstrated significantly decreased levels of SCD and ENO1 in tumors treated with CP-H172^{shCOL3A1}, providing evidence that COL3A1 plays a crucial role in regulating molecular characteristics associated with chemoresistance (Figure 8F, 8G). To clinically validate these findings, we analyzed pre-treatment biopsies from 72 BC patients who received neoadjuvant chemotherapy. IHC analysis revealed a strong positive correlation between COL3A1 and SCD or ENO1 expression (Figure 8H). Notably, non-complete response (non-CR) patients exhibited significantly higher levels of COL3A1, SCD, and ENO1 compared to CR patients (Figure 8I-L). The patients were further stratified into COL3A1^{High} and COL3A1^{Low} groups based on IHC scoring, and

survival analysis revealed that the COL3A1^{High} group had significantly worse prognosis (Figure 8M). Altogether, *in vivo* experiments and clinical cohort analyses consistently demonstrated that COL3A1^{high} CAFs promote chemoresistance in BC, highlighting their prognostic value and therapeutic potential.

3. Discussion

Chemoresistance remains a clinical challenge in BC treatment, substantially undermining therapeutic efficacy with intrinsic and acquired resistance mechanisms. While CAFs are recognized as architects of the desmoplastic TME, the functional specialization of CAF subsets in chemoresistance remains poorly defined[25,26]. Through integrated multi-omics profiling and functional validation, our study reveals that COL3A1^{high} CAFs drive chemoresistance through a dual-axis mechanism including metabolic symbiosis mediated by lipid reprogramming and TME remodeling via immunosuppressive niche formation, offering potential targets for therapeutic intervention (Figure 9).

Collagen, a key extracellular matrix component, exhibits a strong correlation with chemotherapy resistance. In the TME, fibroblasts serve as the main source of collagen secretion. Notably, various CAF subpopulations demonstrate differential collagen-secreting capacities, which contribute to their diverse functional roles within the TME[27]. COL11A1[28] Through integrated analysis of multiple datasets on immune infiltration and chemotherapy response, we identified COL3A1 as the collagen family member most strongly associated with chemotherapy sensitivity in BC. Through integrated analysis of multiple

datasets on immune infiltration and chemotherapy response, we identified COL3A1 as the collagen family member most strongly associated with chemotherapy sensitivity in BC. Functional profiling indicated that COL3A1^{high} CAFs were linked to the activation of extracellular matrix structure and TGF-β signaling pathway, both of which have been implicated in the promotion of chemoresistance[29, 30]. Moreover, the EMT pathway, a key contributor to chemotherapy resistance, exhibited markedly increased activity in both COL3A1^{high} CAFs and chemoresistant tumor cells[33]. Additionally, chemoresistant tumor cells exhibited enhanced anti-apoptotic abilities, which were significantly correlated with COL3A1^{high} CAFs.

Metabolic reprogramming is increasingly recognized as a key mechanism of chemoresistance[32]. Metabolic analysis revealed a significant upregulation of oxidative phosphorylation in both chemoresistant tumor cells and COL3A1high CAFs, indicating that metabolic reprogramming in CAFs contributes to the development of tumor cell chemoresistance. Tumor cells respond to chemotherapy-induced metabolic stress by enhanced lipid droplet biogenesis, de novo fatty acid synthesis, and increased fatty acid oxidation for cytoprotective mechanism against chemotherapeutic damage, highlighting the crucial role of lipid metabolism in the development of chemoresistance[33]. Under certain conditions, tumor cells adaptively utilize lipid metabolic reprogramming of surrounding cells in the TME to fulfill their elevated bioenergetic requirements[34]. And a recent study reported that interactions between tumor cells and neutrophils through the arachidonic acid metabolism pathway modulates the immunometabolic profile of the TME, thereby facilitating

chemoresistance in BC[35]. Our analysis of lipid metabolism revealed that chemoresistant tumor cells exhibited more active lipid metabolism. Furthermore, COL3A1^{high} CAFs underwent metabolic reprogramming, suppressing their own lipid metabolism while upregulating oleic acid synthesis through increased SCD expression. Studies have reported that inhibition of SCD suppressed gastric and colorectal carcinogenesis, and enhanced temozolomide sensitivity in glioblastoma[33-38]. The experimental results validated that COL3A1 knockdown in CAFs resulted in a significant reduction in SCD expression and oleic acid production, suggesting the correlation between COL3A1 and SCD expression in CAFs. Previous studies have shown that oleic acid interacted wtih ENO1 and activated the PI3K/Akt signaling pathway of tumor cells, thereby promoting tumor growth[24]. In this study, we have characterized a novel metabolic crosstalk within the TME that drives chemoresistance in BC. Our findings demonstrate that the resistance to agents like paclitaxel is significantly orchestrated by CAF-derived metabolic reprogramming. Crucially, our data reveal that the intracellular interaction between COL3A1^{high} CAFs-derived OA and ENO1 of tumor cells serves as a molecular switch to activate the PI3K/Akt signaling axis. This activation leads to a profound suppression of pro-apoptotic signaling, thereby establishing a higher threshold for chemotherapy-induced cell death. The significance of this COL3A1^{high} CAFs-OA-PI3K/Akt axis is further underscored by our observation that COL3A1 knockdown in CAFs effectively blunts PI3K/Akt phosphorylation and restores apoptotic sensitivity in co-cultured tumor cells. Because taxane-based regimens have long constituted the backbone of BC chemotherapy and are widely recommended in major clinical

guidelines. Paclitaxel was selected as the representative chemotherapeutic agent for our in vitro and in vivo experiments to validate the mechanism by which COL3A1^{high} CAFs promote chemoresistance in breast cancer[39,40]. In our clinical cohorts, we observed a strong correlation between elevated levels of COL3A1, SCD, and ENO1 expression in tumor tissues and chemotherapy resistance, further supporting this hypothesis.

As one of the most abundant non-immune cell types in the TME, CAFs extensively interact with other cells to play a pivotal role in promoting tumor chemoresistance and immune evasion[5]. Cell-cell communication analysis revealed that COL3A1^{high} CAFs displayed significantly enhanced intercellular signaling, particularly through pathways involving CD39, CD99, MDK, and THBS2. These molecular interactions facilitate Treg cell recruitment while impairing $CD8^+$ T cell cytotoxicity, thereby fostering an immunosuppressive niche that compromises anti-tumor immunity[41-43]. Spatial transcriptomics further revealed that COL3A1^{high} CAFs were spatially closer to chemoresistant tumor cells and Treg cells, emphasizing their spatial proximity and functional interaction. Integrative analysis of bulk transcriptome demonstrated that COL3A1^{high} CAFs significantly enhanced the predictive efficacy for chemoresistant cells and were strongly correlated with poor patient survival outcomes. These findings provide validation for the critical role of COL3A1^{high} CAFs in modulating chemotherapy sensitivity in BC. Nevertheless, a limitation of this study is the use of an immunodeficient mouse model, which does not fully recapitulate the complex interactions between CAFs and immune cells. As a result, the contribution of CAF–immune crosstalk to treatment response may not be fully captured in vivo. However,

analyses of clinical specimens using IHC and mxIF, in conjunction with treatment response data, validated the associations between COL3A1^{high} CAFs, immune cell infiltration, and chemotherapy sensitivity, thereby partially mitigating this limitation. Additionally, COL3A1^{high} CAFs predicted poorer survival outcomes not only in BC but across multiple solid tumor types, suggesting evolutionarily conserved tumor-promoting mechanisms in diverse malignancies. While our multi-omics approach offers robust mechanistic insights, the clinical cohort size in this study was limited. Larger, prospective studies are needed to validate COL3A1 and SCD of CAFs as reliable biomarkers of chemoresistance.

In conclusion, this study systematically reveals that COL3A1^{high} CAFs orchestrate chemoresistance through dual mechanisms of metabolic and immunomodulatory modulation. Our study reveals novel aspects of CAF heterogeneity in chemoresistance and offer a solid theoretical foundation for the development of targeted therapies against COL3A1^{high} CAFs, with significant clinical translational potential.

4. Methods

4.1 Data Sources and Preprocessing

Publicly available transcriptomic and clinical datasets were leveraged to investigate gene expression profiles in BC. Microarray data from cohorts GSE20194 and GSE25066 were achieved from the Gene Expression Omnibus (GEO) database. METABRIC gene expression and clinical information were accessed through the cBioPortal platform (https://www.cbioportal.org/). Single-cell RNA sequencing

(scRNA-seq) data from 26 BC patients were downloaded from the Broad Institute's Single-Cell Portal (https://singlecell.broadinstitute.org/single_cell/study/SCP1039). This study utilized spatial transcriptomics datasets retrieved from the Zenodo repository (DOI: 10.5281/zenodo.4739739). Pan-cancer gene expression data and patient survival information were retrieved from The Cancer Genome Atlas (TCGA) via its Genomic Data Commons portal. Patients with incomplete drug response records or missing survival information were excluded from subsequent analyses.

4.2 Single-Cell RNA-seq Processing and Cell Annotation

Quality control of scRNA-seq data was performed using established criteria. Cells with fewer than 200–250 unique molecular identifiers (UMIs) or with mitochondrial gene content exceeding 20% were excluded. The remaining data underwent log-normalization, and the top 2000 genes exhibiting high variability were chosen for principal component analysis (PCA), with the initial 30 principal components used for clustering via FindNeighbors and FindClusters functions. Cell identity was determined using canonical marker genes and published annotation references.

4.3 Advanced Analysis of Bulk and Single-Cell RNA-seq Datasets

Gene expression differences were assessed through statistical analysis using the limma R package, and functional enrichment was performed through Gene Set Enrichment Analysis (GSEA) and Gene Set Variation Analysis (GSVA), using gene sets from the

Molecular Signatures Database (MSigDB) and Gene Ontology. Immune infiltration estimations were calculated using the EPIC and MCPcounter algorithms.

To investigate spatial preferences of specific cell subsets, the ratio of observed to expected (Ro/e) values was calculated[44]. Cellular metabolic activity was assessed using the scMetabolism package, while AUCell was applied to score gene set activity at the single-cell level.

To reduce data sparsity and enhance interpretability, similar single cells were aggregated into metacells.

4.4 Cell–Cell Communication Analysis Using CellChat

Cell–cell communication analysis was performed using the CellChat (v1.6.1)[45]. Single-cell gene expression data were first processed to infer intercellular signaling networks based on the curated ligand–receptor interaction database implemented in CellChat. Communication probabilities for each ligand–receptor pair were calculated using the computeCommunProb function, which models signaling strength by integrating the average expression levels of ligands and receptors in sender and receiver cell populations, respectively. To specifically investigate differences in signaling interactions, the inferred communication network was subset using the subsetCommunication function with the sources.use parameter, restricting the analysis to certain populations as signal senders. Communication probabilities associated with

selected ligand – receptor pairs and signaling pathways were then extracted and visualized to highlight differential interaction patterns.

4.5 Combined Analysis of Single-Cell and Bulk RNA-seq Data

To integrate scRNA-seq with bulk RNA-seq datasets, Scissor and BayesPrism algorithms were employed. To identify specific cell subpopulations associated with chemoresistance, we applied the Scissor algorithm[46] to integratively analyze scRNA-seq and bulk RNA-seq data. Briefly, clinical phenotypic information derived from GSE20194[47] with annotated chemotherapy response was used as a reference to guide the prioritization of cells within the scRNA-seq dataset. Through this approach, individual cells were ranked based on their transcriptional relevance to the chemoresistance phenotype observed at the bulk level, enabling the identification of cell subsets that are most strongly associated with treatment response. BayesPrism was used to deconvolve bulk data by referencing scRNA-seq profiles, enabling estimation of cell-type proportions and context-specific gene expression[48]. The phenotype-relevant cell populations identified by Scissor were further validated through independent integration with the GSE25066 and METABRIC datasets using BayesPrism.

4.6 Prediction of Drug Sensitivity

Drug responsiveness was estimated using the oncoPredict package, which incorporates pharmacogenomic signatures from the Genomics of Drug Sensitivity in Cancer (GDSC) resource. For spatial transcriptomics data, the Beyondcell R package was utilized to

calculate Beyondcell Scores (BCS), which quantify single-cell-level sensitivity to specific therapeutic compounds, thereby offering a spatially resolved perspective on treatment response[49].

4.7 Transcription Factor (TF) Analysis

Single-cell regulatory network inference was performed using the SCENIC (Single-Cell rEgulatory Network Inference and Clustering) pipeline to identify TF–centered gene regulatory programs[50]. Regulon activity for each cell was quantified using the AUCell algorithm, which calculates an enrichment score reflecting the activity of each TF-associated gene set at the single-cell level.

To evaluate SPI1- and DBX2-associated transcriptional programs in CAFs, downstream target genes were identified by regulon analysis. To reduce noise and avoid overfitting due to the large number of targets (>3,000), these genes were intersected with the TNFα/NF-κB pathway, which was closely associated with post-treatment COL3A1high CAFs. Principal component analysis (PCA) was performed on the scaled expression matrix of the intersected gene set, and the first principal component (PC1) was defined as the SPI1/DBX2-associated signature score.

4.8 Spatial Transcriptomics Analysis

Spatial transcriptomics data were analyzed using the spaCET R package to infer cell-type composition and spatial interactions within the TME[51]. For each spatial transcriptomics sample, spaCET was first applied to perform cell-type deconvolution,

estimating the relative abundance of different cell populations at each spatial spot based on reference expression profiles.

To quantify spatial co-localization between specific cell types, the SpaCET.CCI.colocalization function was subsequently used. This analysis computes a fraction_rho value for each pair of cell types within a given sample, representing a correlation coefficient that reflects the degree of spatial co-localization between two cell populations across spatial locations .

4.9 Patients and Tissue Samples

This retrospective study involved 72 patients with histologically or cytologically confirmed BC. Inclusion criteria were: (1) histological or cytological confirmation of BC; (2) early-stage disease (stages I–III) without metastasis according to the 8th edition of the AJCC staging system; (3) availability of comprehensive baseline clinical and imaging data; (4) prior receipt of neoadjuvant chemotherapy; and (5) Eastern Cooperative Oncology Group (ECOG) performance status ranging from 0 to 2, along with sufficient organ function. Treatment responses were evaluated based on RECIST 1.1 criteria.

4.10 Cell Lines and Culture Conditions

MDA-MB-231, MDA-MB-453, and 293T cells were obtained from the Cell Resource Center, Institute of Basic Medical Sciences (CAMS, China), and cultured in DMEM (GIBCO, USA). The CP-H172 cell line, derived from breast cancer-associated fibroblasts (CAFs), was obtained from Procell Life Science & Technology (Wuhan,

China) and cultured using CM-H172 medium according to the supplier's instructions. Cells were grown at 37°C in a humidified atmosphere containing 5% CO_2.

4.11 Co-culture and Flow Cytometry Assays

Transwell chambers (0.4-μm pore size, Corning, CLS3412) were used to establish indirect co-culture systems. BC cells (MDA-MB-231 or MDA-MB-453, 1×10^5) were seeded in the lower chamber, and CP-H172 fibroblasts (1×10^5) in the upper chamber. After drug treatments, cells along with culture supernatants were collected, then stained with Annexin V-APC (Biolegend, USA) and Propidium Iodide (Solarbio, China), followed by analysis using FlowJo version 10.

4.12 Lentiviral Vector Construction and Transduction

COL3A1-targeting shRNA constructs were generated using the pLKO.1-PuroR vector (TsingKe Biotechnology, China). Lentiviruses were produced in HEK293T cells by co-transfecting shRNA plasmids with psPAX2 and pMD.2G helper plasmids (Addgene, USA). Viral supernatants were collected at 48 h and used to transduce BC cells. Stable cell lines were selected with puromycin (Solarbio, China).

4.13 Quantitative Real-Time PCR and Enzyme Linked Immunosorbent Assay (ELISA)

RNA was isolated from samples utilizing the FastPure Cell/Tissue Total RNA Isolation Kit provided by Vazyme (China). RNA quantity and purity were assessed using a NanoDrop spectrophotometer (Thermo Fisher Scientific, USA). qPCR was carried out using TB Green® Premix Ex Taq™ (Takara, Japan). The sequences of primers are provided in Supplementary Table 1. Cell supernatants from the different treatment

groups were harvested for ELISA. ELISA was performed according to the manufacturer's instructions. The following ELISA kits were used for detection: THBS2 (Jonln,China), FN1(Multi Science,China), MDK (Multi Science,China).

4.14 Western Blotting

Proteins were extracted using NETN buffer and separated by SDS-PAGE. After transfer, membranes were blocked and probed with primary antibodies against COL3A1, β-ACTINE, E-cadherin, N-cadherin, Vimentin, SNAIL, SCD, ENO1, AKT, phospho-AKT (Ser473), PI3K p85, and phospho-PI3K p85, followed by secondary antibody incubation. All antibodies were sourced from Abcam or Cell Signaling Technology as specified.

4.15 Transwell Assay

A Transwell chamber (Corning, 354480) pre-coated with Matrigel was used for the migration assay. MDA-MB-231 cells (3×10^4), previously co-cultured with CP-H172shNC or CP-H172shCOL3A1, were placed in the upper chamber. The system was then incubated for 24 h at 37 °C with 600 μL of 20% FBS medium in the lower well. Following incubation, migrated cells on the membrane were fixed with 70% ethanol (15 min) and stained with 2% Crystal Violet (10 min) at room temperature.

4.16 Transmission Electron Microscopy (TEM)

Fixation of cells was performed using Trump's glutaraldehyde, with a secondary fixation step in 1% osmium tetroxide. Samples were dehydrated in ethanol, then embedded in resin composed of Araldite 502 and dodecenyl succinic anhydride containing the catalyst DMP-30. Ultrathin sections were sectioned on a Leica EM UC7

ultramicrotome, placed on copper grids, and stained using uranyl acetate and lead citrate.Imaging was performed with a FEI Spirit Tecnia TEM at 60 kV.

4.17 BODIPY Staining for Lipid Droplets

To detect oleic acid accumulation, CP-H172 cells grown on coverslips were treated, fixed with 4% paraformaldehyde, and incubated with 2 μM BODIPY™ 493/503 (Thermo Fisher Scientific) for 30 minutes in the dark. Slides were mounted and imaged with a Leica SP8 confocal microscope. Quantification of fluorescence intensity was performed with ImageJ software.

4.18 Cell Viability and Drug Sensitivity Assays

Cell viability and drug sensitivity were assessed using the Cell Counting Kit-8 (CCK-8; MedChemExpress, China). Cells were plated in 96-well plates and treated for 24 h. CCK-8 reagent (10%) was added, followed by 2 h incubation at 37°C. Absorbance at a wavelength of 450 nm was measured, and the half-maximal inhibitory concentration (IC_{50}) was calculated.

4.19 In Vivo Tumor Xenograft Models

NOD/SCID mice (6 weeks old) were injected into the mammary fat pads with MDA-MB-231 cells and CP-H172 fibroblasts (1:3 ratio). Upon reaching a tumor volume of ~100 mm^3, mice were treated with paclitaxel (10 mg/kg/week, intraperitoneally). Tumor volumes were measured every 3 days using the following formula: length × $width^2 \times 0.5$ (cm^3).

4.20 Lung Metastasis Modeling

To investigate lung metastasis formation, female Balb/c nude mice (6 weeks old,

pathogen-free) were used. A suspension containing 5×10^5 viable MDA-MB-231 cells, co-cultured with either CP-H172^{shNC} or CP-H172^{shCOL3A1} fibroblasts, was injected into the tail vein of each mouse in a volume of 0.1 mL. The endpoint assays were conducted 4 weeks post-injection.

4.21 Histology and Immunohistochemistry (IHC)

Formalin-fixed, paraffin-embedded tumor tissues were sliced into 4 μm sections. Routine H&E staining was applied. Prior to immunohistochemical analysis, antigen retrieval was carried out, followed by incubation with primary antibodies against COL3A1, SCD, or ENO1. HRP-conjugated secondary antibodies were applied, followed by hematoxylin counterstaining. Positive staining was quantified using ImageJ. IHC staining results were defined as: (Staining Intensity) × (% Positive Cells).

4.22 Multiplex immunofluorescence (mxIF) Staining

mxIF staining was performed on formalin-fixed, paraffin-embedded tissue sections using an iterative staining and imaging approach. Briefly, tissue sections were sequentially incubated with primary antibodies against selected targets, followed by fluorophore-conjugated secondary antibodies. After each imaging cycle, fluorescence signals were quenched prior to the next round of staining to enable the detection of multiple markers on the same tissue section. Nuclei were counterstained with DAPI, and images were acquired using a fluorescence microscope under identical acquisition settings across samples.

4.23 Ethics Statement

All animal experiments were conducted in accordance with protocols approved by the

Institutional Animal Care and Use Committee of the Cancer Hospital, Chinese Academy of Medical Sciences and Peking Union Medical College. At the experimental endpoint, mice were humanely euthanized to minimize suffering. Euthanized was performed via an overdose of sodium pentobarbital (150 mg/kg, i.p.). Death was confirmed by observing the permanent cessation of heartbeat and respiration, followed by cervical dislocation as a secondary physical method to ensure complete euthanasia. Human tissue usage was approved by the Ethics Review Committee of Liaoning Cancer Hospital (Approval No.: LH20250340), and conducted in accordance with the Declaration of Helsinki.

4.24 Statistical Analysis

All statistical analyses were performed using R (version 4.2.1). Two-group comparisons were conducted using either Student's t-test or the Wilcoxon rank-sum test, depending on data distribution and group characteristics. Correlations between variables were examined using Pearson's correlation coefficient. Differences in survival outcomes were evaluated via the log-rank test. Statistical significance was defined as a p-value less than 0.05. Significance levels were noted as follows: ns (not significant), *$p < 0.05$, **$p < 0.01$, ***$p < 0.001$, ****$p < 0.0001$.

5. Acknowledgements

We would like to express our sincere gratitude to the patients for their contribution to this study. We also acknowledge the GEO and TCGA databases for providing high-quality data.

6.Data availability

The sequencing data utilized in this study are publicly available from the databases referenced in the manuscript. Other data supporting the findings are available from the corresponding author upon reasonable request.

7. Code availability

Relevant code is accessible through the corresponding author(s) upon reasonable request.

8. Competing interests

All authors declare no competing interests.

9. Author contributions

PJ: Conceptualization, Methodology, Formal analysis, Investigation, Data curation, Visualization, Writing-original draft. XL: Investigation, Methodology, Visualization, Writing-original draft, Funding acquisition. ZW: Investigation, Methodolog; SL: Investigation, Writing-editing; YH: Clinical samples collection; YL: Funding acquisition, Project administration, Resources, Supervision; YC: Conceptualization, Supervision, Validation, Writing-review. XS: Conceptualization, Funding acquisition, Project administration, Supervision, Methodology, Investigation, Writing-review & editing.

10. Funding

This work was supported by National Natural Science Foundation of China (82403430), the Technology Program Joint Fund of Liaoning Province (2023-BSBA-207), Oncology Project of Liaoning Cancer Hospital (2024-ZLKF-09), Tianjin Key Medical Discipline Construction Project (TJYXZDXK-3-003A) and Noncommunicable Chronic Diseases-National Science and Technology Major Project (2023ZD0502200).

11. Reference

1. Santucci C, Mignozzi S, Levi F, et al. European cancer mortality predictions for the year 2025 with focus on breast cancer. Annals of oncology : official journal of the European Society for Medical Oncology 2025; 36(4): 460-8.

2. Waks AG, Winer EP. Breast Cancer Treatment: A Review. Jama 2019; 321(3): 288-300.

3. Harbeck N, Penault-Llorca F, Cortes J, et al. Breast cancer. Nature reviews Disease primers 2019; 5(1): 66.

4. Gascard P, Tlsty TD. Carcinoma-associated fibroblasts: orchestrating the composition of malignancy. Genes & development 2016; 30(9): 1002-19.

5. Liao Z, Tan ZW, Zhu P, Tan NS. Cancer-associated fibroblasts in tumor microenvironment - Accomplices in tumor malignancy. Cell Immunol 2019; 343: 103729.

6. Chen C, Liu J, Lin X, et al. Crosstalk between cancer-associated fibroblasts and regulated cell death in tumors: insights into apoptosis, autophagy, ferroptosis, and pyroptosis. Cell death discovery 2024; 10(1): 189.

7. Öhlund D, Handly-Santana A, Biffi G, et al. Distinct populations of inflammatory fibroblasts

and myofibroblasts in pancreatic cancer. The Journal of experimental medicine 2017; 214(3): 579-96.

8. Butti R, Khaladkar A, Bhardwaj P, Prakasam G. Heterotypic signaling of cancer-associated fibroblasts in shaping the cancer cell drug resistance. Cancer drug resistance (Alhambra, Calif) 2023; 6(1): 182-204.

9. Chen X, Chen S, Yu D. Metabolic Reprogramming of Chemoresistant Cancer Cells and the Potential Significance of Metabolic Regulation in the Reversal of Cancer Chemoresistance. Metabolites 2020; 10(7).

10. Linares J, Marín-Jiménez JA, Badia-Ramentol J, Calon A. Determinants and Functions of CAFs Secretome During Cancer Progression and Therapy. Frontiers in cell and developmental biology 2020; 8: 621070.

11. Maeda A, Takahashi H, Harata S, et al. The Interaction Between Cancer-associated Fibroblasts and Cancer Cells Enhances Bcl-xL and Mcl-1 in Colorectal Cancer. Anticancer research 2022; 42(3): 1277-88.

12. Bian L, Sun X, Jin K, He Y. Oral cancer-associated fibroblasts inhibit heat-induced apoptosis in Tca8113 cells through upregulated expression of Bcl-2 through the Mig/CXCR3 axis. Oncology reports 2012; 28(6): 2063-8.

13. Li Y, Li X, Deng M, Ye C, Peng Y, Lu Y. Cancer-Associated Fibroblasts Hinder Lung Squamous Cell Carcinoma Oxidative Stress-Induced Apoptosis via METTL3 Mediated m(6)A Methylation of COL10A1. Oxidative medicine and cellular longevity 2022; 2022: 4320809.

14. Zhang Q, An ZY, Jiang W, Jin WL, He XY. Collagen code in tumor microenvironment: Functions, molecular mechanisms, and therapeutic implications. Biomedicine & pharmacotherapy = Biomedecine & pharmacotherapie 2023; 166: 115390.

15. Xu K, Wang H, Zou YX, et al. Distinct fibroblast subpopulations associated with bone, brain or intrapulmonary metastasis in advanced non-small-cell lung cancer. Clinical and translational medicine 2024; 14(3): e1605.

16. LaRue MM, Parker S, Puccini J, Cammer M, Kimmelman AC, Bar-Sagi D. Metabolic reprogramming of tumor-associated macrophages by collagen turnover promotes fibrosis in pancreatic cancer. Proceedings of the National Academy of Sciences of the United States of America 2022; 119(16): e2119168119.

17. Chen Y, Yang S, Tavormina J, et al. Oncogenic collagen I homotrimers from cancer cells bind to α3β1 integrin and impact tumor microbiome and immunity to promote pancreatic cancer. Cancer cell 2022; 40(8): 818-34.e9.

18. Li G, Tao T, Deng D, et al. Collagen-targeted tumor-specific transepithelial penetration

enhancer mediated intravesical chemoimmunotherapy for non-muscle-invasive bladder cancer. Biomaterials 2022; 283: 121422.

19. Zhang JY, Zhu WW, Wang MY, et al. Cancer-associated fibroblasts promote oral squamous cell carcinoma progression through LOX-mediated matrix stiffness. Journal of translational medicine 2021; 19(1): 513.

20. Zhou Y, Jiang Z, Cao L, Yang J. The role of various collagen types in tumor biology: a review. Frontiers in oncology 2025; 15: 1549797.

21. Zhang H, Ding C, Li Y, et al. Data mining-based study of collagen type III alpha 1 (COL3A1) prognostic value and immune exploration in pan-cancer. Bioengineered 2021; 12(1): 3634-46.

22. Stewart DC, Brisson BK, Dekky B, et al. Prognostic and therapeutic implications of tumor-restrictive type III collagen in the breast cancer microenvironment. NPJ Breast Cancer 2024; 10(1): 86.

23. Ren J, Zhao S, Lai J. Role and mechanism of COL3A1 in regulating the growth, metastasis, and drug sensitivity in cisplatin-resistant non-small cell lung cancer cells. Cancer Biol Ther 2024; 25(1): 2328382.

24. Sun Y, Zhang X, Hang D, et al. Integrative plasma and fecal metabolomics identify functional metabolites in adenoma-colorectal cancer progression and as early diagnostic biomarkers. Cancer cell 2024; 42(8): 1386-400.e8.

25. Chen Y, McAndrews KM, Kalluri R. Clinical and therapeutic relevance of cancer-associated fibroblasts. Nature reviews Clinical oncology 2021; 18(12): 792-804.

26. Biffi G, Tuveson DA. Diversity and Biology of Cancer-Associated Fibroblasts. Physiological reviews 2021; 101(1): 147-76.

27. Costa A, Kieffer Y, Scholer-Dahirel A, et al. Fibroblast Heterogeneity and Immunosuppressive Environment in Human Breast Cancer. Cancer cell 2018; 33(3): 463-79.e10.

28. Yan Y, Sun D, Hu J, et al. Multi-omic profiling highlights factors associated with resistance to immuno-chemotherapy in non-small-cell lung cancer. Nat Genet 2025; 57(1): 126-39.

29. Xiao L, Kim DJ, Davis CL, et al. Tumor Endothelial Cells with Distinct Patterns of TGF β -Driven Endothelial-to-Mesenchymal Transition. Cancer research 2015; 75(7): 1244-54.

30. Mousset A, Lecorgne E, Bourget I, et al. Neutrophil extracellular traps formed during chemotherapy confer treatment resistance via TGF- β activation. Cancer cell 2023; 41(4): 757-75.e10.

31. Singh A, Settleman J. EMT, cancer stem cells and drug resistance: an emerging axis of evil in the war on cancer. Oncogene 2010; 29(34): 4741-51.

32. Liu S, Zhang X, Wang W, et al. Metabolic reprogramming and therapeutic resistance in primary and metastatic breast cancer. Molecular cancer 2024; 23(1): 261.

33. Saikia S, Ahmed F, Prajapati BG, et al. Reprogramming of Lipid Metabolism in Cancer: New Insight into Pathogenesis and Therapeutic Strategies. Current pharmaceutical biotechnology 2023; 24(15): 1847-58.

34. Yang D, Li Y, Xing L, et al. Utilization of adipocyte-derived lipids and enhanced intracellular trafficking of fatty acids contribute to breast cancer progression. Cell communication and signaling : CCS 2018; 16(1): 32.

35. Yu L, Liebenberg K, Shen Y, et al. Tumor-derived arachidonic acid reprograms neutrophils to promote immune suppression and therapy resistance in triple-negative breast cancer. Immunity 2025; 58(4): 909-25.e7.

36. Roongta UV, Pabalan JG, Wang X, et al. Cancer cell dependence on unsaturated fatty acids implicates stearoyl-CoA desaturase as a target for cancer therapy. Molecular cancer research : MCR 2011; 9(11): 1551-61.

37. Griffiths B, Lewis CA, Bensaad K, et al. Sterol regulatory element binding protein-dependent regulation of lipid synthesis supports cell survival and tumor growth. Cancer & metabolism 2013; 1(1): 3.

38. Williams KJ, Argus JP, Zhu Y, et al. An essential requirement for the SCAP/SREBP signaling axis to protect cancer cells from lipotoxicity. Cancer research 2013; 73(9): 2850-62.

39. Lai JI, Chao TC, Liu CY, Huang CC, Tseng LM. A systemic review of taxanes and their side effects in metastatic breast cancer. Frontiers in oncology 2022; 12: 940239.

40. Gradishar WJ, Moran MS, Abraham J, et al. Breast Cancer, Version 3.2024, NCCN Clinical Practice Guidelines in Oncology. Journal of the National Comprehensive Cancer Network : JNCCN 2024; 22(5): 331-57.

41. Huang T, Ren X, Tang X, et al. Current perspectives and trends of CD39-CD73-eAdo/A2aR research in tumor microenvironment: a bibliometric analysis. Frontiers in immunology 2024; 15: 1427380.

42. Luo L, Yang P, Mastoraki S, et al. Single-cell RNA sequencing identifies molecular biomarkers predicting late progression to CDK4/6 inhibition in patients with HR+/HER2- metastatic breast cancer. Molecular cancer 2025; 24(1): 48.

43. Liu Z, Ba Y, Shan D, et al. THBS2-producing matrix CAFs promote colorectal cancer progression and link to poor prognosis via the CD47-MAPK axis. Cell reports 2025; 44(4): 115555.

44. Zhang L, Yu X, Zheng L, et al. Lineage tracking reveals dynamic relationships of T cells in

colorectal cancer. Nature 2018; 564(7735): 268-72.

45. Jin S, Guerrero-Juarez CF, Zhang L, et al. Inference and analysis of cell-cell communication using CellChat. Nature communications 2021; 12(1): 1088.

46. Tran KA, Addala V, Johnston RL, et al. Performance of tumour microenvironment deconvolution methods in breast cancer using single-cell simulated bulk mixtures. Nature communications 2023; 14(1): 5758.

47. Sun D, Guan X, Moran AE, et al. Identifying phenotype-associated subpopulations by integrating bulk and single-cell sequencing data. Nature biotechnology 2022; 40(4): 527-38.

48. Chu T, Wang Z, Pe'er D, Danko CG. Cell type and gene expression deconvolution with BayesPrism enables Bayesian integrative analysis across bulk and single-cell RNA sequencing in oncology. Nature cancer 2022; 3(4): 505-17.

49. Fustero-Torre C, Jiménez-Santos MJ, García-Martín S, et al. Beyondcell: targeting cancer therapeutic heterogeneity in single-cell RNA-seq data. Genome medicine 2021; 13(1): 187.

50. Aibar S, González-Blas CB, Moerman T, et al. SCENIC: single-cell regulatory network inference and clustering. Nature methods 2017; 14(11): 1083-6.

51. Ru B, Huang J, Zhang Y, Aldape K, Jiang P. Estimation of cell lineages in tumors from spatial transcriptomics data. Nature communications 2023; 14(1): 568.

12. Figure legends:

Figure 1. CAFs and COL3A1 are associated with chemoresistance and poor prognosis in BC.
(A-B) MCP-counter revealed significant differences in CAFs abundance between chemotherapy-sensitive and -resistant groups in GSE20194 dataset.
(C-D) EPIC revealed significant differences in CAFs abundance between chemotherapy-sensitive and -resistant groups in GSE20194 dataset.
(E) Top 10 collagenfamily genes most correlated with CAFs abundance as estimated by EPIC (left panel) and MCP-counter (right panel) in METABRIC dataset.
(F) Differential expression of collagen family genes in chemotherapy-sensitive versus chemotherapy-resistant patients from the GSE20194 dataset.
(G) Venn diagram showing the intersection of genes strongly correlated with CAFs abundance and chemotherapy response.
(H) Correlation analysis between COL3A1, COL1A2 and the IC50 of common breast cancer chemotherapeutic agents.
(I) COL3A1 expression is significantly higher in chemotherapy-resistant patients in GSE20194 dataset.
(J-K) Kaplan-Meier analysis showing that high COL3A1 expression is associated with poor OS and RFS in METABRIC dataset.
(L-M) Kaplan-Meier analysis showing that high COL3A1 expression is associated with poor OS and RFS in drug-treated patients of METABRIC dataset.
(N) GSVA demonstrating the different enrichment of hallmark pathways in high- versus low-COL3A1 expression groups.
(O) GSEA shows enrichment of drug resistance-related pathways in COL3A1-high patients.

Wilcox rank-sum test was used for panel B,D; Pearson correlation analysis was used for panel H.
BC, breast cancer; CAFs,cancer-associated fibroblasts; EPIC, Estimating the proportion of immune and cancer cells; OS,overall survival; RFS,relapse-free survival.

Figure 2. Single-cell transcriptomic profiling identifies COL3A1^{high} CAFs subpopulations influncing chemosensitivity.
(A) UMAP plot showing the cell types.
(B) UMAP plot of CAFs colored by subsets according to COL3A1 expression.
(C) UMAP plot of CAFs colored by chemosensitivity.
(D) Proportion of tumor cell subsets in untreated and treated patients.
(E) Proportion of CAFs derived from untreated and treated patients across distinct subsets.
(F) Distribution of cell counts and proportion of CAFs across biological and clinical dimensions.
(G) Volcano plot showing differentially expressed genes in CAFs substes associated with chemoresistance.

(H) UMAP plots showing the features of EMT and oxidative phosphorylation in CAFs.
(I) UMAP plots showing the feature of drug metabolism in tumor cells.
(J) Ro/e analysis reveals differencet infiltation of CAFs and T cells between untreated and treated samples.
(K) Pseudotime trajectory analysis indicates temporal evolution of CAFs substes between naive and treated patients.
(L) The expression of key EMT proteins in MDA-MB-231 co-cultured with CP-H172^{shNC} or CP-H172^{shCOL3A1} , with or without PTX treatment.
(M-N) Representative images (M) and quantitative data (N) of MDA-MB-231 co-cultured with CP-H172^{shNC} or CP-H172^{shCOL3A1} in transwell chamber. Scale bar, 100 μm.
(O) Schematic of the lung metastasis model established by tail vein co-injection of MDA-MB-231 cells with CP-H172^{shNC} or CP-H172^{shCOL3A1}.
(P-Q) Representative images (P) and quantitative data (Q) of HE staining of lung from each group (n =6). Scale bars: 500 μm (top),100 μm (bottom).
(R) Cell viability proporation with PTX in MDA-MB-231, which were cocultured with CP-H172^{shNC} or CP-H172^{shCOL3A1}.
(S) Cell proliferation rate by PTX in MDA-MB-231, which were cocultured with CP-H172^{shNC} or CP-H172^{shCOL3A1}.

Student's t test was used for panel N, Q,R,S.
COL3A1^{high} CAFs, CAFs with high COL3A1 expression; COL3A1^{low} CAFs, CAFs with low COL3A1 expression; COL3A1^{-} CAFs, COL3A1-negative CAFs;

Tumor^{resist},chemoresistant tumor cells; tumor^{sen},chemosensitive tumor cells ; tumor^{inter}, tumor cells with intermediate chemosensitivity.
EMT, Epithelial-Mesenchymal Transition; Ro/e, ratio of observed to expected cell counts; PTX, paclitaxel.

Figure 3. Metabolic reprogramming in COL3A1^{high} CAFs and chemoresistant tumor cells.

(A) Metabolic signature comparison among tumor substes.
(B) Correlation between COL3A1 and SCD expression in CAFs
(C) ENO1 expression across tumor substes.
(D) Apoptosis activity across tumor substes.
(E) SCD expression in CP-H172^{shNC} or CP-H172^{shCOL3A1}.
(F) ENO1 expression in BC cells co-cultured with CP-H172^{shNC} or CP-H172^{shCOL3A1}.
(G) Representative images (left) and quantification (right) of BODIPY™ 493/503 staining for lipids in MDA-MB-231 cells co-cultured with CP-H172^{shNC} or CP-H172^{shCOL3A1}. Scale bars: 20 μm.
(H) TEM images of MDA-MB-231 cells after co-culture with CP-H172shNC (top) or CP-H172shCOL3A1. Scale bars: 5 μm (top),1 μm (bottom).
(I-J) Expression of key AKT/PI3K pathway key proteins in BC cells co-cultured with

CP-H172^{shNC} or CP-H172^{shCOL3A1} , with/without PTX treatment.
(K) SCD expression in CP-H172 treated with/without oleic acid.
(L) ENO1 expression in BC cells treated with/without oleic acid.
(M-N) Expression of key AKT/PI3K pathway key proteins in BC cells with /without ENO1 knocking down, treated with/without oleic acid.
(O) Apoptosis in MDA-MB-231 co-cultured with CP-H172^{shNC} or CP-H172^{shCOL3A1} ± PTX by flow cytometry .
(P) Quantification of apoptosis from panels O.

Pearson correlation analysis was used for panel B; Student's t test was used for panel G,P.
TEM, transmission electron microscopy.

Figure 4. Intercellular communication highlights immunosuppressive signaling from COL3A1^{high} CAFs.
(A) Overview of cell-cell interactions across cell types.
(B) Signal input and output strength of CD99 pathway among cell types.
(C) CD99-PILRA communication intensity in COL3A1^{high} vesus COL3A1^{low} CAFs.
(D) Number and strength of ligand-receptor interactions between CAFs subsets and tumor cell substes.
(E) Top ligand-receptor interactions between CAFs subsets and chemoresistant tumor cells.
(H) The correlation of COL3A1 with FN1, CD99, MDK, and THBS2 in CAFs.
(A) FN1, CD99, MDK, THBS2 mRNA levels in CP-H172^{shNC} or CP-H172^{shCOL3A1}.

Pearson correlation analysis was used for panel F; Student's t test was used for panel G.

Figure 5. The TFs regulates COL3A1 expression in CAFs and promotes chemoresistance.
(A) TFs most correlated with COL3A1^{high} CAFs in treated patients.
(B) Expression of top 5 TFs of figure 5A in treated versus untreated patients.
(C) GSEA analysis of TNFα signaling in treated versus untreated patients and key associated TFs.
(D) TFs most associated with TNFα signaling ssin treated patients.
(E) Expression of top 5 TNFα-related transcription factors, including SPI1, in treated vs. untreated samples.
(F) The ridge plots of SPI1 and DBX2 across CAFs and tumor substes.
(G) Comparison of TF target gene scores between chemoresistant and chemosensitive CAFs.

TFs, transcription factors ; PC1, first principal component .

Figure 6. Spatial proximity and drug resistance potential of COL3A1^{high} CAFs.
(A) Spatial expression pattern of COL3A1 in tissue sections.
(B) Representative spatial maps of CAFs and tumor subsets of sample CID4290.

(C) The heatmap of spatial distance across cell subsets.
(D) Spatial proximity of COL3A1-high CAFs to chemoresistant versus chemosensitive tumor cells.
(E) Representative images of mxIF from clinical samples in clinical samples from patients with differential response to chemotherapy.
(F) Quantification of $COL3A1^{+}$ CAFs, Treg and $CD8^{+}$_IFNG in panel E.
(H) Representative network visualization of the associations between CAFs and tumor cell subsets and their sensitivities to durgs of sample CID4290.

Paired t test was used for panel D. Wilcox rank-sum test was used for panel F .
mxIF, Multiplex immunofluorescence; CR, complete response; HP, high-power field .

Figure 7. Clinical relevance of $COL3A1^{high}$ CAFs in chemoresistance.
(A-B) The abundance of $COL3A1^{high}$ CAFs and resistant tumor cells in GSE20194 dataset.
(C-D) The abundance of $COL3A1^{high}$ CAFs and resistant tumor cells in GSE25066 dataset.
(E-F) Correlation between $COL3A1^{high}$ CAFs and non-resistant tumor cells in GSE20194 and GSE25066 datasets.
(G-I) ROC curves comparing chemosensitive tumor cells alone, in combination with $COL3A1^{low}$ CAFs, and in combination with $COL3A1^{high}$ CAFs in GSE20194 dataset.
(J-K) Kaplan-Meier analysis showing that the abundance of $COL3A1^{high}$ CAFs is associated with poor OS and RFS in METABRIC dataset.
(L) PAM50 subtype distribution stratified by $COL3A1^{high}$ CAFs abundance.
(M) Radar plot of log-rank test p-values for the prognostic model across pan-cancer.
(N-O) Kaplan-Meier survival analysis based on $COL3A1^{high}$ CAFs abundance in TCGA_BRCA (N) and TCGA_LUAD (O).

Wilcox rank-sum test was used for panel A-D; Pearson correlation analysis was used for panel E and F.
ROC, receiver operating characteristic. OS,overall survival; RFS,relapse-free survival.

Figure 8. In Vivo and Clinical Validation of $COL3A1^{high}$ CAFs in BC Chemoresistance.
(A) Schematic diagram of the xenograft model. MDA-MB-231 cells were either injected alone or coinjected with CP-$H172^{shNC}$ or CP-$H172^{shCOL3A1}$ at a ratio of 1:3 into immunodeficient mice.
(B) Photographs of tumors in each group.
(C-E) Tumor growth curves (C), tumor weights (D), and body weight changes of mice (E) in each group (n = 6).
(F-G) Representative images (F) and quantitative data (G) of IHC forSCD and ENO1 in tumor samples from each group (n =6). Scale bar, 100 μm.
(H) Correlation between COL3A1 and SCD, ENO1 expression based on IHC staining.

(I) Representative ultrasound images from clinical samples.
(G-K) Representative IHC images of COL3A1, SDC1, and ENO1 in CR (G) and non-CR patients (K).
(L) Expression levels of COL3A1, SDC1, and ENO1 in CR and non-CR patients.
(M) Kaplan-Meier analysis showing that high COL3A1 expression is associated with poor DFS in our cohort.

Student's t test was used for panel C, D, E and G. Wilcox rank-sum test was used for panel L.
IHC, immunohistochemistry; CR, complete response; DFS,disease-free survival.

Figure 9. Graphical Abstract: COL3A1^{high} CAFs promote BC chemoresistance through oleic acid metabolism reprogramming and TME remodeling. Figure created with BioRender.com.

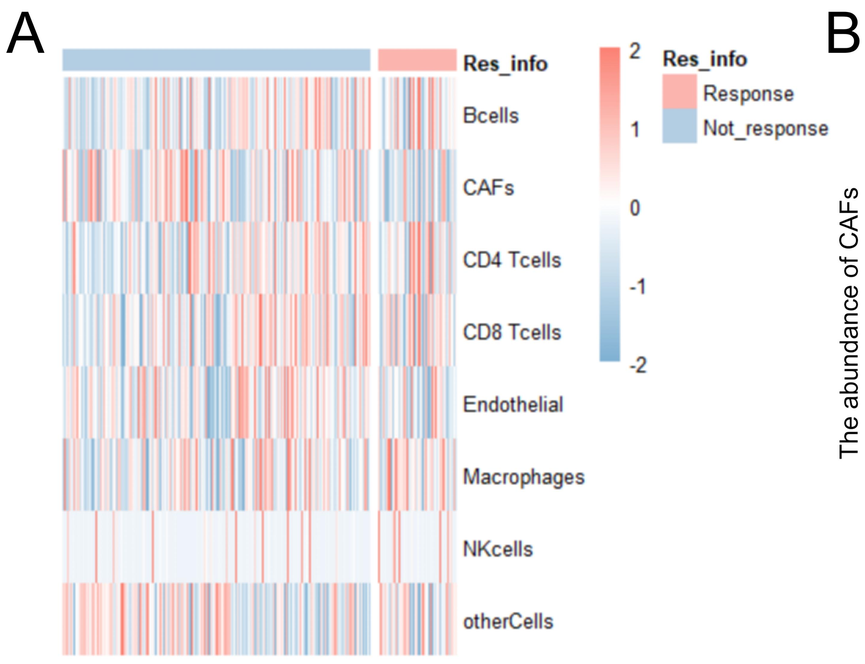
A
Res_info
Bcells
CAFs
CD4 Tcells
CD8 Tcells
Endothelial
Macrophages
NKcells
otherCells
2
1
0
-1
-2
Res_info
Response
Not_response

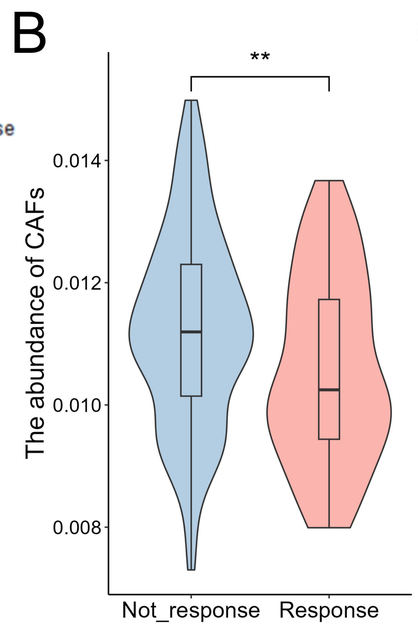
B
**
The abundance of CAFs
0.014
0.012
0.010
0.008
Not_response
Response

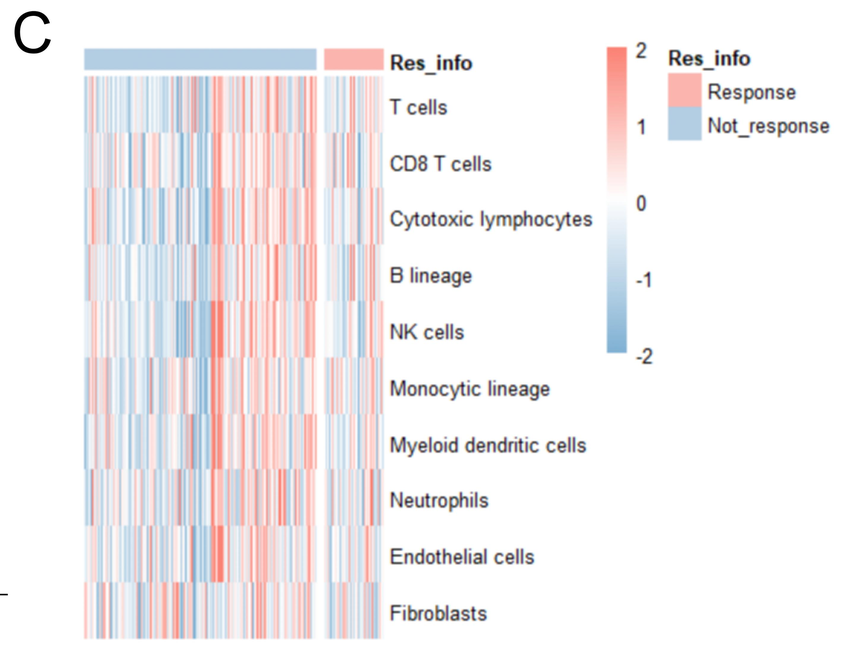
C
Res_info
T cells
CD8 T cells
Cytotoxic lymphocytes
B lineage
NK cells
Monocytic lineage
Myeloid dendritic cells
Neutrophils
Endothelial cells
Fibroblasts
2
1
0
-1
-2
Res_info
Response
Not_response

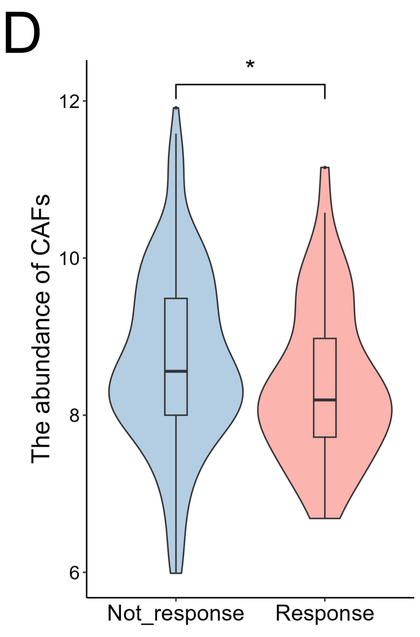
D
*
The abundance of CAFs
12
10
8
6
Not_response
Response

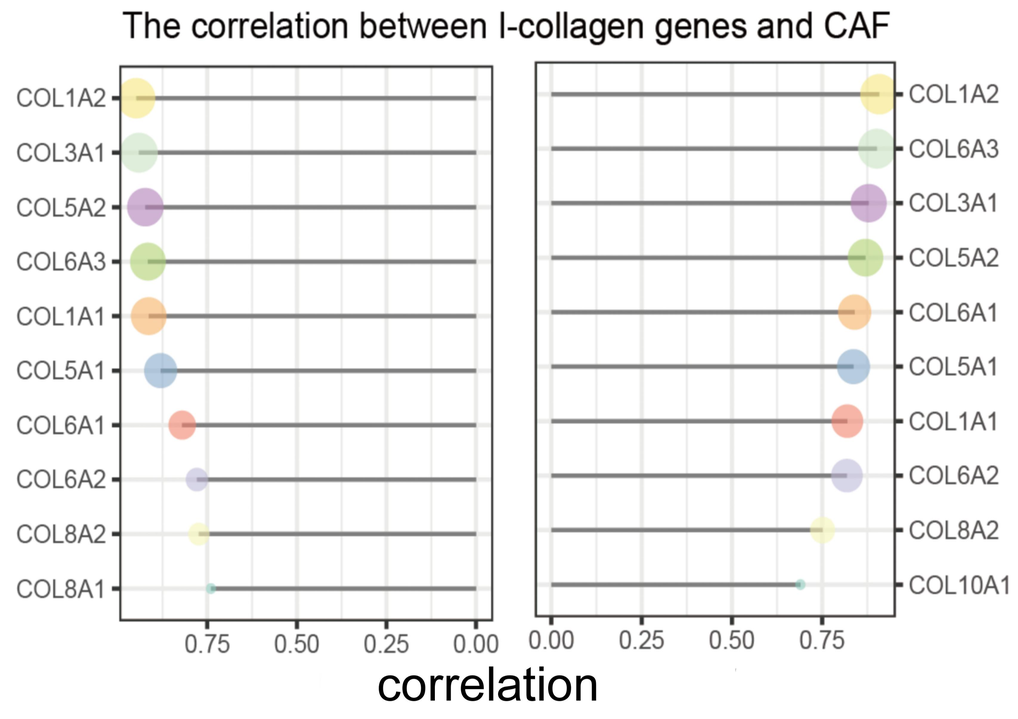
The correlation between I-collagen genes and CAF
COL1A2
COL3A1
COL5A2
COL6A3
COL1A1
COL5A1
COL6A1
COL6A2
COL8A2
COL8A1
0.75 0.50 0.25 0.00
0.00 0.25 0.50 0.75
COL1A2
COL6A3
COL3A1
COL5A2
COL6A1
COL5A1
COL1A1
COL6A2
COL8A2
COL10A1
correlation
cor
0.70
0.75
0.80
0.85
0.90

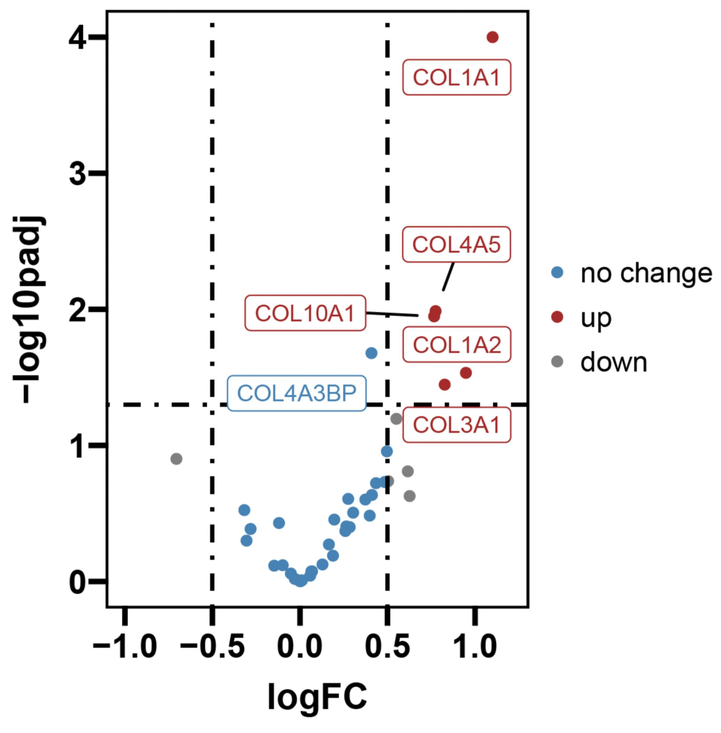
F
−log10padj
4
3
2
1
0
−1.0 −0.5 0.0 0.5 1.0
logFC
COL1A1
COL4A5
COL10A1
COL1A2
COL4A3BP
COL3A1
no change
up
down

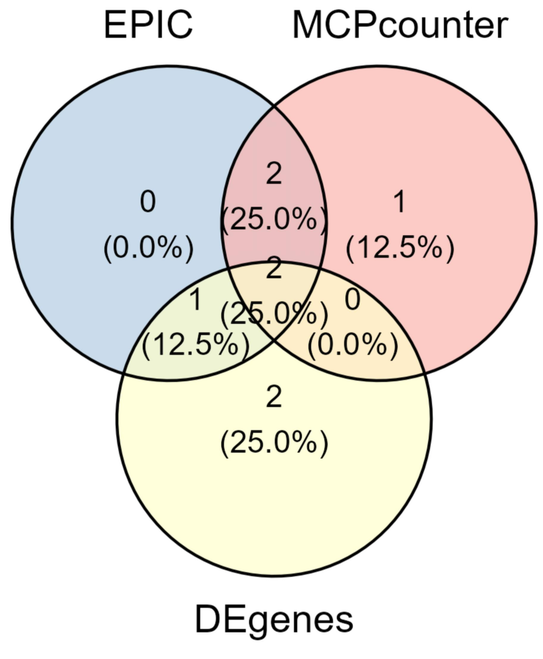
G
EPIC
MCPcounter
DEgenes
0
(0.0%)
2
(25.0%)
1
(12.5%)
2
(25.0%)
1
(12.5%)
0
(0.0%)
2
(25.0%)

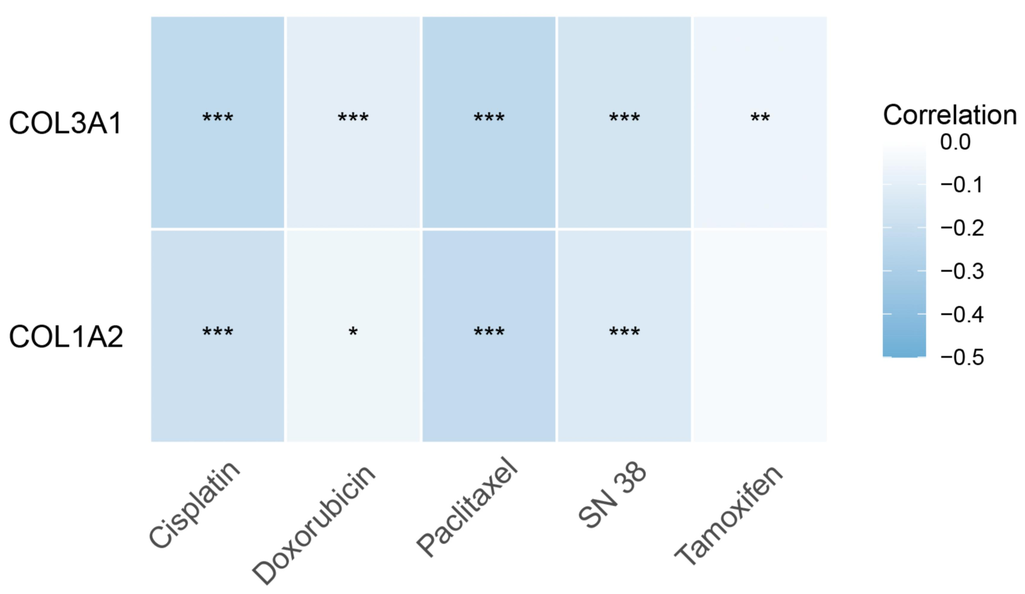
COL3A1
COL1A2
***
***
***
***
**
***
*
***
***
Cisplatin
Doxorubicin
Paclitaxel
SN 38
Tamoxifen
Correlation
0.0
−0.1
−0.2
−0.3
−0.4
−0.5

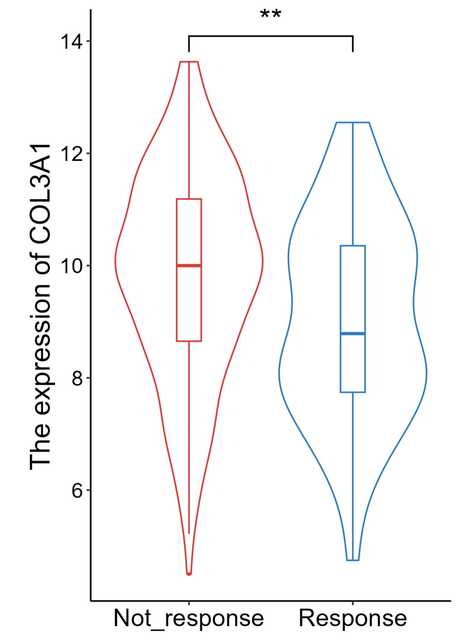
The expression of COL3A1
**
14
12
10
8
6
Not_response
Response

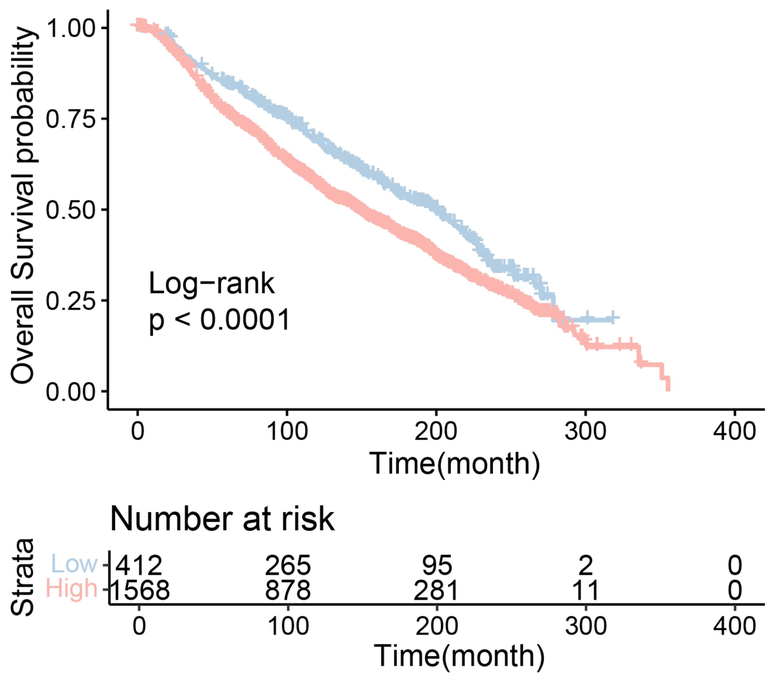
Overall Survival probability
1.00
0.75
0.50
0.25
0.00
Log−rank
p < 0.0001
0
100
200
300
400
Time(month)
Number at risk
Strata
Low 412 265 95 2 0
High 1568 878 281 11 0
Time(month)

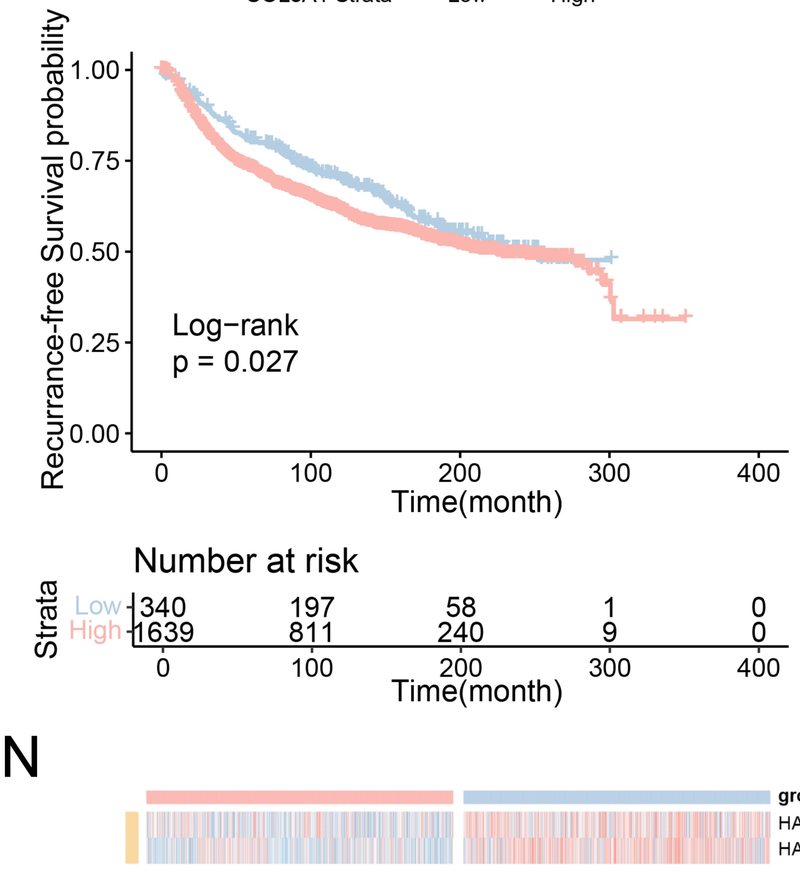
COL3A1 Strata Low High
Recurrance-free Survival probability
1.00
0.75
0.50
0.25
0.00
Log−rank
p = 0.027
0
100
200
300
400
Time(month)
Number at risk
Strata
Low 340 197 58 1 0
High 1639 811 240 9 0
Time(month)

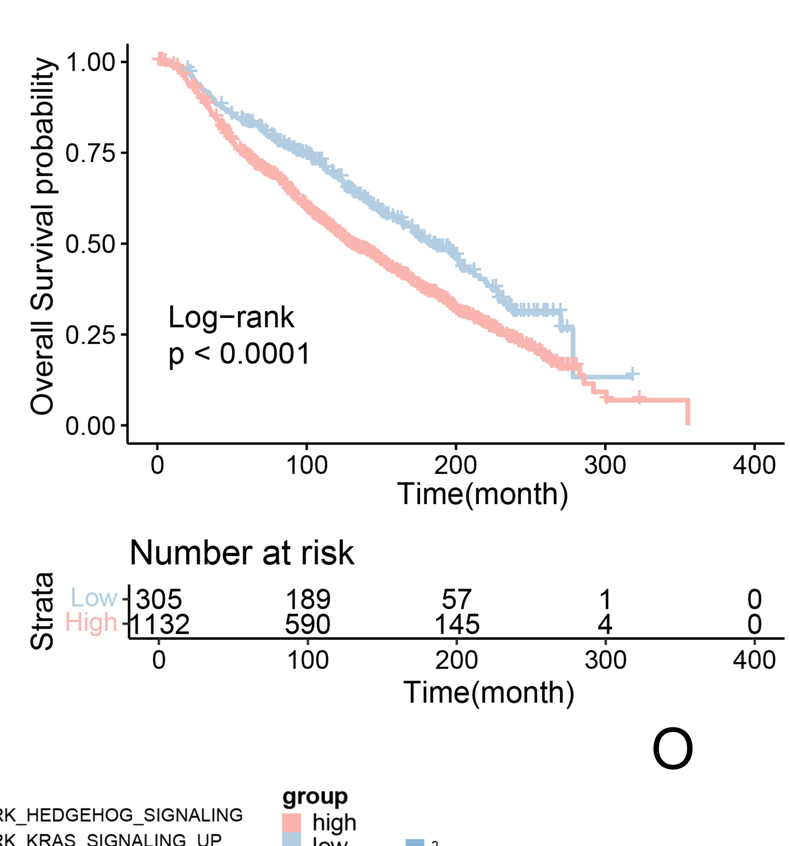
COL3A1 Strata Low High
Overall Survival probability
1.00
0.75
0.50
0.25
0.00
Log−rank
p < 0.0001
0
100
200
300
400
Time(month)
Number at risk
Strata
Low 305 189 57 1 0
High 1132 590 145 4 0
Time(month)

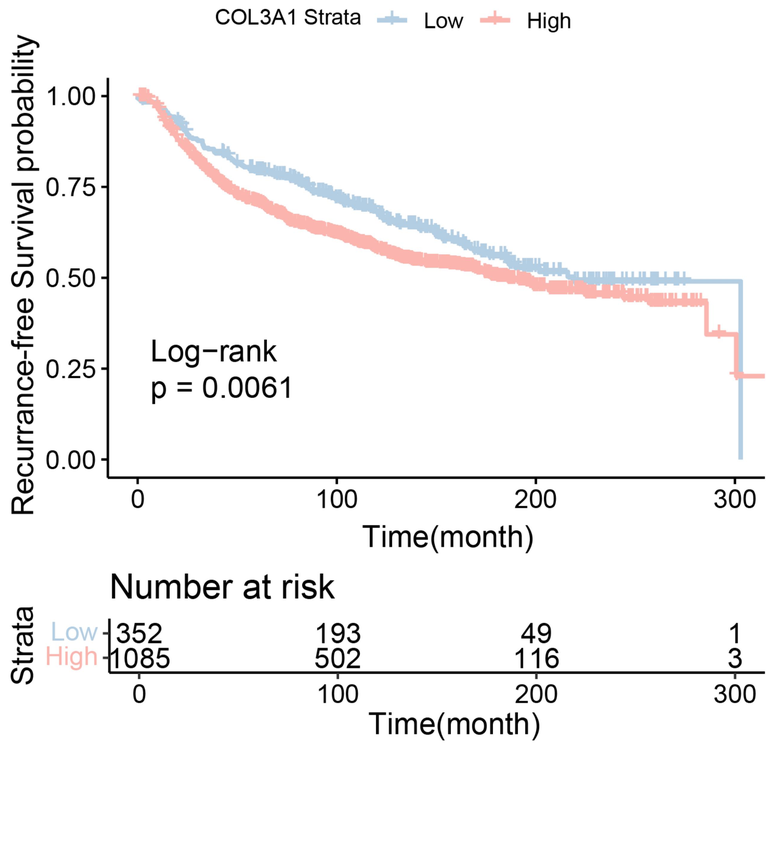
COL3A1 Strata Low High
Recurrance-free Survival probability
1.00
0.75
0.50
0.25
0.00
Log−rank
p = 0.0061
0
100
200
300
Time(month)
Number at risk
Strata
Low 352 193 49 1
High 1085 502 116 3
Time(month)

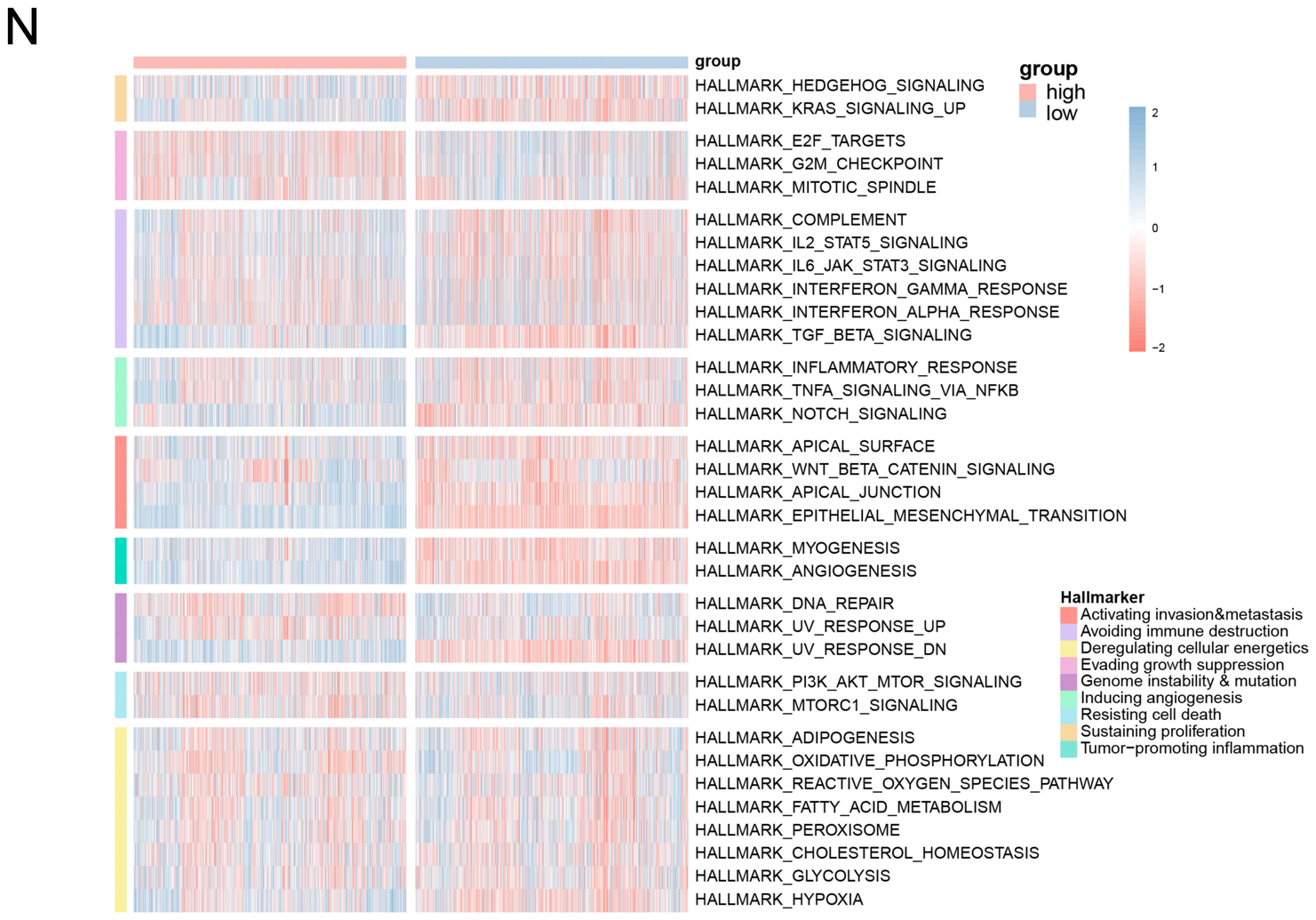
N
group
HALLMARK_HEDGEHOG_SIGNALING
HALLMARK_KRAS_SIGNALING_UP
HALLMARK_E2F_TARGETS
HALLMARK_G2M_CHECKPOINT
HALLMARK_MITOTIC_SPINDLE
HALLMARK_COMPLEMENT
HALLMARK_IL2_STAT5_SIGNALING
HALLMARK_IL6_JAK_STAT3_SIGNALING
HALLMARK_INTERFERON_GAMMA_RESPONSE
HALLMARK_INTERFERON_ALPHA_RESPONSE
HALLMARK_TGF_BETA_SIGNALING
HALLMARK_INFLAMMATORY_RESPONSE
HALLMARK_TNFA_SIGNALING_VIA_NFKB
HALLMARK_NOTCH_SIGNALING
HALLMARK_APICAL_SURFACE
HALLMARK_WNT_BETA_CATENIN_SIGNALING
HALLMARK_APICAL_JUNCTION
HALLMARK_EPITHELIAL_MESENCHYMAL_TRANSITION
HALLMARK_MYOGENESIS
HALLMARK_ANGIOGENESIS
HALLMARK_DNA_REPAIR
HALLMARK_UV_RESPONSE_UP
HALLMARK_UV_RESPONSE_DN
HALLMARK_PI3K_AKT_MTOR_SIGNALING
HALLMARK_MTORC1_SIGNALING
HALLMARK_ADIPOGENESIS
HALLMARK_OXIDATIVE_PHOSPHORYLATION
HALLMARK_REACTIVE_OXYGEN_SPECIES_PATHWAY
HALLMARK_FATTY_ACID_METABOLISM
HALLMARK_PEROXISOME
HALLMARK_CHOLESTEROL_HOMEOSTASIS
HALLMARK_GLYCOLYSIS
HALLMARK_HYPOXIA
group
high
low
2
1
0
−1
−2
Hallmarker
Activating invasion&metastasis
Avoiding immune destruction
Deregulating cellular energetics
Evading growth suppression
Genome instability & mutation
Inducing angiogenesis
Resisting cell death
Sustaining proliferation
Tumor−promoting inflammation

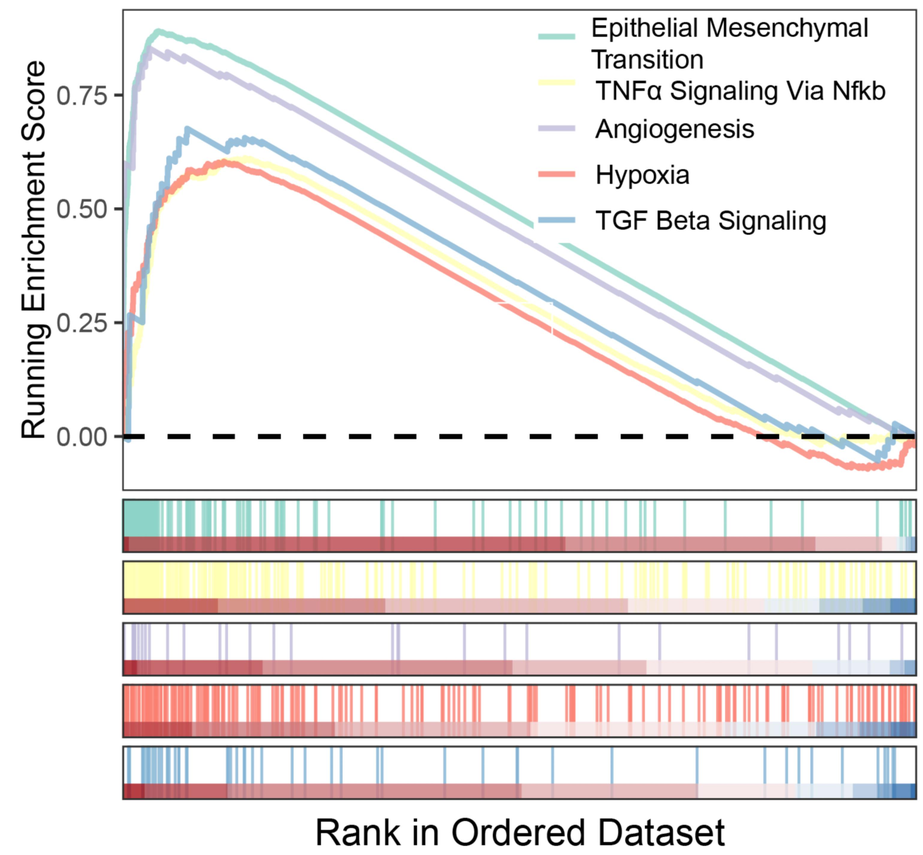
O
Running Enrichment Score
0.75
0.50
0.25
0.00
Epithelial Mesenchymal Transition
TNFα Signaling Via Nfkb
Angiogenesis
Hypoxia
TGF Beta Signaling
Rank in Ordered Dataset

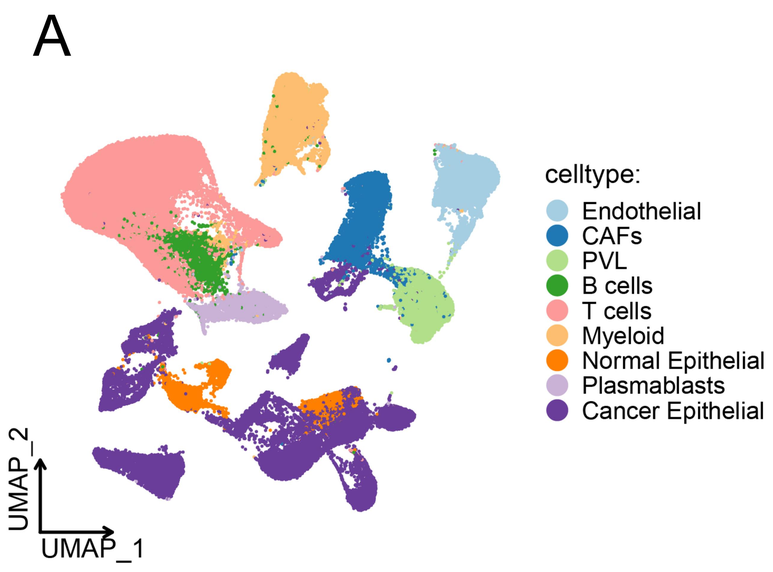
A
UMAP_2
UMAP_1
celltype:
Endothelial
CAFs
PVL
B cells
T cells
Myeloid
Normal Epithelial
Plasmablasts
Cancer Epithelial

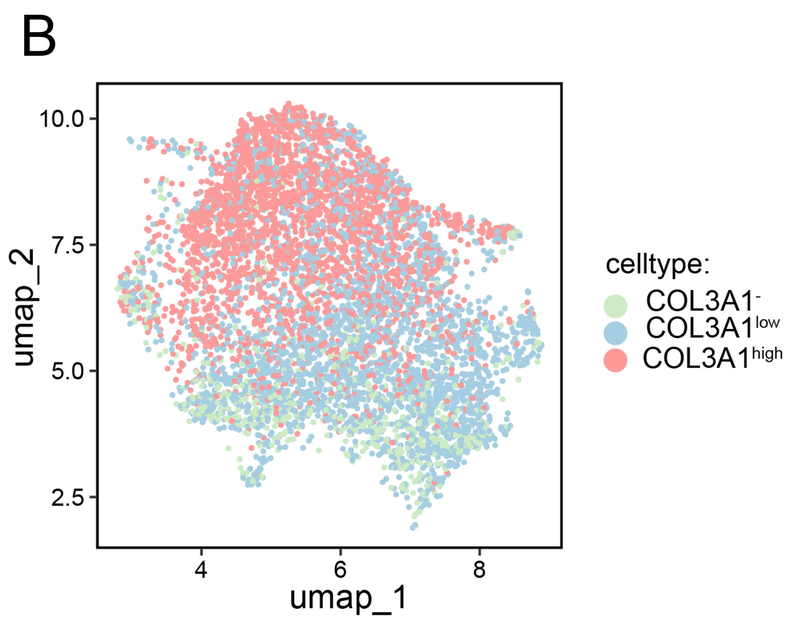
B
umap_2
umap_1
celltype:
COL3A1-
COL3A1low
COL3A1high

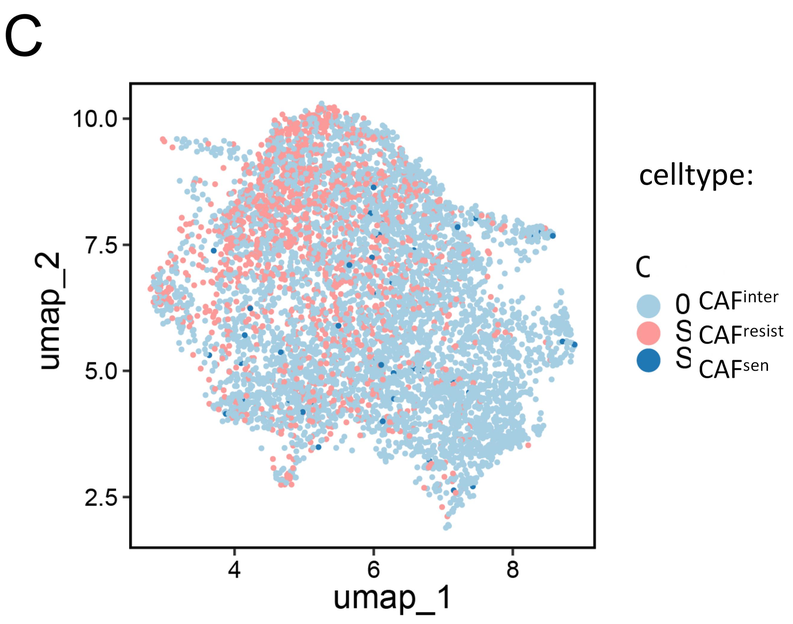
C
umap_2
umap_1
celltype:
0 CAFinter
S CAFresist
S CAFsen

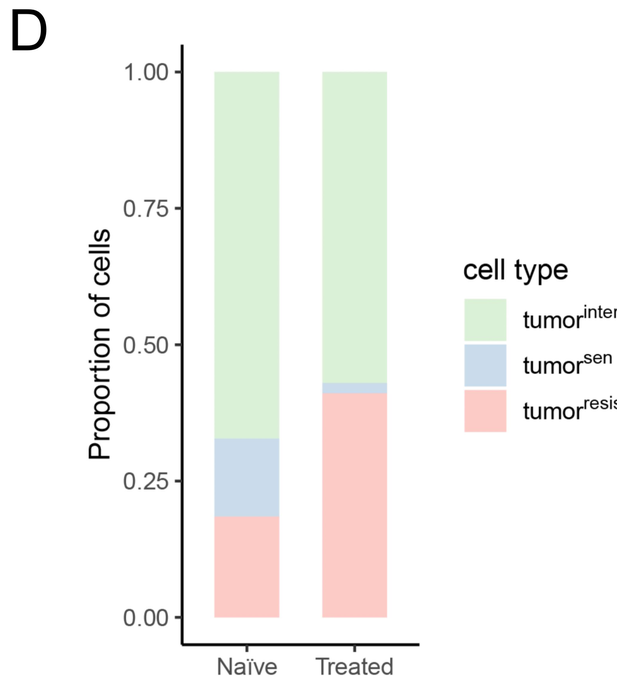
D
Proportion of cells
Naïve
Treated
cell type
tumorinter
tumorsen
tumorresist

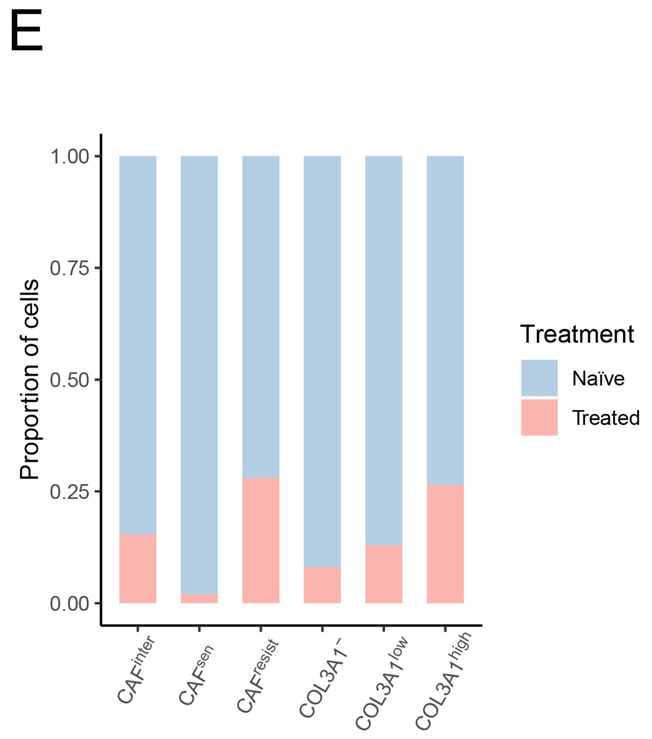
E
Proportion of cells
CAFinter
CAFsen
CAFresist
COL3A1-
COL3A1low
COL3A1high
Treatment
Naïve
Treated

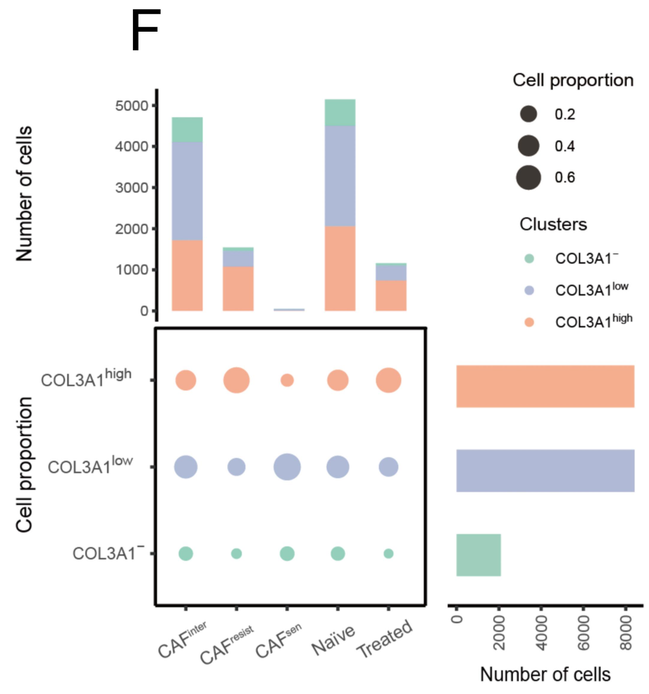
F
Number of cells
Cell proportion
Clusters
COL3A1-
COL3A1low
COL3A1high
CAFinter
CAFresist
CAFsen
Naïve
Treated

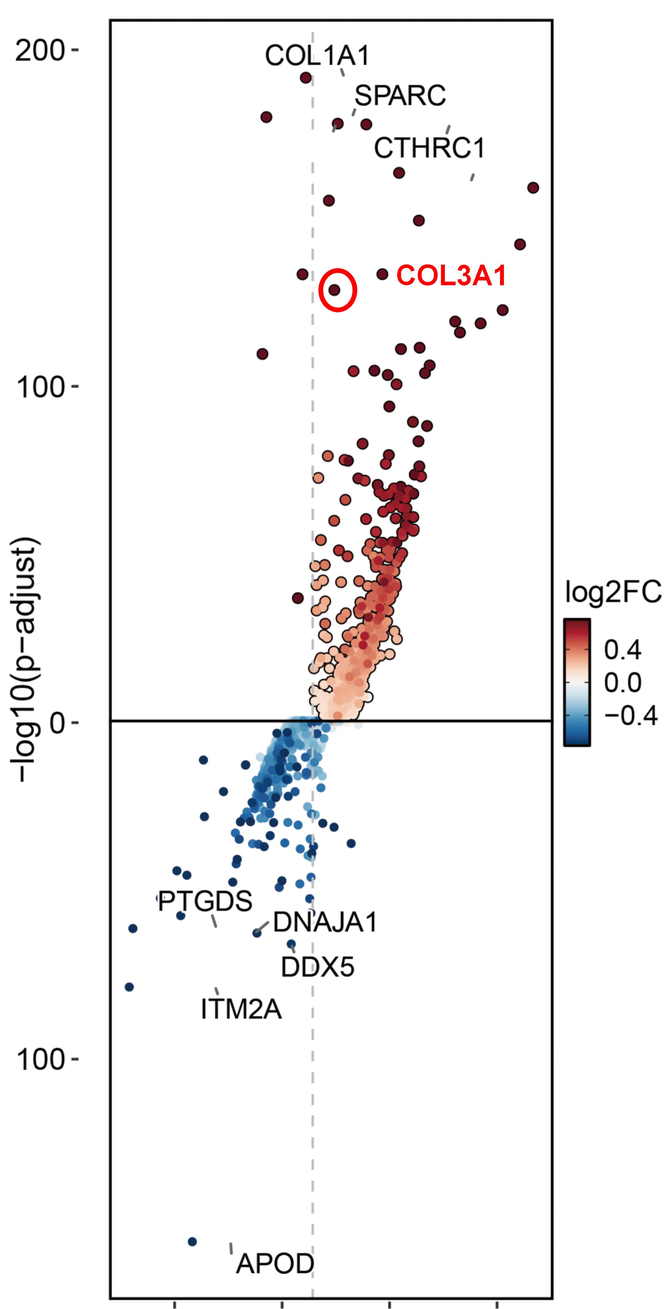
G
COL1A1
SPARC
CTHRC1
COL3A1
PTGDS
DNAJA1
DDX5
ITM2A
APOD
−log10(p−adjust)
logFC
log2FC

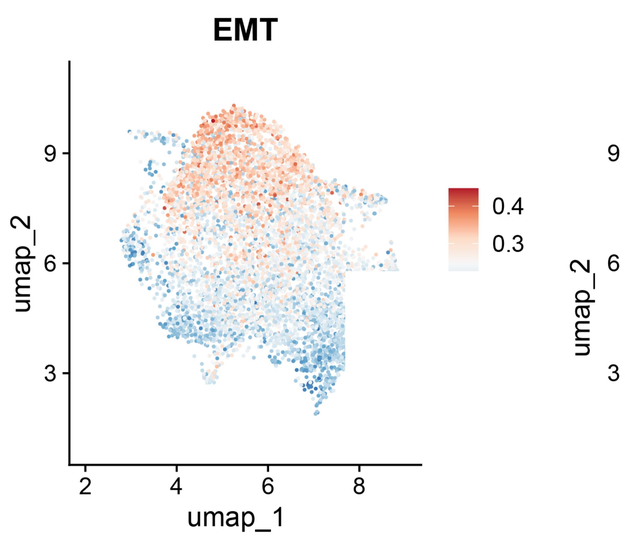
H
EMT
Oxidative phosphorylation
umap_2
umap_1

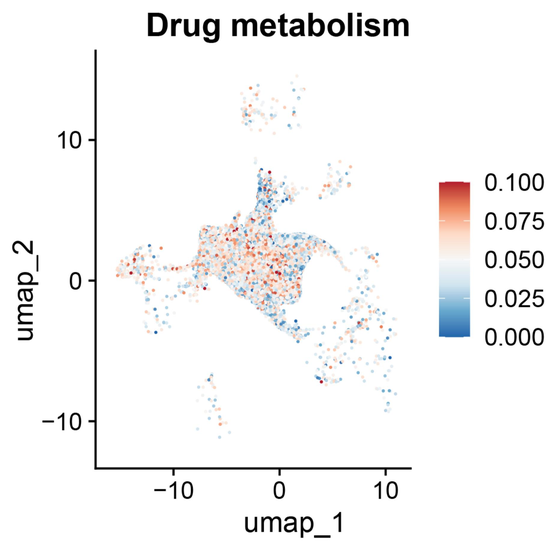
I
Drug metabolism
umap_2
umap_1

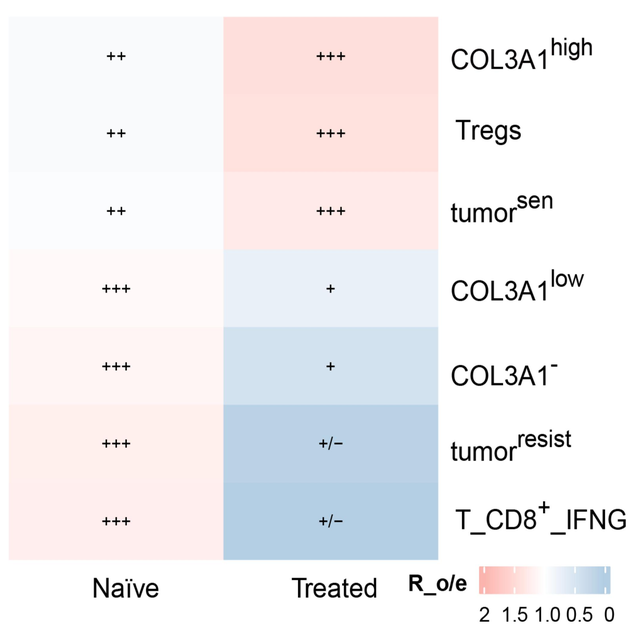
J
COL3A1high
Tregs
tumorsen
COL3A1low
COL3A1-
tumorresist
T_CD8+_IFNG
Naïve
Treated
R_o/e

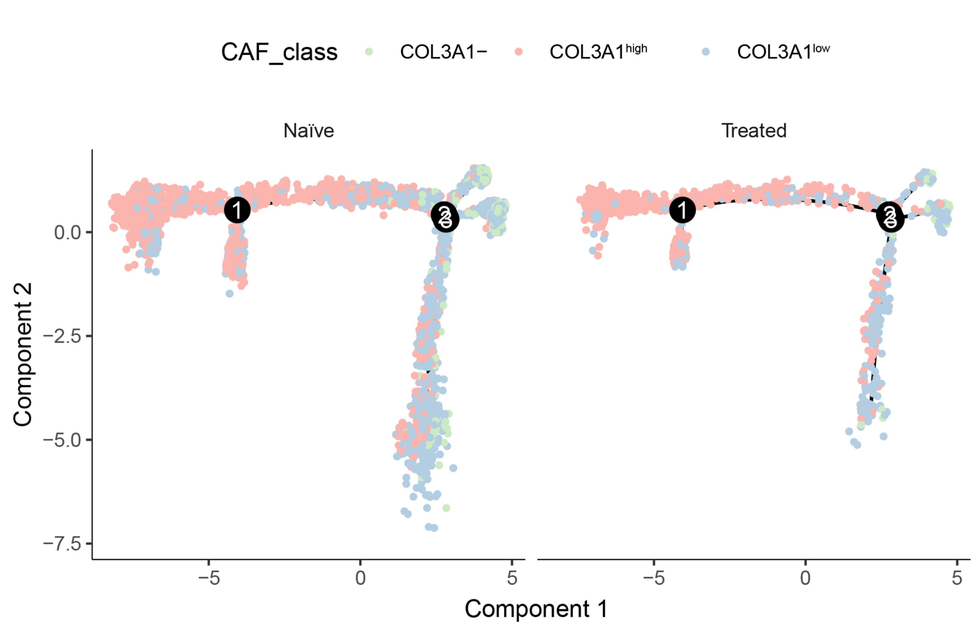
K
CAF_class
COL3A1−
COL3A1high
COL3A1low
Naïve
Treated
Component 1
Component 2

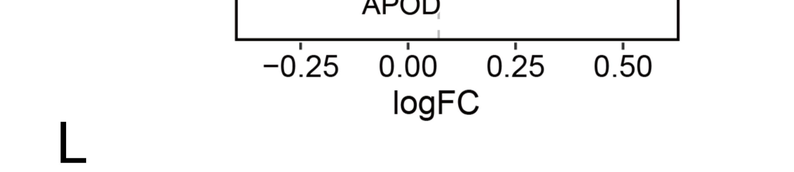
L
PTX
MDA-MB-231
CP-H172_shCOL3A1
NC #1 #2 NC #1 #2
Snail
E-Cadherin
N-Cadherin
Vimentin
β-ACTIN

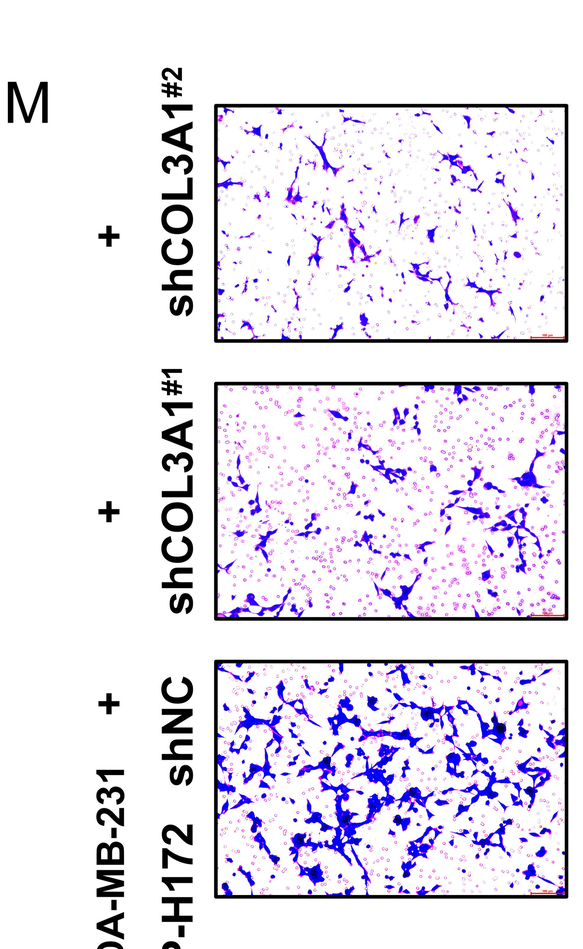
M
shCOL3A1#2
shCOL3A1#1
shNC
MDA-MB-231
CP-H172

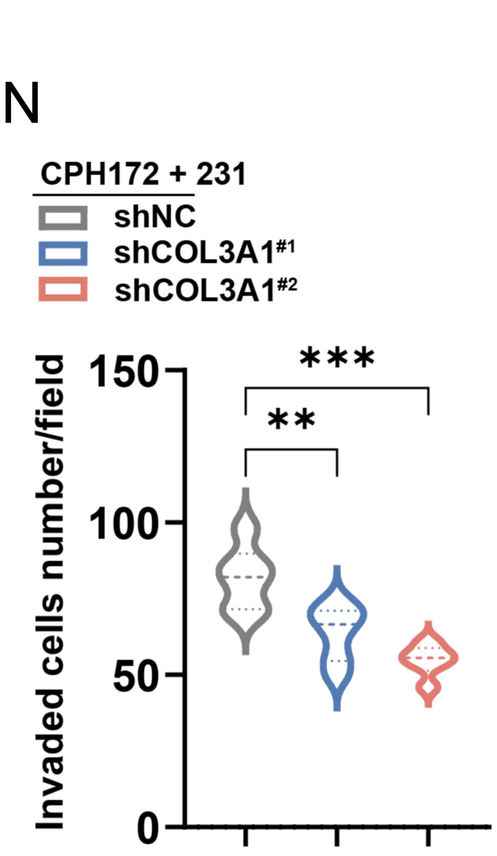
N
CPH172 + 231
shNC
shCOL3A1#1
shCOL3A1#2
Invaded cells number/field

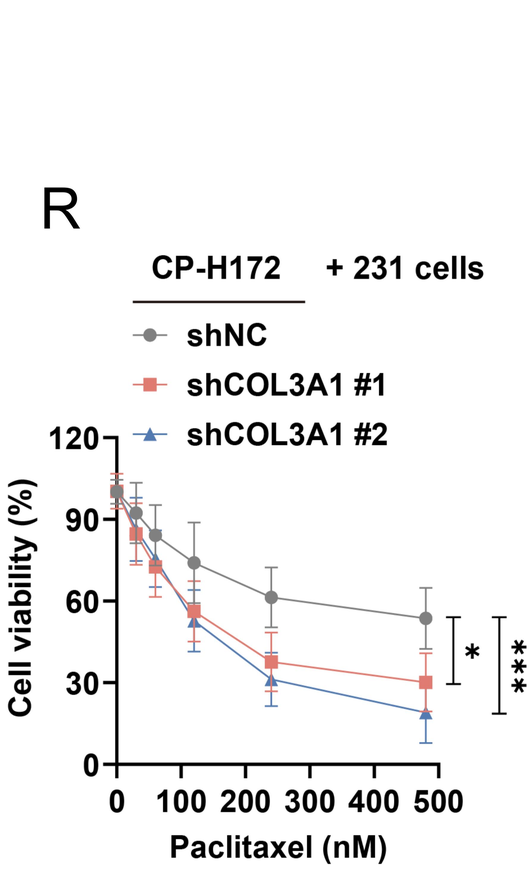
R
CP-H172 + 231 cells
shNC
shCOL3A1 #1
shCOL3A1 #2
Cell viability (%)
Paclitaxel (nM)

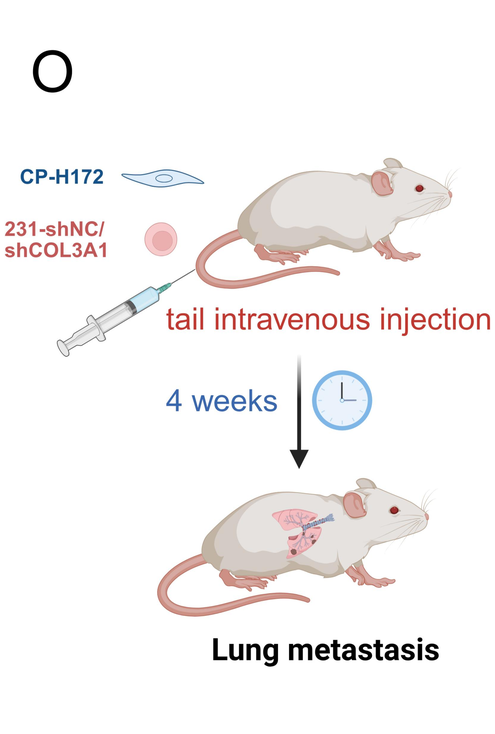
O
CP-H172
231-shNC/
shCOL3A1
tail intravenous injection
4 weeks
Lung metastasis

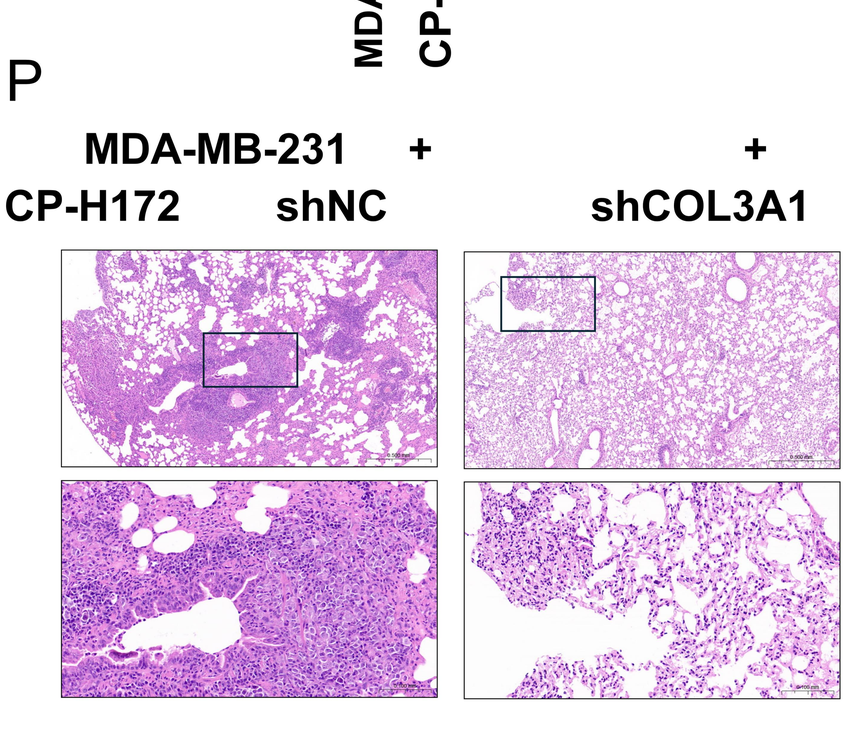
P
MDA-MB-231 +
CP-H172 shNC
+ shCOL3A1

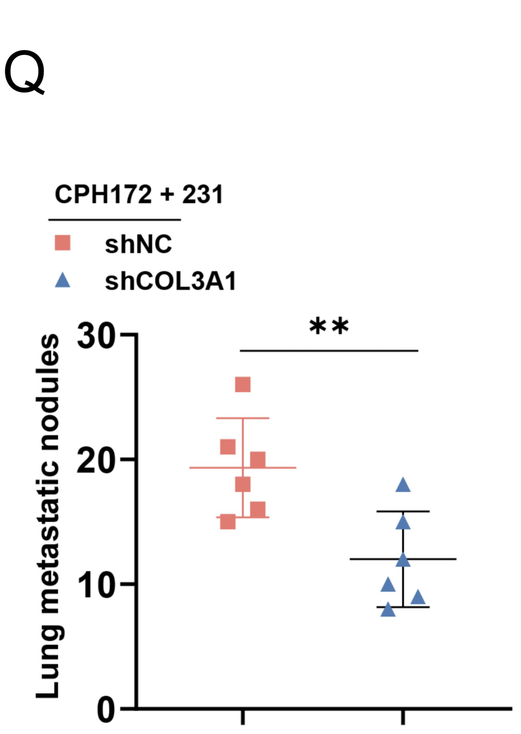
Q
CPH172 + 231
shNC
shCOL3A1
Lung metastatic nodules

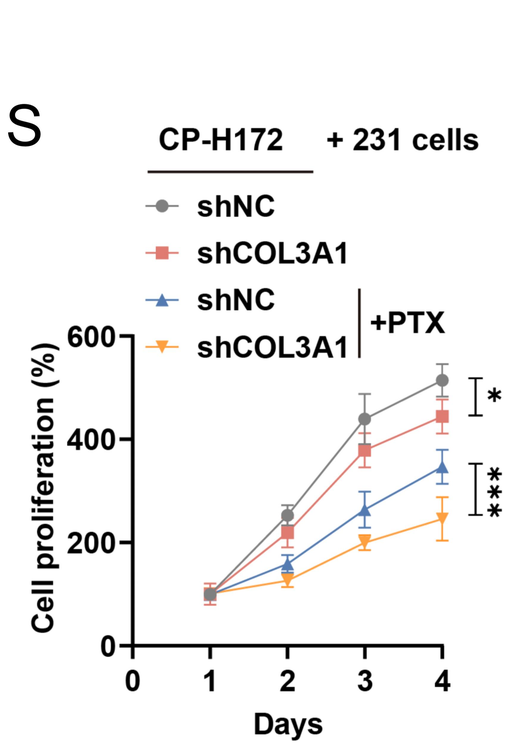
S
CP-H172 + 231 cells
shNC
shCOL3A1
shNC
shCOL3A1
+PTX
Cell proliferation (%)
Days

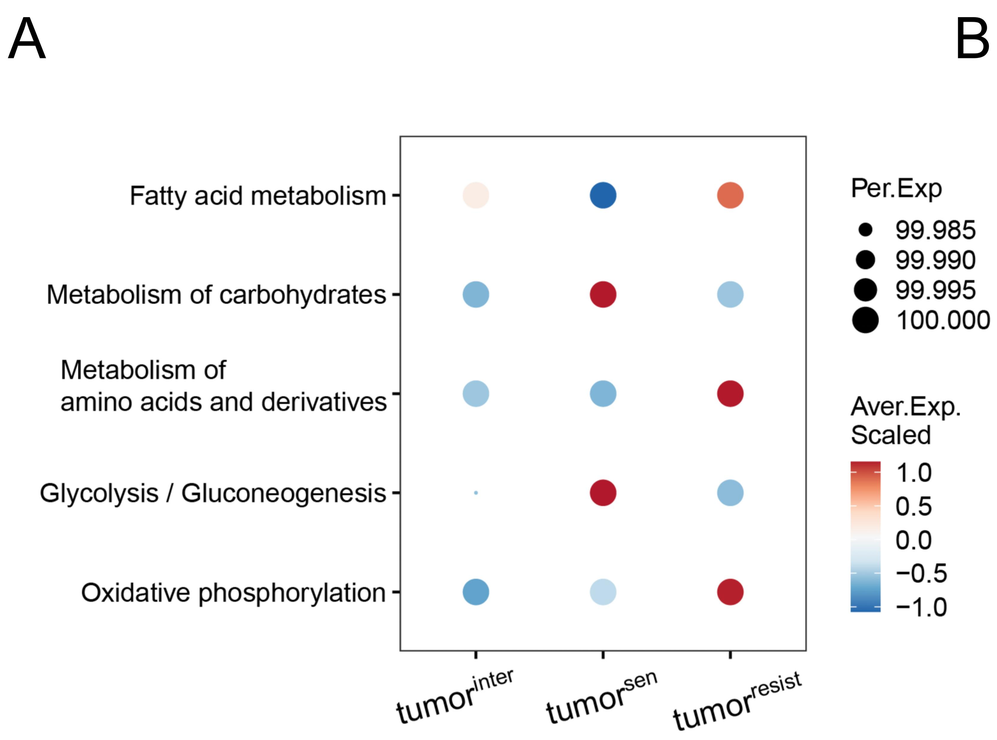
A
Fatty acid metabolism
Metabolism of carbohydrates
Metabolism of amino acids and derivatives
Glycolysis / Gluconeogenesis
Oxidative phosphorylation
tumor^inter
tumor^sen
tumor^resist
Per.Exp
99.985
99.990
99.995
100.000
Aver.Exp. Scaled
1.0
0.5
0.0
−0.5
−1.0

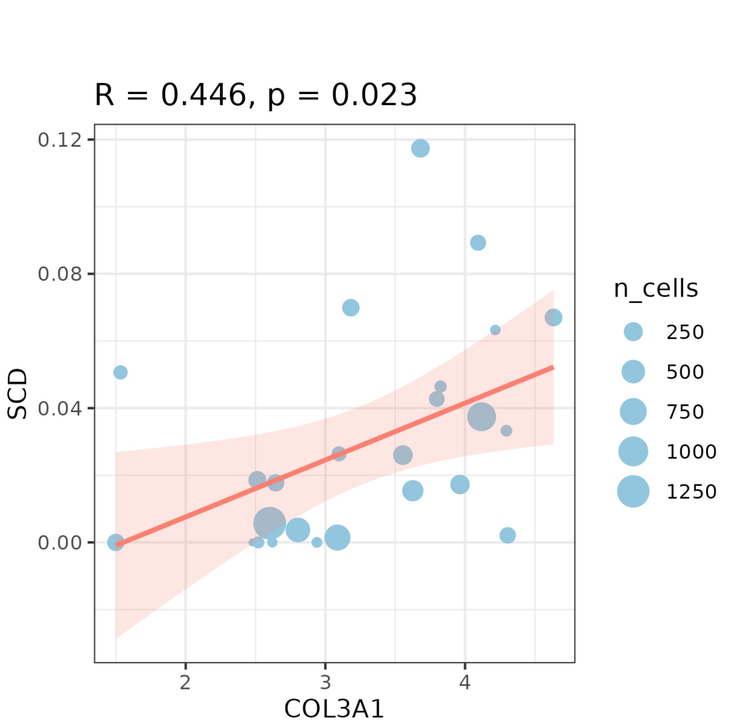
B
R = 0.446, p = 0.023
SCD
COL3A1
n_cells
250
500
750
1000
1250

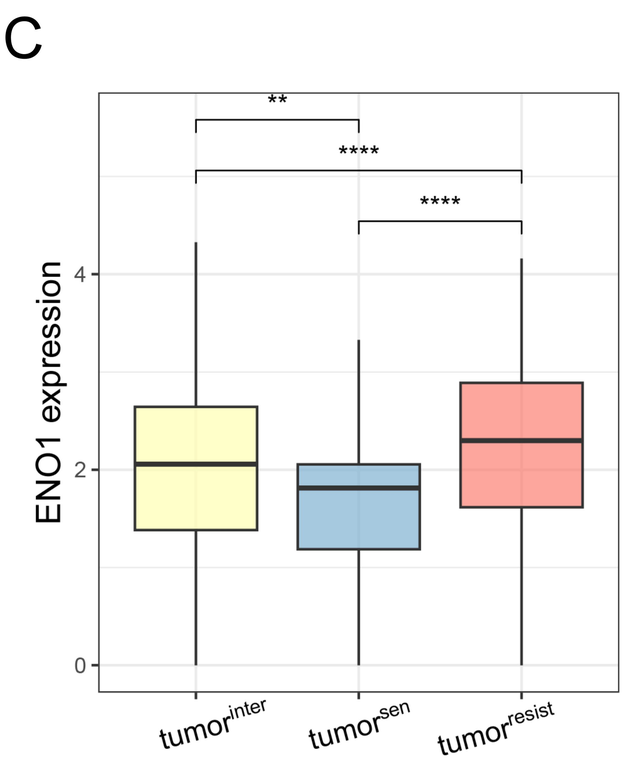
C
ENO1 expression
**
****
****
tumor^inter
tumor^sen
tumor^resist

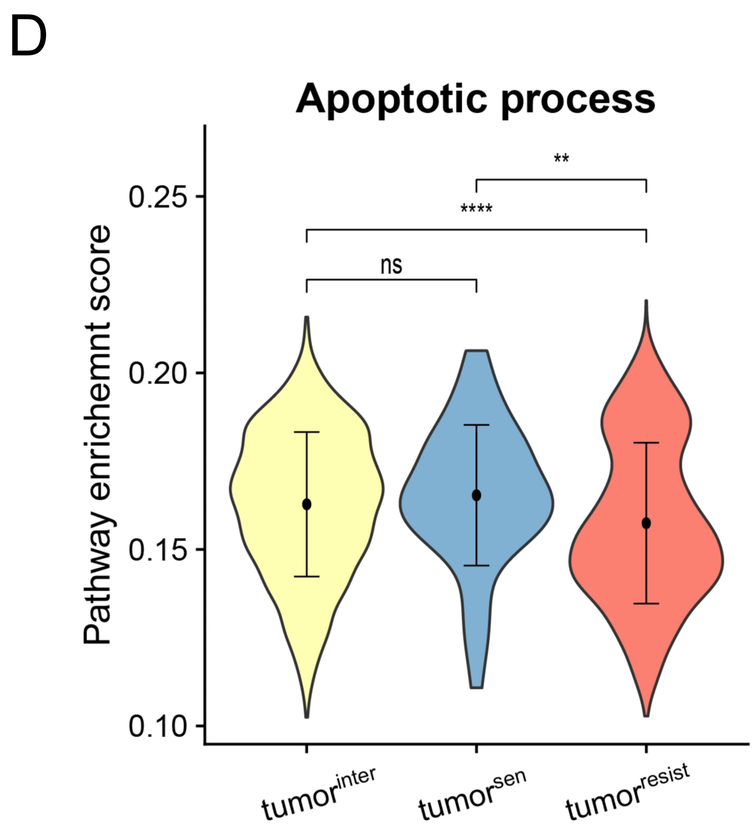
D
Apoptotic process
Pathway enrichemnt score
ns
**
****
tumor^inter
tumor^sen
tumor^resist

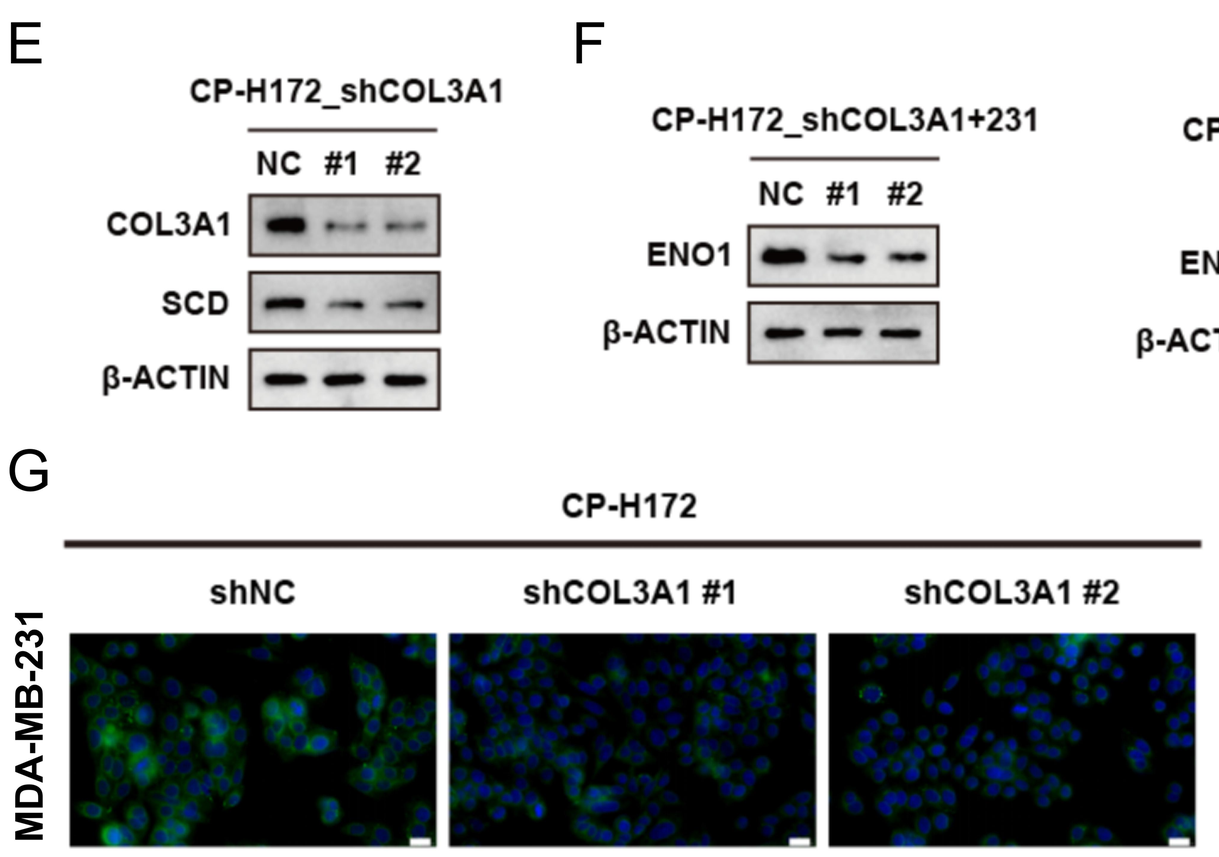
E
CP-H172_shCOL3A1
NC #1 #2
COL3A1
SCD
β-ACTIN
F
CP-H172_shCOL3A1+231
CP-H172_shCOL3A1+453
ENO1
β-ACTIN
G
CP-H172
shNC
shCOL3A1 #1
shCOL3A1 #2
MDA-MB-231
Relative fluorescence intensity
shNC shCOL3A1

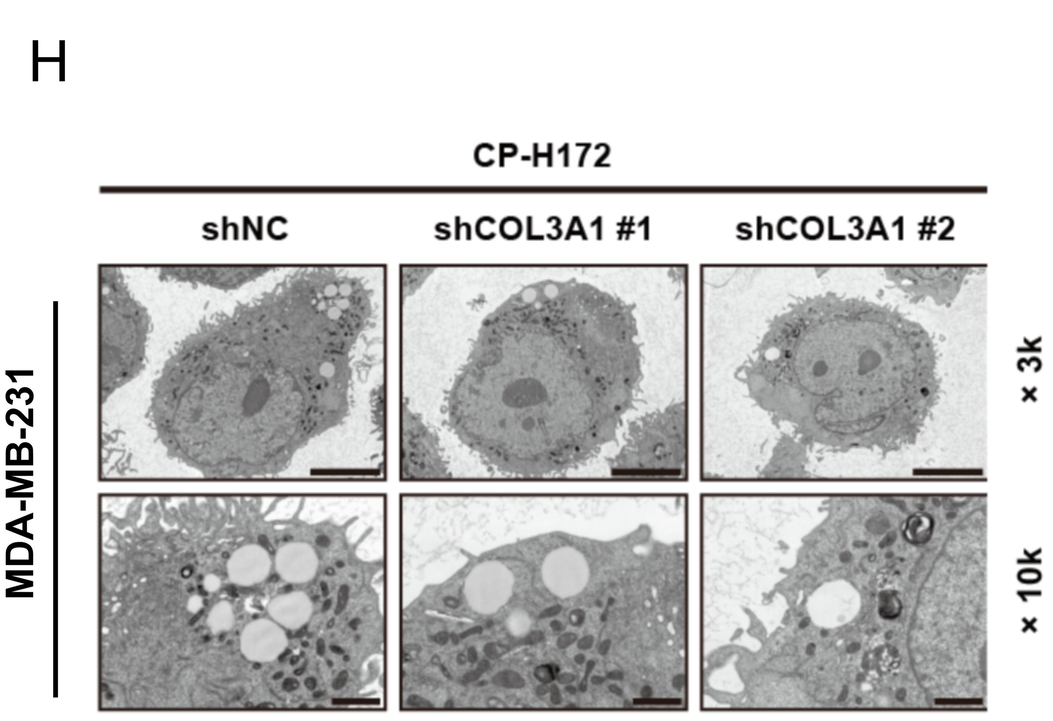
H
CP-H172
shNC
shCOL3A1 #1
shCOL3A1 #2
MDA-MB-231
× 3k
× 10k

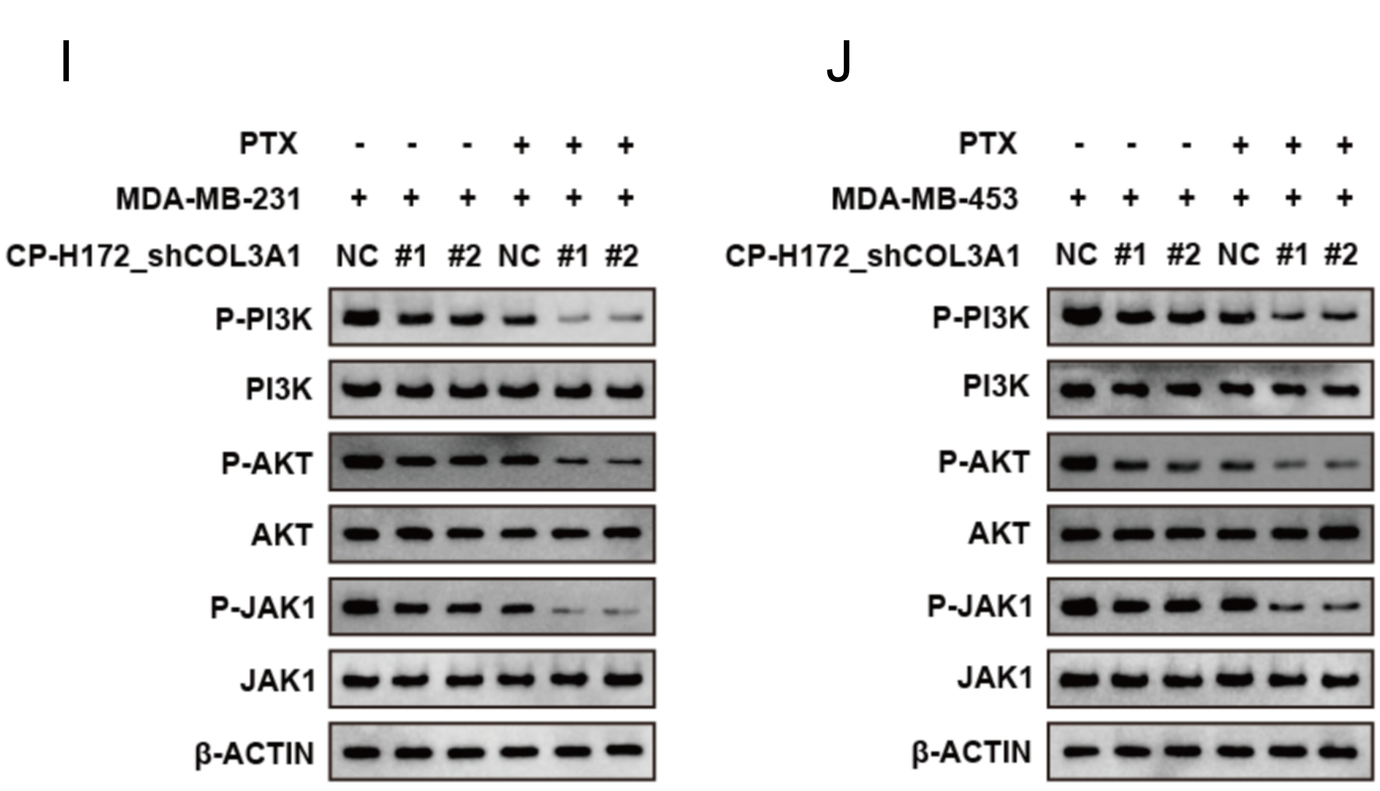
I
PTX
MDA-MB-231
CP-H172_shCOL3A1
NC #1 #2 NC #1 #2
P-PI3K
PI3K
P-AKT
AKT
P-JAK1
JAK1
β-ACTIN
J
MDA-MB-453

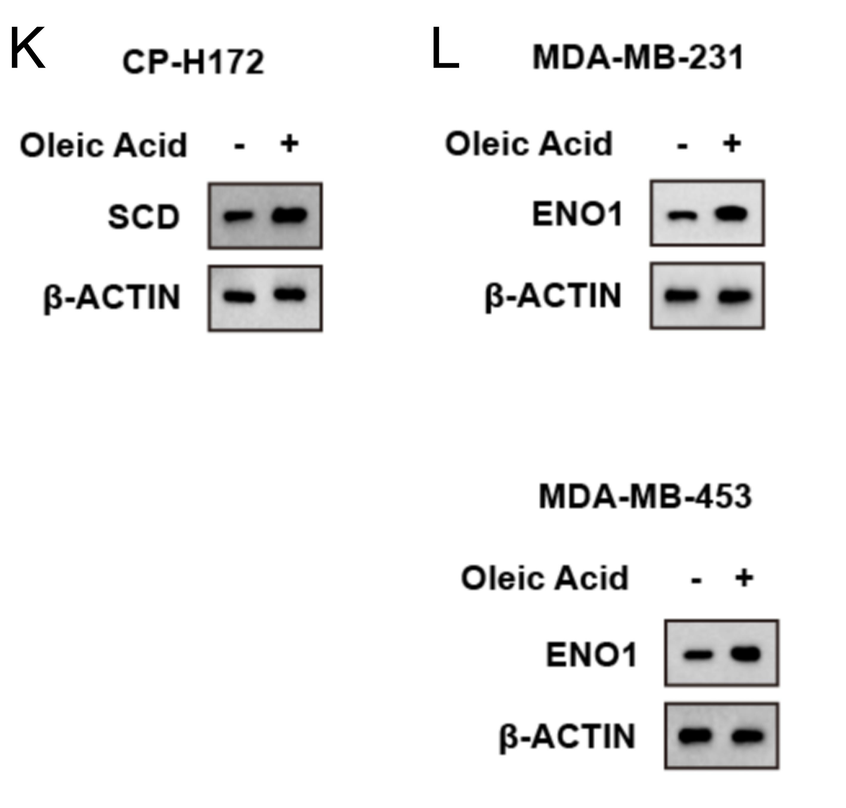
K
CP-H172
Oleic Acid
SCD
β-ACTIN
MDA-MB-453
ENO1

L
MDA-MB-231
Oleic Acid
ENO1
β-ACTIN

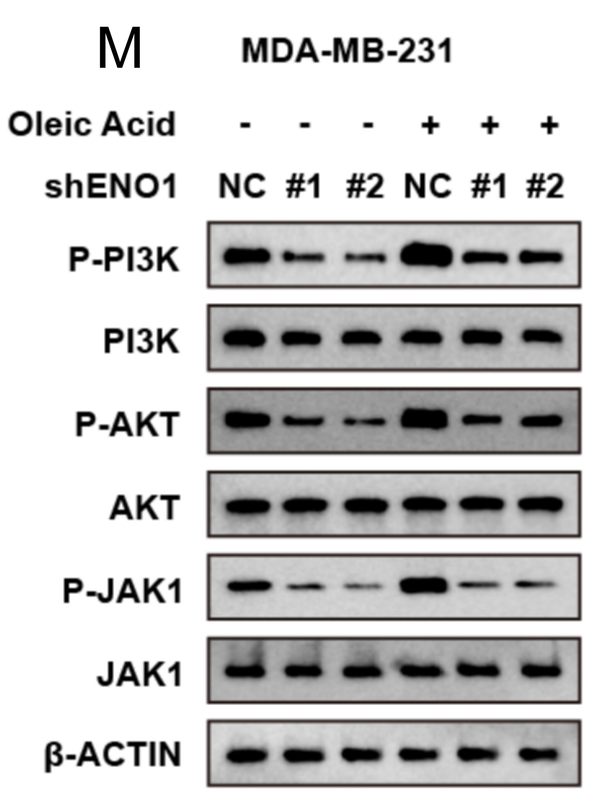
M
MDA-MB-231
Oleic Acid
shENO1
NC #1 #2 NC #1 #2
P-PI3K
PI3K
P-AKT
AKT
P-JAK1
JAK1
β-ACTIN

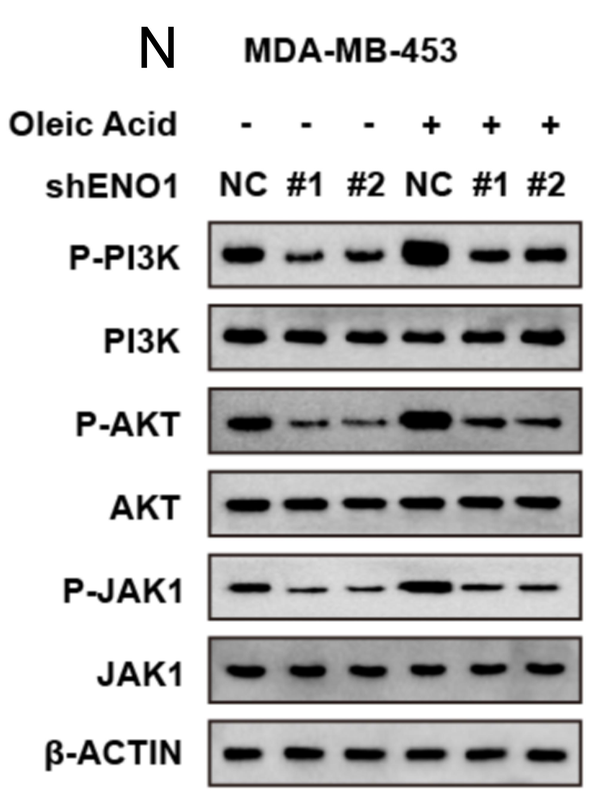
N
MDA-MB-453

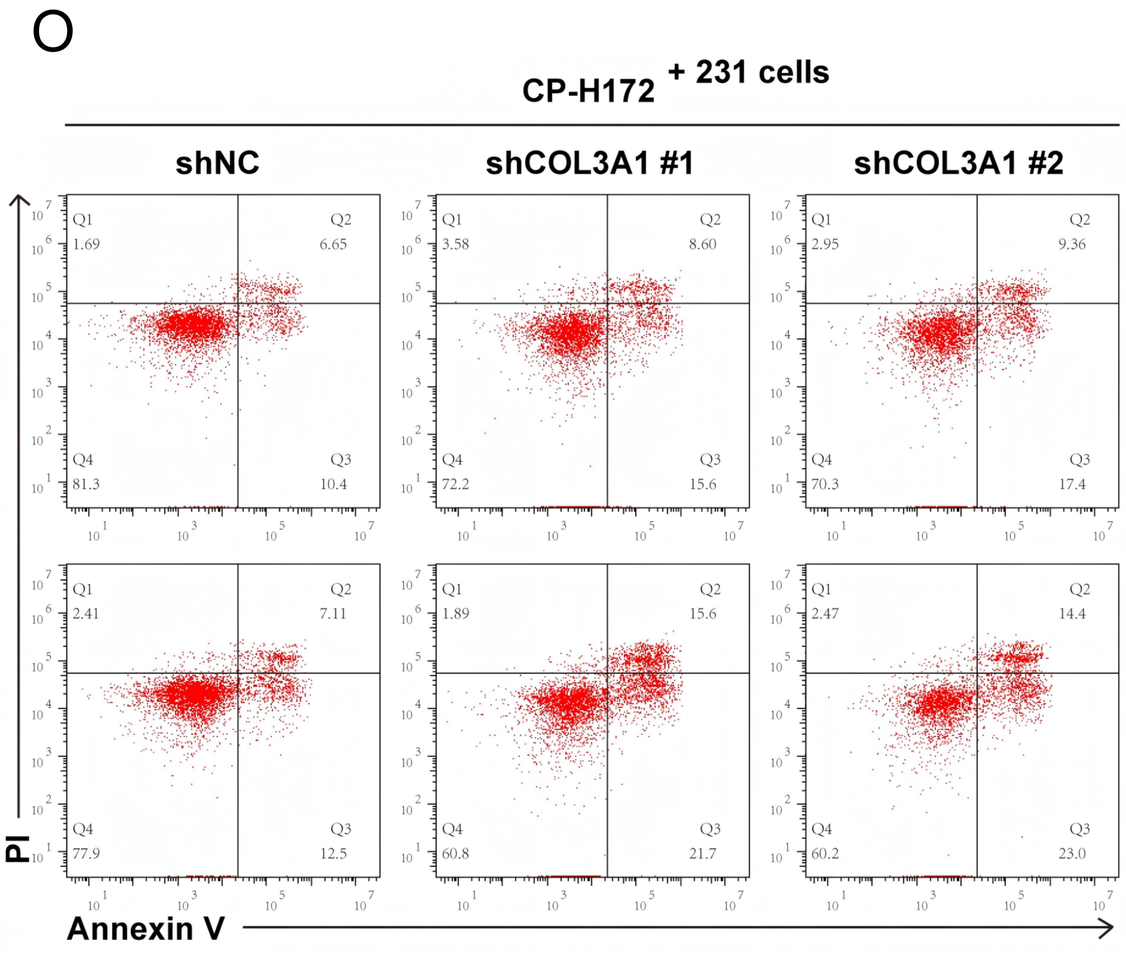
O
CP-H172 + 231 cells
shNC
shCOL3A1 #1
shCOL3A1 #2
Ctrl
PTX
PI
Annexin V
Q1 1.69
Q2 6.65
Q4 81.3
Q3 10.4
Q1 3.58
Q2 8.60
Q4 72.2
Q3 15.6
Q1 2.95
Q2 9.36
Q4 70.3
Q3 17.4
Q1 2.41
Q2 7.11
Q4 77.9
Q3 12.5
Q1 1.89
Q2 15.6
Q4 60.8
Q3 21.7
Q1 2.47
Q2 14.4
Q4 60.2
Q3 23.0

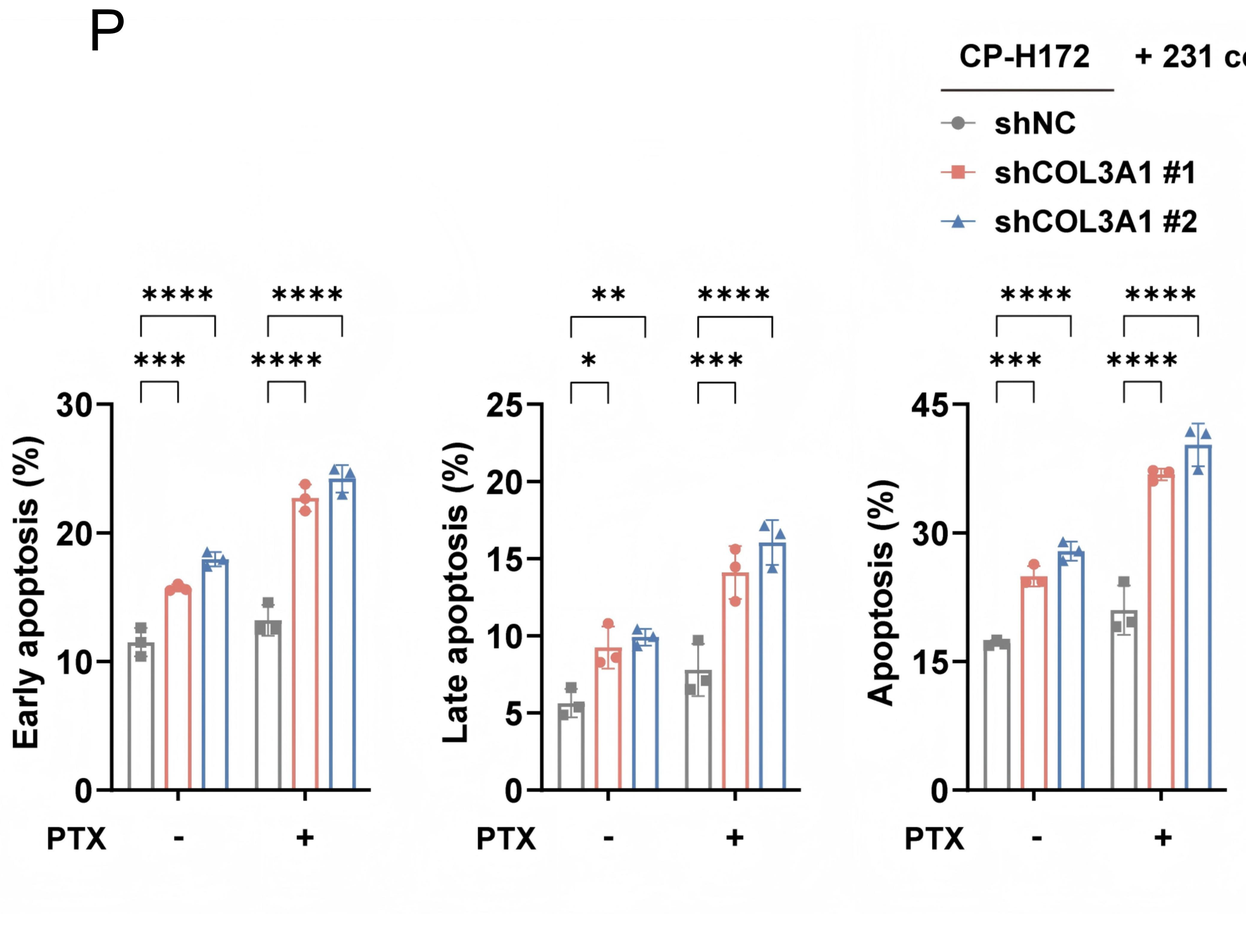
P
CP-H172 + 231 cells
shNC
shCOL3A1 #1
shCOL3A1 #2
Early apoptosis (%)
Late apoptosis (%)
Apoptosis (%)
PTX - +

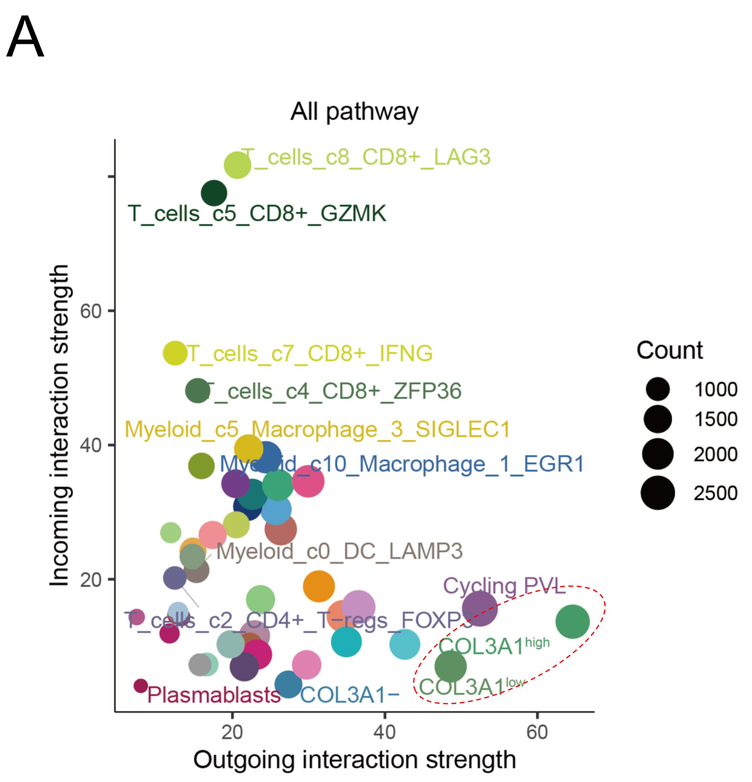
A
All pathway
T_cells_c8_CD8+_LAG3
T_cells_c5_CD8+_GZMK
T_cells_c7_CD8+_IFNG
T_cells_c4_CD8+_ZFP36
Myeloid_c5_Macrophage_3_SIGLEC1
Myeloid_c10_Macrophage_1_EGR1
Myeloid_c0_DC_LAMP3
Cycling PVL
T_cells_c2_CD4+_T-regs_FOXP3
COL3A1high
COL3A1low
Plasmablasts
COL3A1−
Count
1000
1500
2000
2500
Incoming interaction strength
Outgoing interaction strength

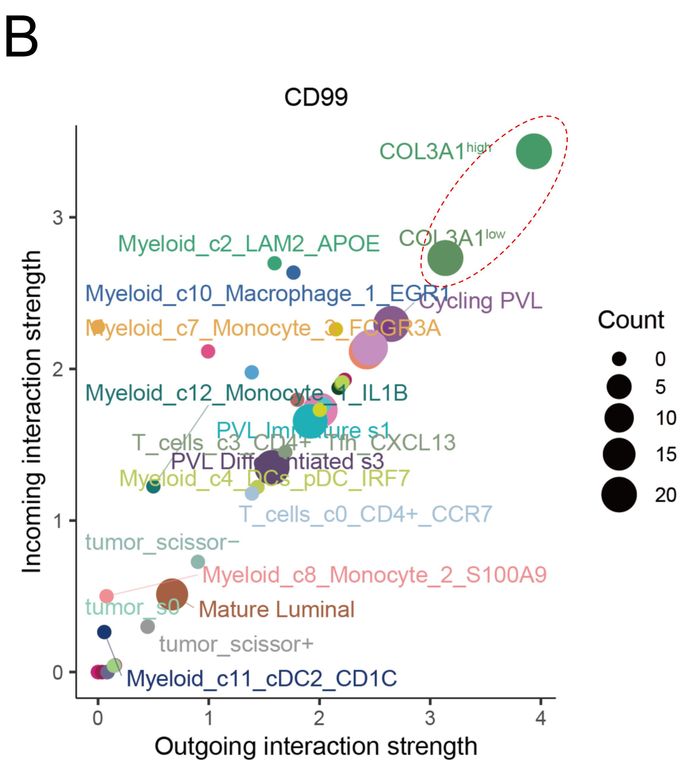
B
CD99
COL3A1high
COL3A1low
Myeloid_c2_LAM2_APOE
Myeloid_c10_Macrophage_1_EGR1
Cycling PVL
Myeloid_c7_Monocyte_3_FCGR3A
Myeloid_c12_Monocyte_1_IL1B
T_cells_c3_CD4+_Tfh_CXCL13
PVL Differentiated s3
Myeloid_c4_DCs_pDC_IRF7
T_cells_c0_CD4+_CCR7
tumor_scissor−
Myeloid_c8_Monocyte_2_S100A9
tumor_s0
Mature Luminal
tumor_scissor+
Myeloid_c11_cDC2_CD1C
Count
0
5
10
15
20
Incoming interaction strength
Outgoing interaction strength

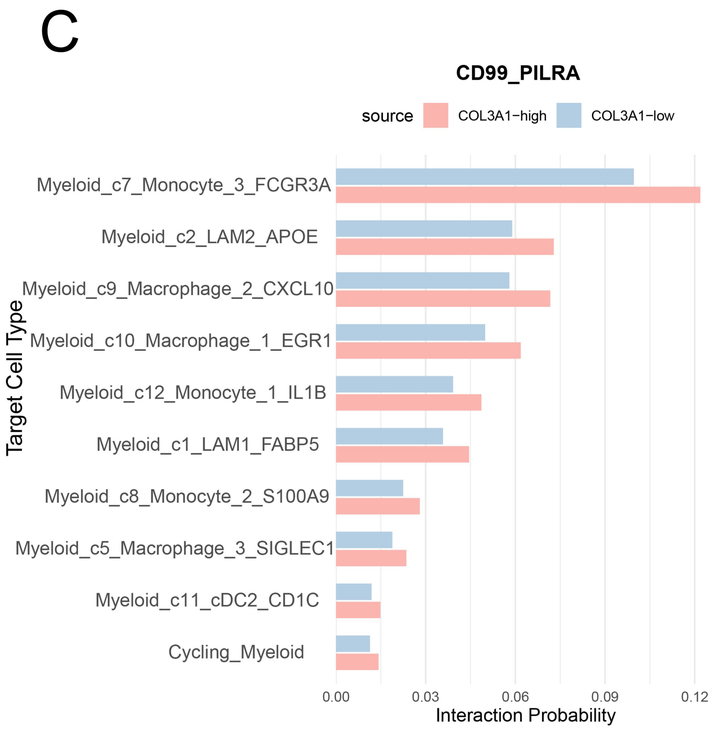
C
CD99_PILRA
source
COL3A1−high
COL3A1−low
Myeloid_c7_Monocyte_3_FCGR3A
Myeloid_c2_LAM2_APOE
Myeloid_c9_Macrophage_2_CXCL10
Myeloid_c10_Macrophage_1_EGR1
Myeloid_c12_Monocyte_1_IL1B
Myeloid_c1_LAM1_FABP5
Myeloid_c8_Monocyte_2_S100A9
Myeloid_c5_Macrophage_3_SIGLEC1
Myeloid_c11_cDC2_CD1C
Cycling_Myeloid
Target Cell Type
Interaction Probability

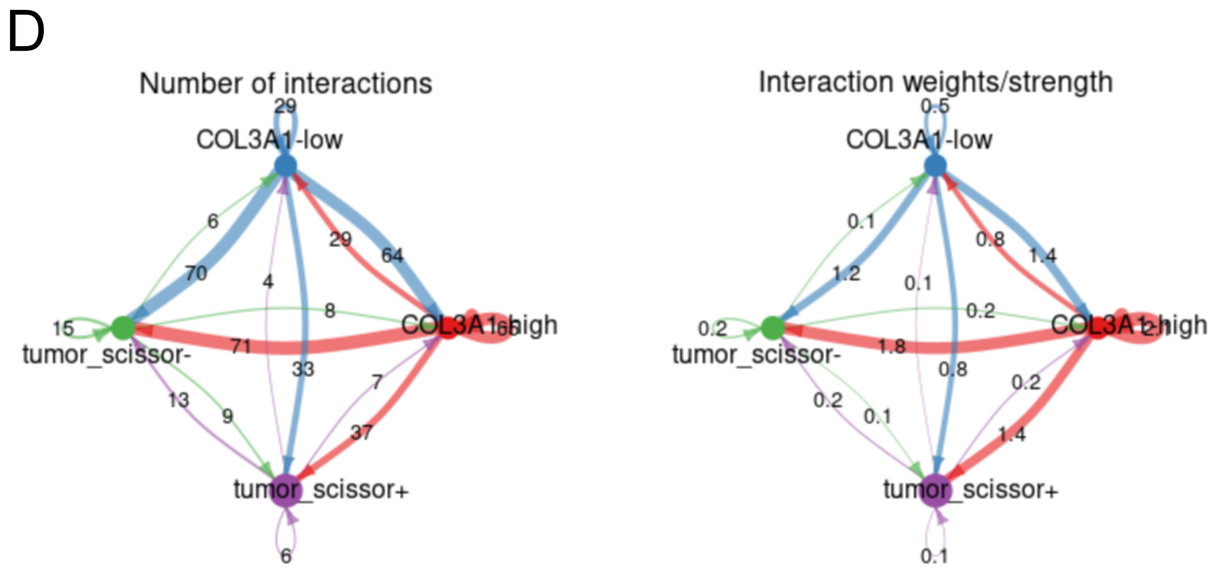
D
Number of interactions
COL3A1-low
COL3A1-high
tumor_scissor-
tumor_scissor+
Interaction weights/strength
COL3A1-low
COL3A1-high
tumor_scissor-
tumor_scissor+

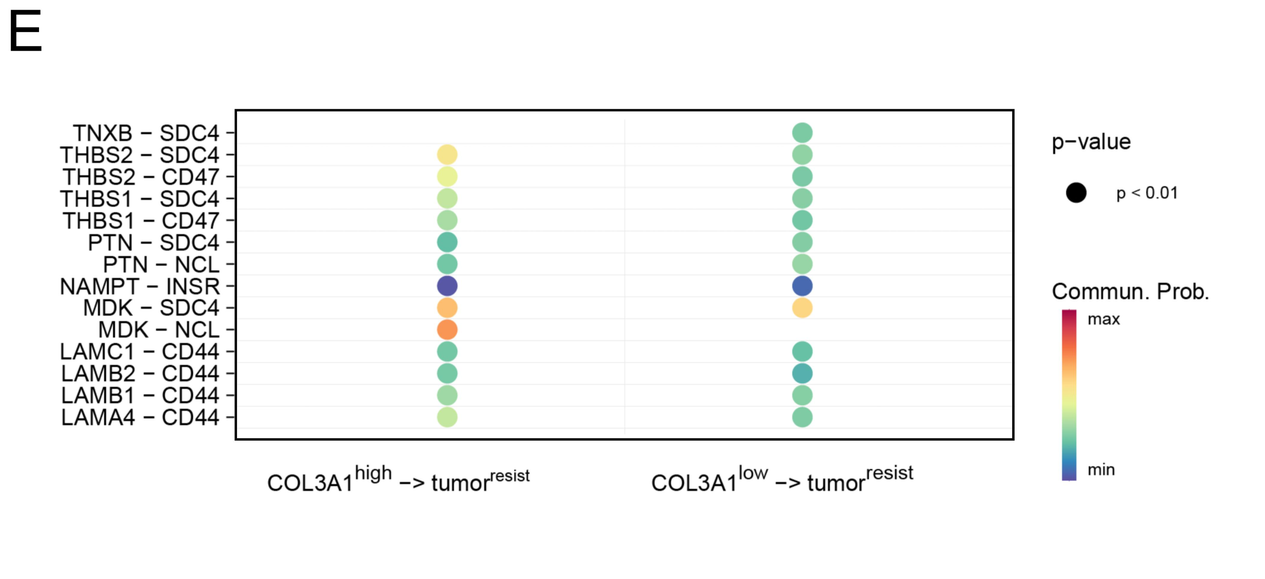
E
TNXB − SDC4
THBS2 − SDC4
THBS2 − CD47
THBS1 − SDC4
THBS1 − CD47
PTN − SDC4
PTN − NCL
NAMPT − INSR
MDK − SDC4
MDK − NCL
LAMC1 − CD44
LAMB2 − CD44
LAMB1 − CD44
LAMA4 − CD44
COL3A1high −> tumorresist
COL3A1low −> tumorresist
p−value
p < 0.01
Commun. Prob.
max
min

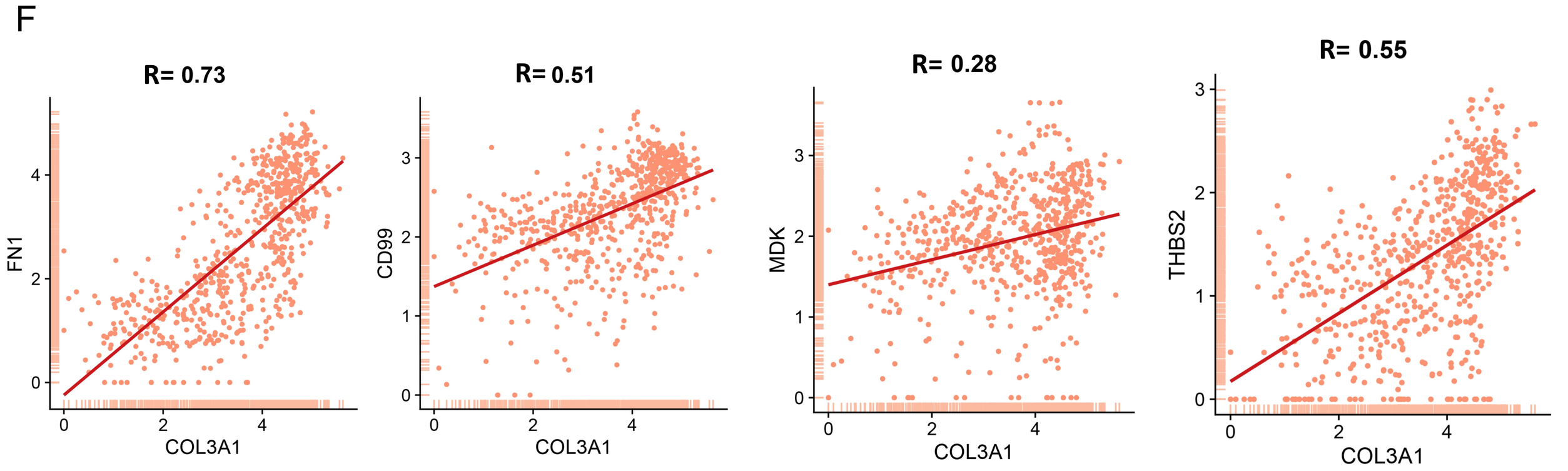
R= 0.73
FN1
COL3A1
R= 0.51
CD99
COL3A1
R= 0.28
MDK
COL3A1
R= 0.55
THBS2
COL3A1

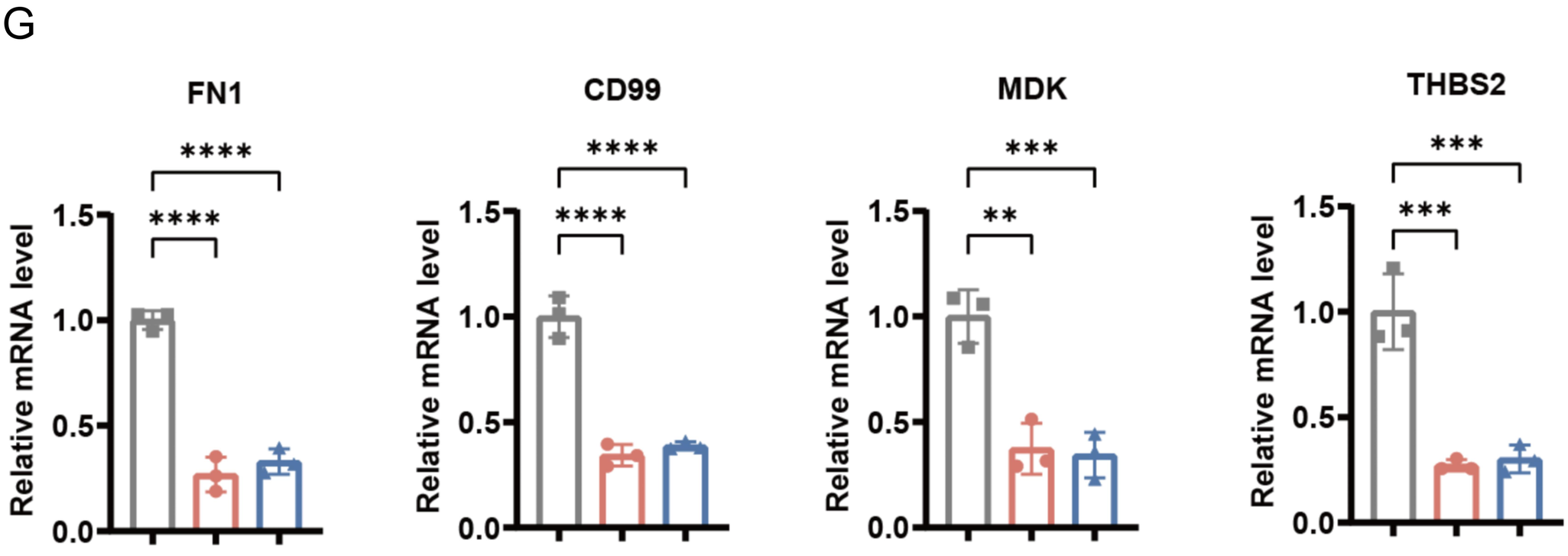
G
FN1
CD99
MDK
THBS2
****
****
**
***
Relative mRNA level
shNC
shCOL3A1 #1
shCOL3A1 #2

A

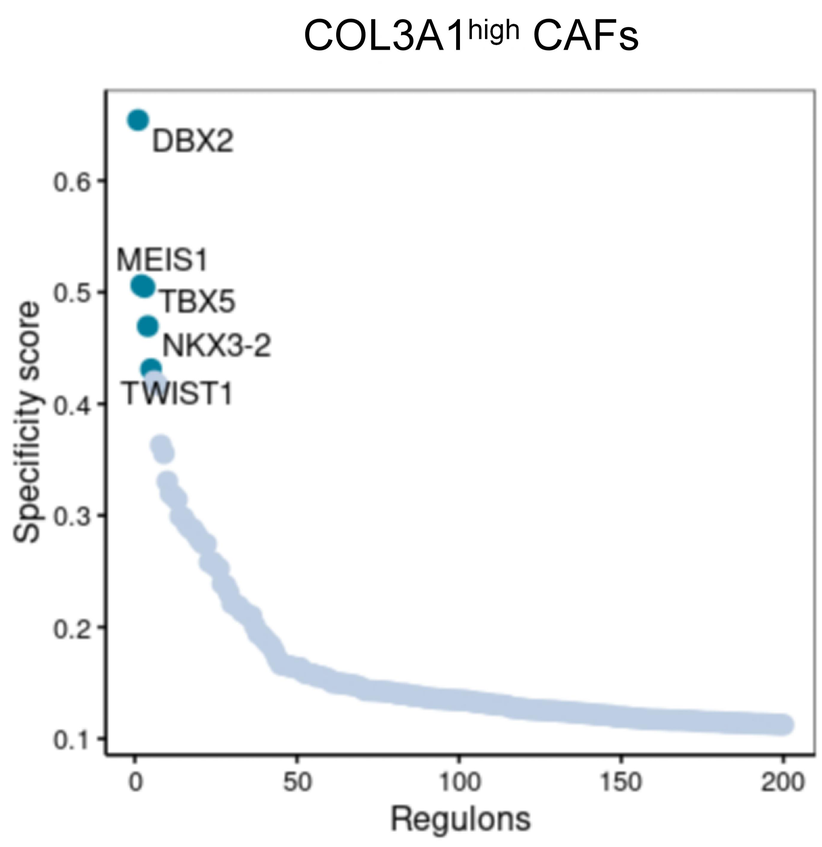
COL3A1high CAFs
DBX2
MEIS1
TBX5
NKX3-2
TWIST1
Specificity score
Regulons
0.6
0.5
0.4
0.3
0.2
0.1
0
50
100
150
200

B

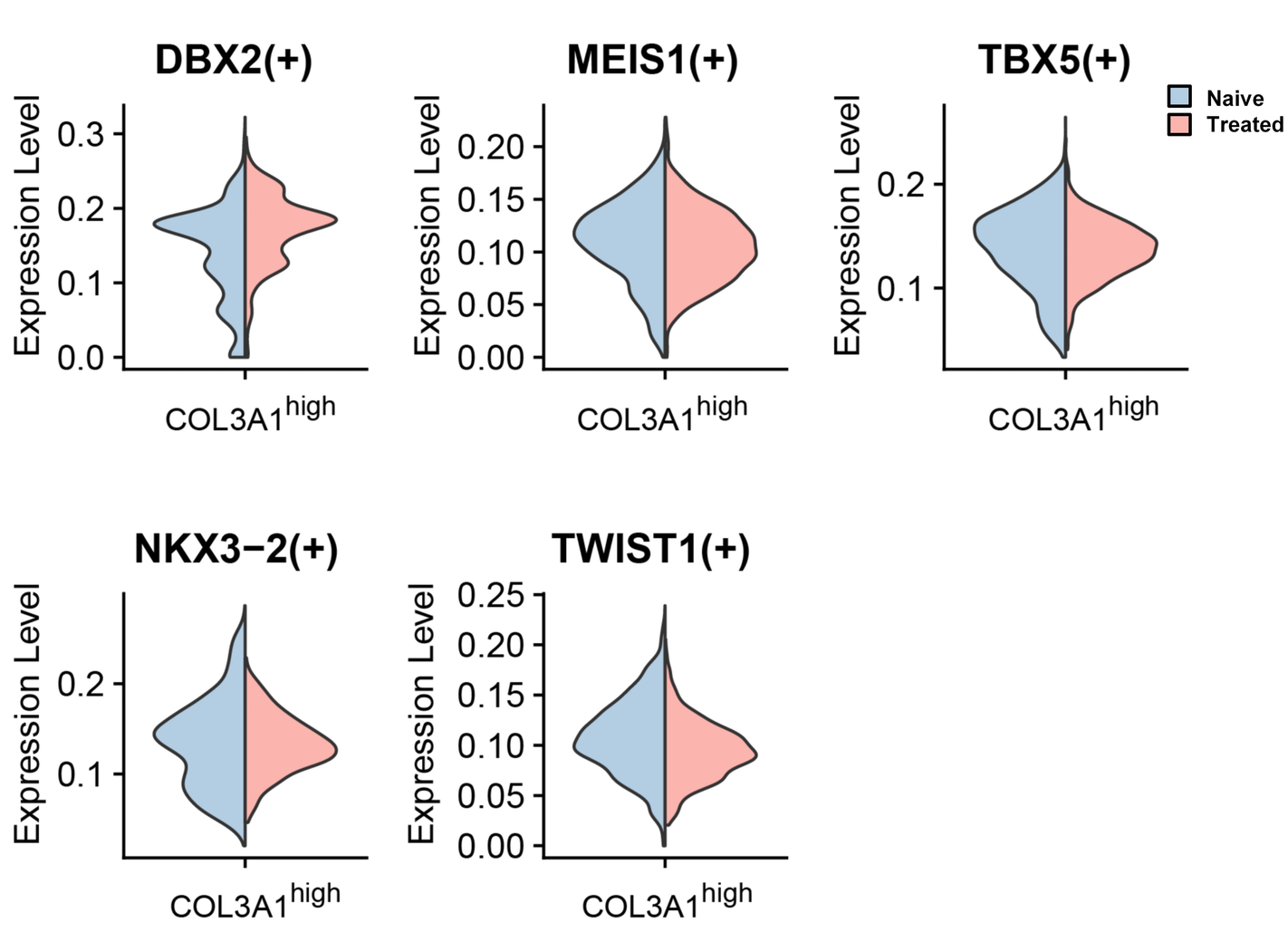
DBX2(+)
MEIS1(+)
TBX5(+)
NKX3−2(+)
TWIST1(+)
Expression Level
COL3A1high
Naive
Treated

C

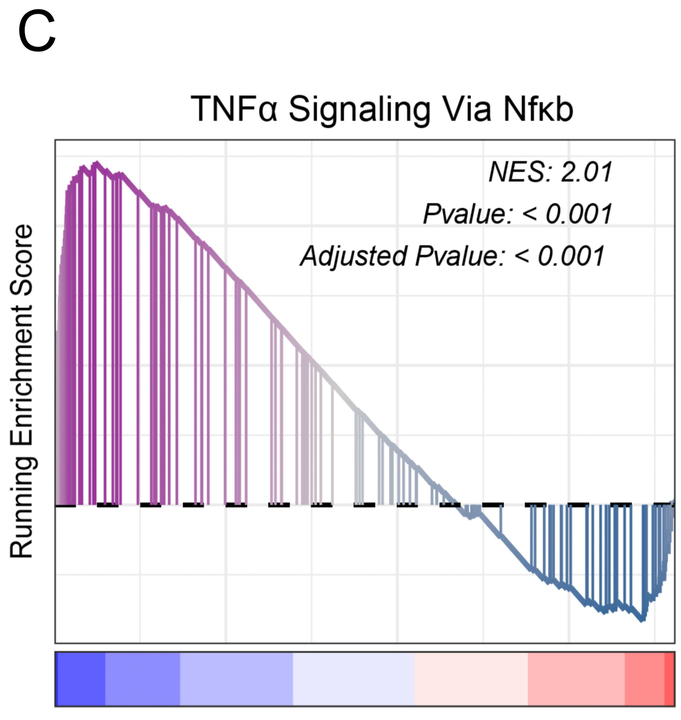
TNFα Signaling Via Nfκb
NES: 2.01
Pvalue: < 0.001
Adjusted Pvalue: < 0.001
Running Enrichment Score

D

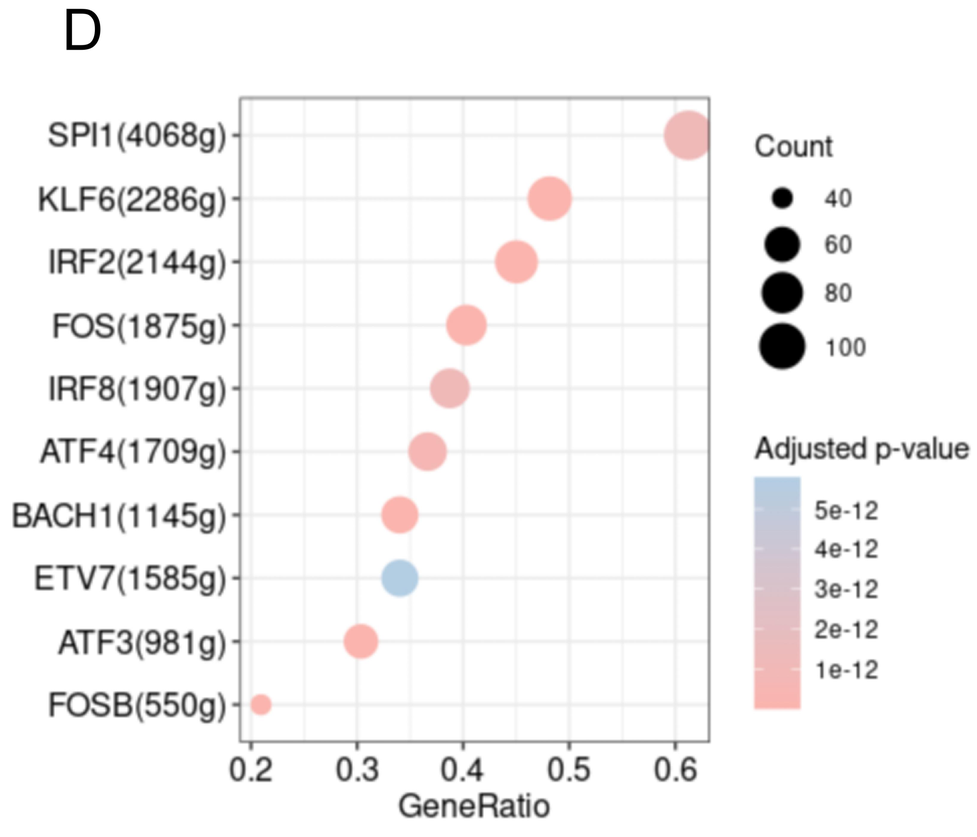
SPI1(4068g)
KLF6(2286g)
IRF2(2144g)
FOS(1875g)
IRF8(1907g)
ATF4(1709g)
BACH1(1145g)
ETV7(1585g)
ATF3(981g)
FOSB(550g)
GeneRatio
Count
40
60
80
100
Adjusted p-value
5e-12
4e-12
3e-12
2e-12
1e-12

F

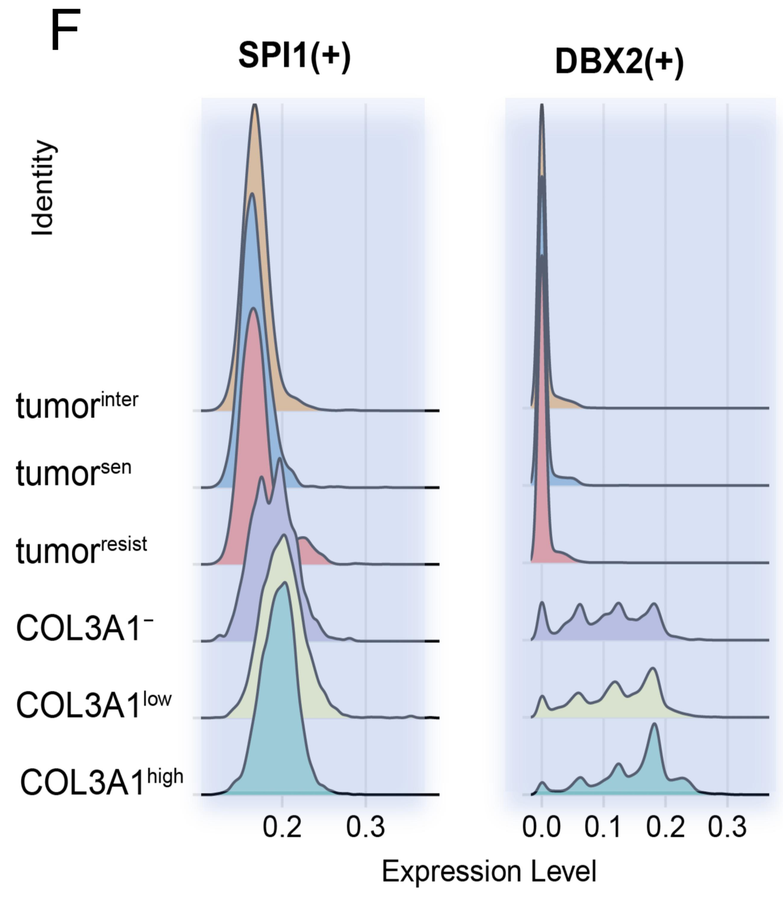
SPI1(+)
DBX2(+)
Identity
tumorinter
tumorsen
tumorresist
COL3A1−
COL3A1low
COL3A1high
Expression Level

E

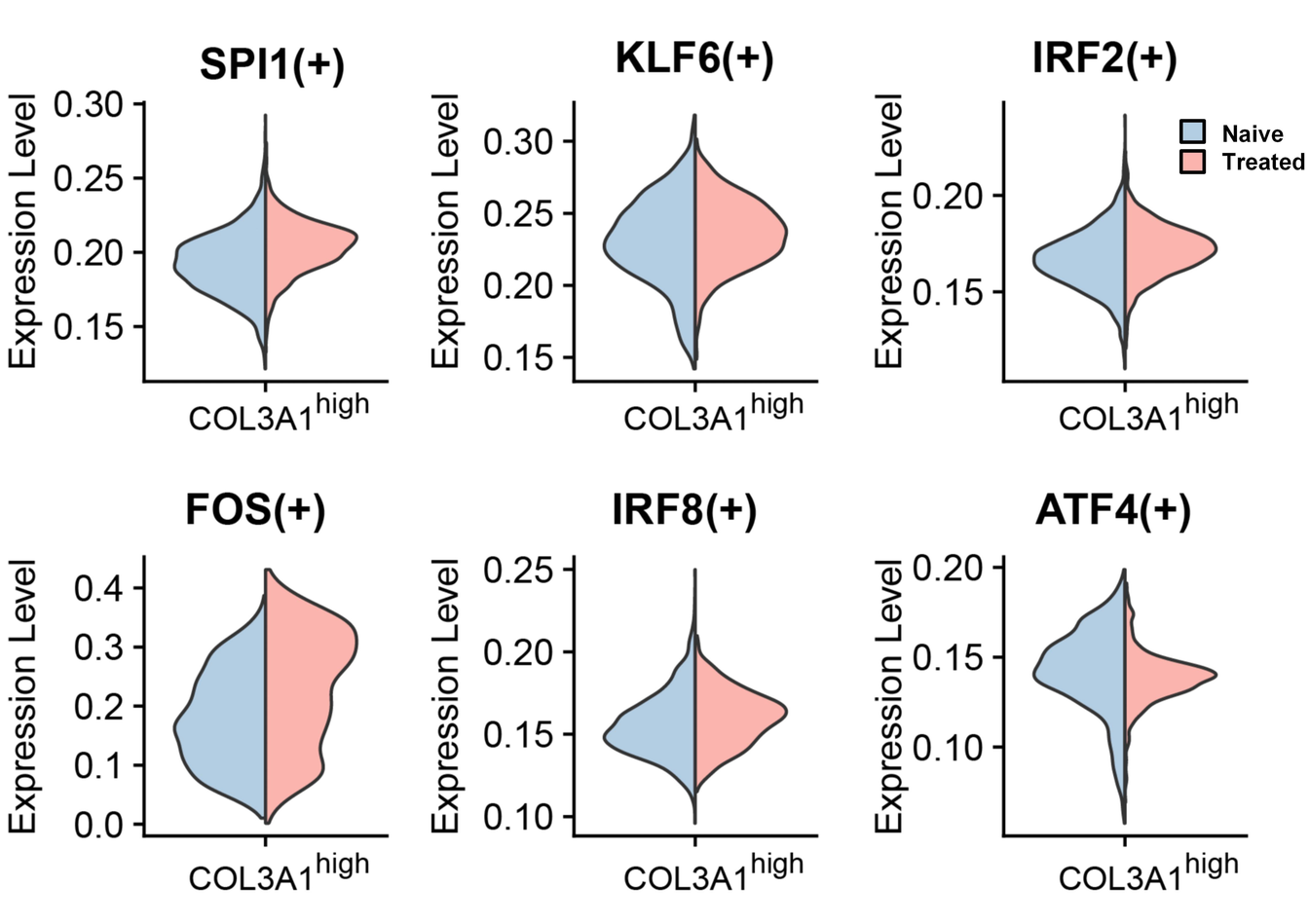
SPI1(+)
KLF6(+)
IRF2(+)
FOS(+)
IRF8(+)
ATF4(+)
Expression Level
COL3A1high
Naive
Treated

G

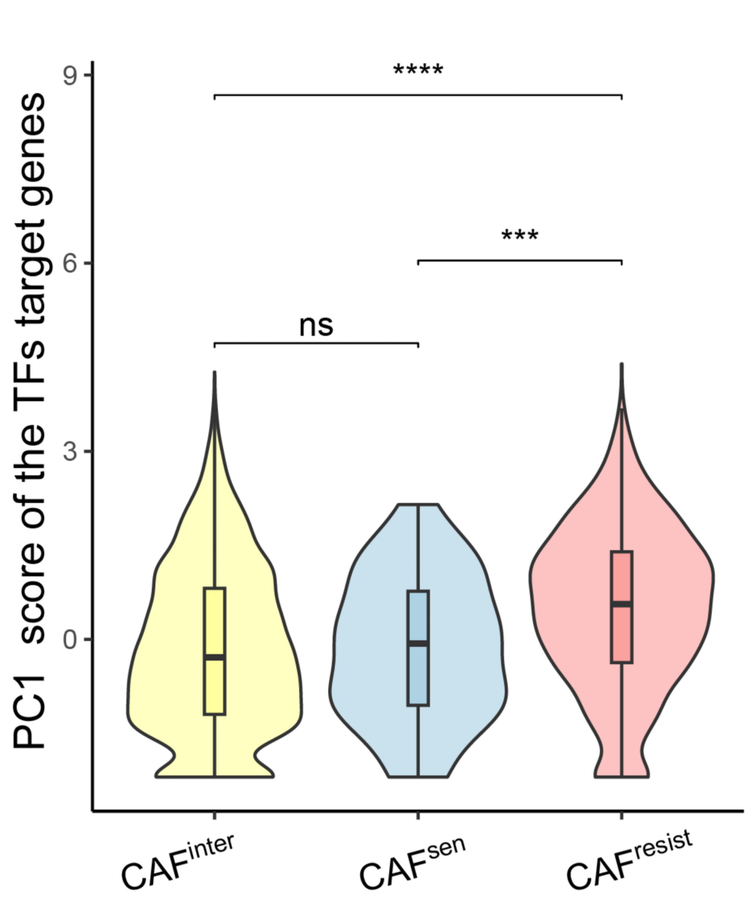
PC1 score of the TFs target genes
****
***
ns
CAFinter
CAFsen
CAFresist

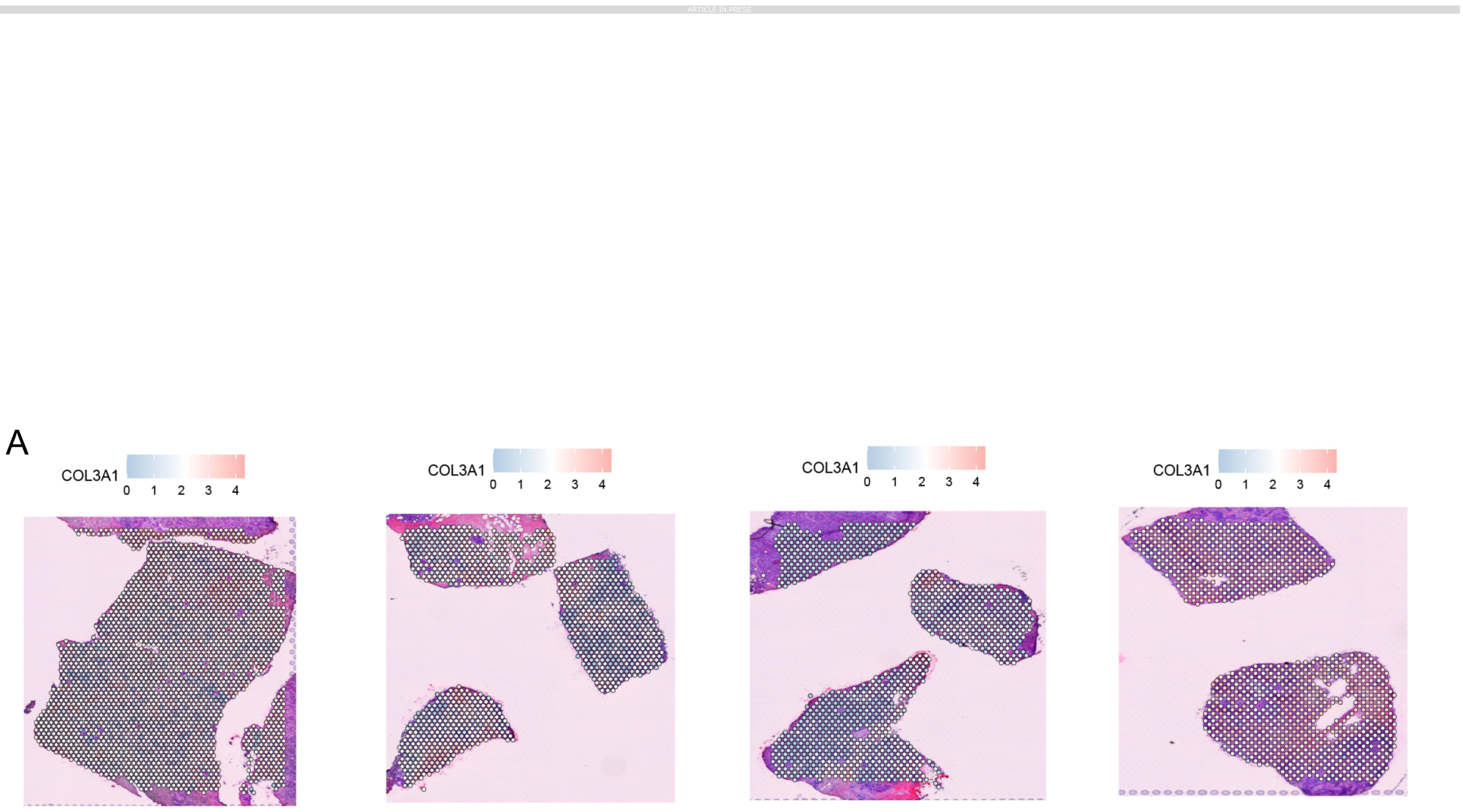
A
COL3A1
0 1 2 3 4
B
tumor^resist
tumor^sen
value
CAF_COL3A1^high
CAF_COL3A1^low
C
Cell−Cell Colocalization
Fraction Rho
D
Paired t−test p = 0.0317
ID CID4290 CID4465 CID44971 CID4535
Fraction Rho
tumor^sen
tumor^resist
E
CR
non_CR
COL3A1
α-SMA
Foxp3
CD8
IFN-γ
CD4
F
The number of COL3A1⁺ CAFs/HP
The number of Treg/HP
The number of CD8⁺_IFNG/HP
CR
non_CR
G
fluorouracil_K24844714
doxorubicin_K92093830
carboplatin_K11626735
tamoxifen_K93754473
paclitaxel_A28746609
doxorubicin_M01915239
docetaxel_A05821830
carboplatin_M63575423
tumor^resist
CAF_COL3A1^high
CAF_COL3A1^low
tumor^sen
Correlation
negtive
positive
Rho

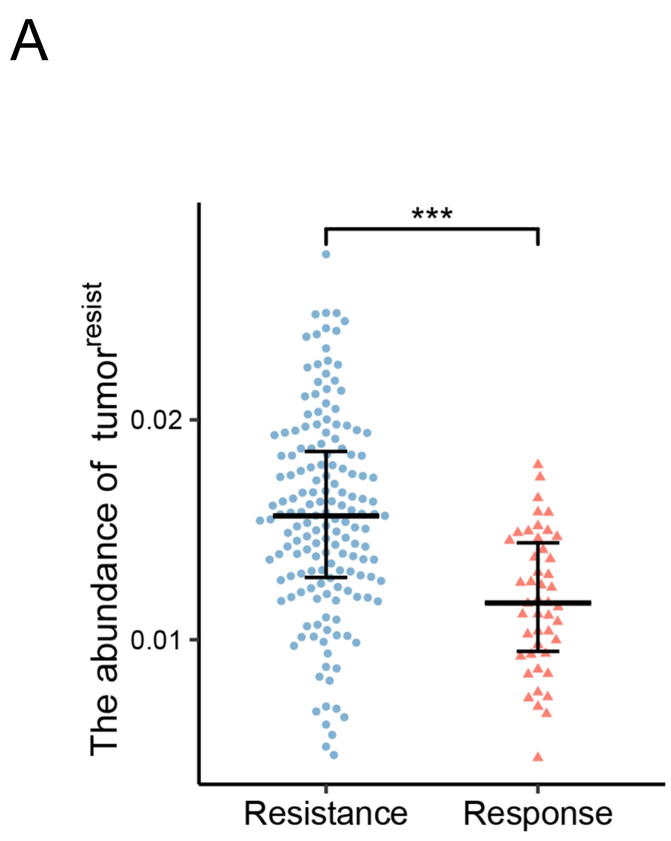
A
***
The abundance of tumor^resist
0.02
0.01
Resistance
Response

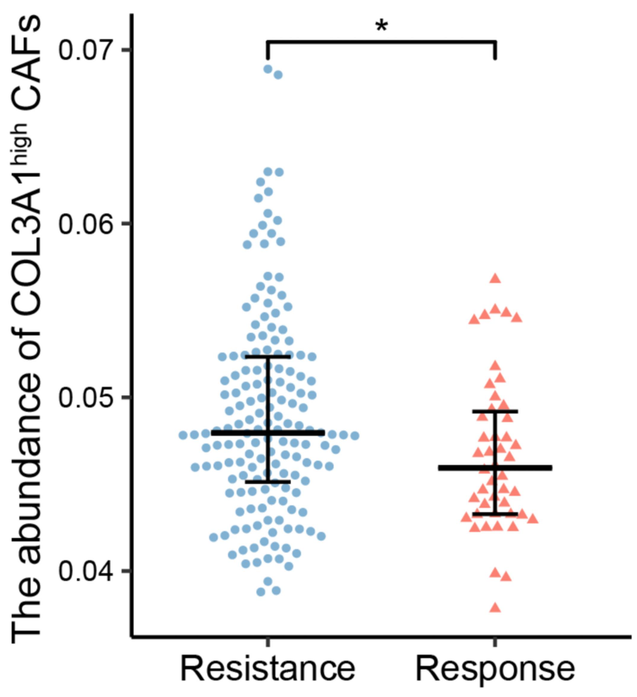
C
*
The abundance of COL3A1^high CAFs
0.07
0.06
0.05
0.04
Resistance
Response

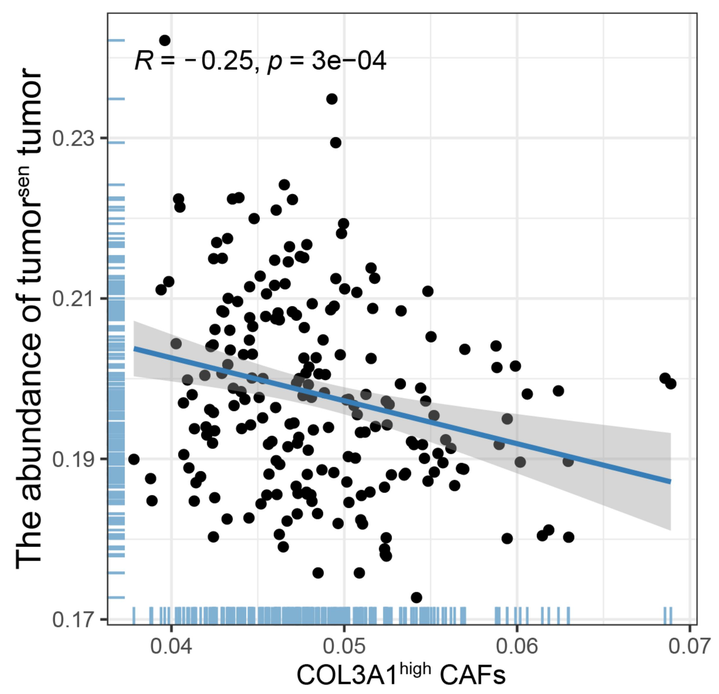
E
R = −0.25, p = 3e−04
The abundance of tumor^sen
0.23
0.21
0.19
0.17
0.04
0.05
0.06
0.07
COL3A1^high CAFs

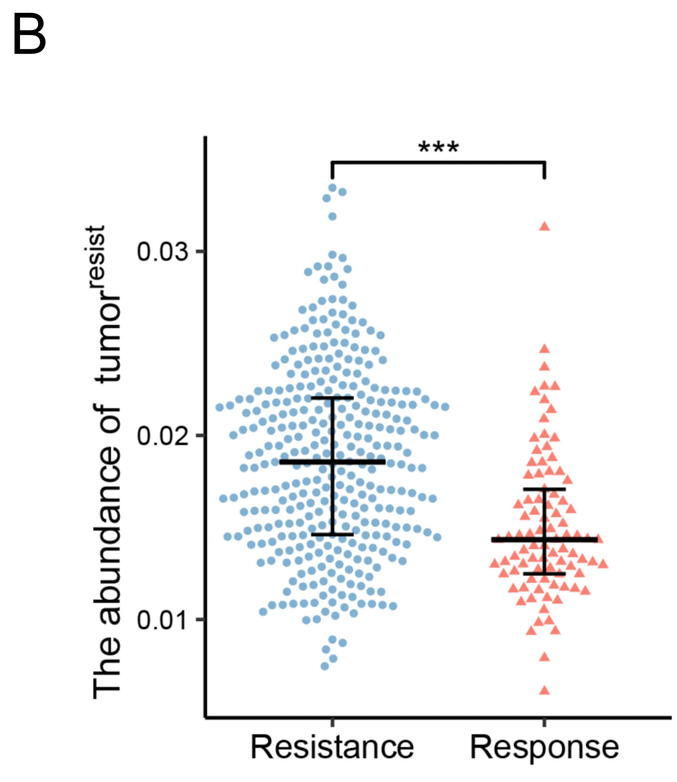
B
***
The abundance of tumor^resist
0.03
0.02
0.01
Resistance
Response

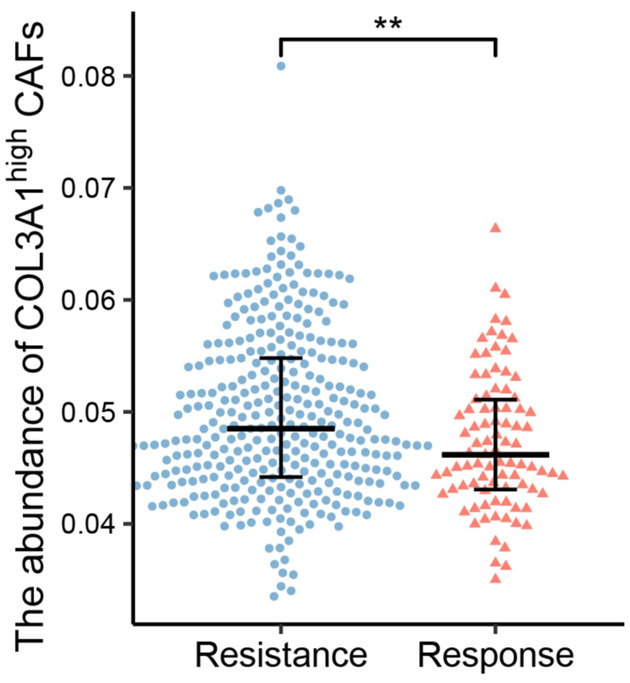
D
**
The abundance of COL3A1^high CAFs
0.08
0.07
0.06
0.05
0.04
Resistance
Response

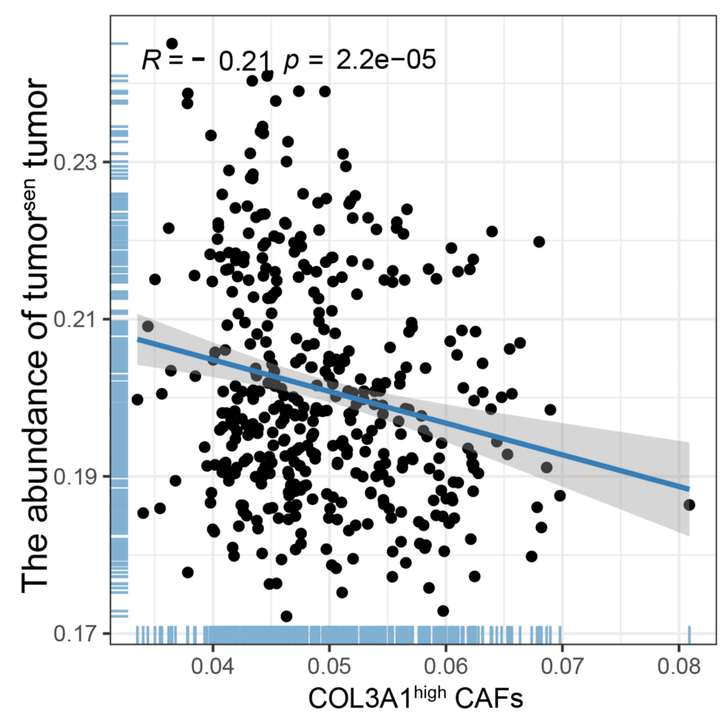
F
R = −0.21 p = 2.2e−05
The abundance of tumor^sen
0.23
0.21
0.19
0.17
0.04
0.05
0.06
0.07
0.08
COL3A1^high CAFs

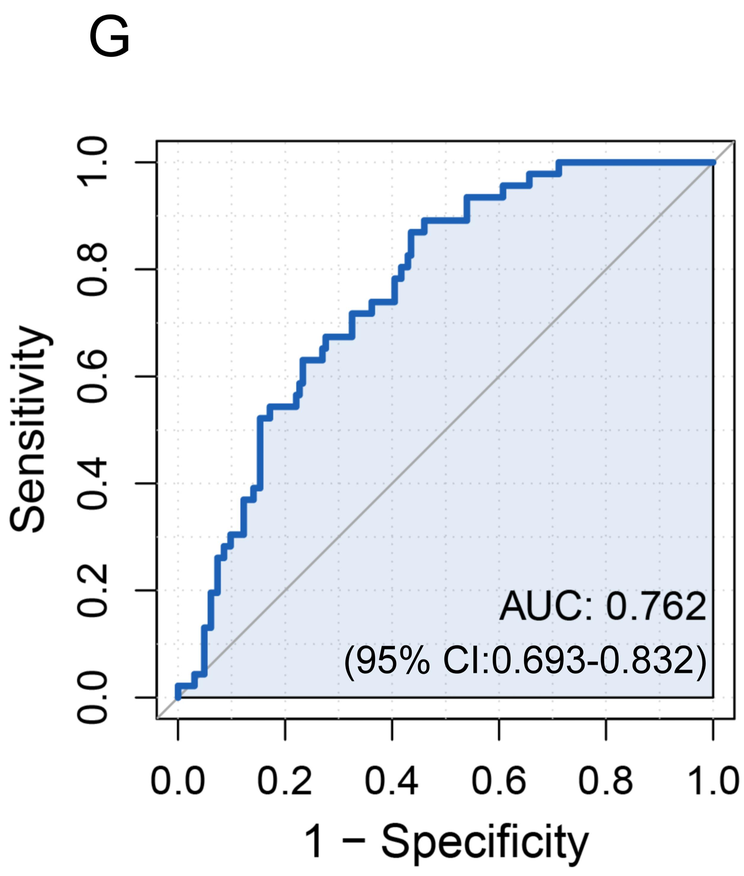
G
Sensitivity
1 − Specificity
AUC: 0.762
(95% CI:0.693-0.832)

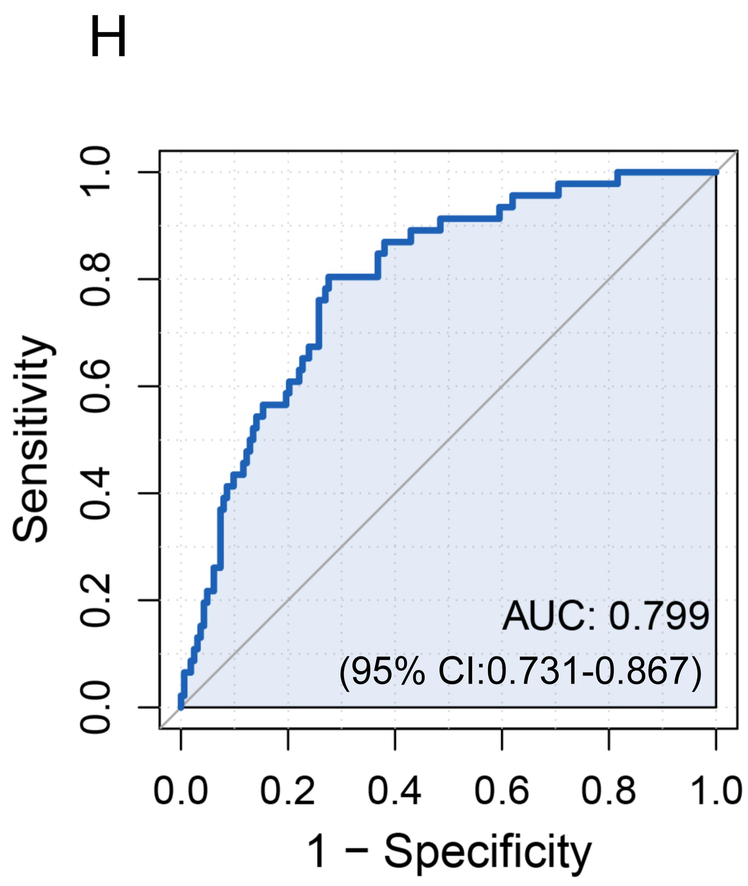
H
Sensitivity
1 − Specificity
AUC: 0.799
(95% CI:0.731-0.867)

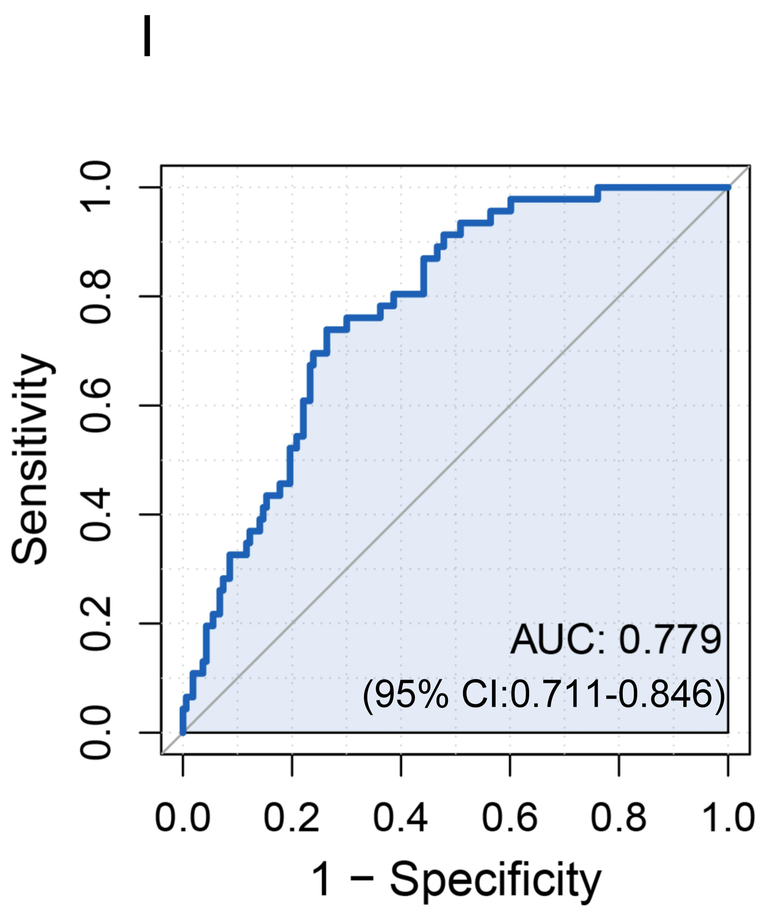
I
Sensitivity
1 − Specificity
AUC: 0.779
(95% CI:0.711-0.846)

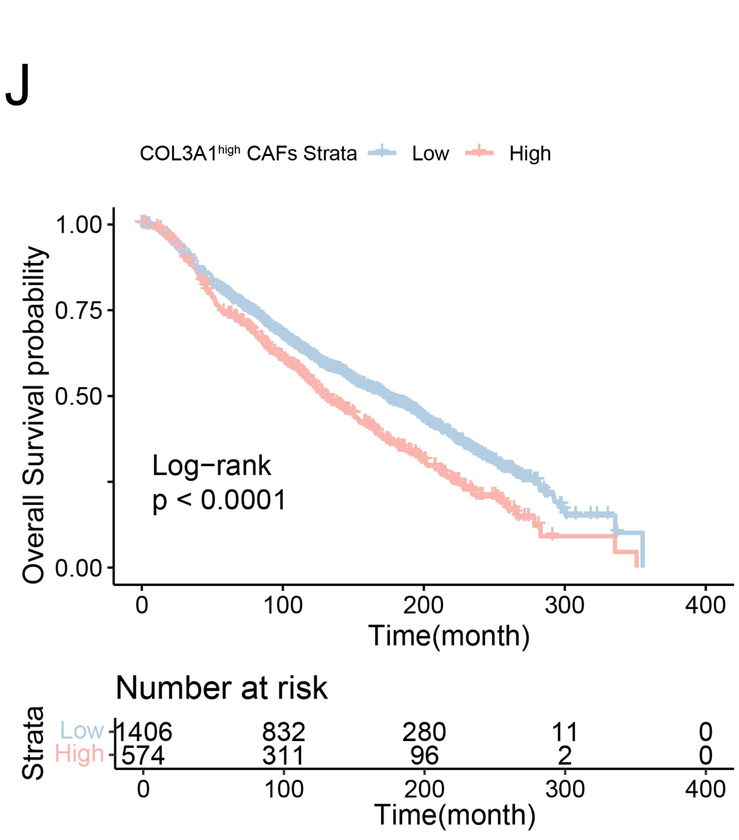
J
COL3A1^high CAFs Strata Low High
Overall Survival probability
Log−rank
p < 0.0001
Time(month)
Number at risk
Strata
Low 1406 832 280 11 0
High 574 311 96 2 0
Time(month)

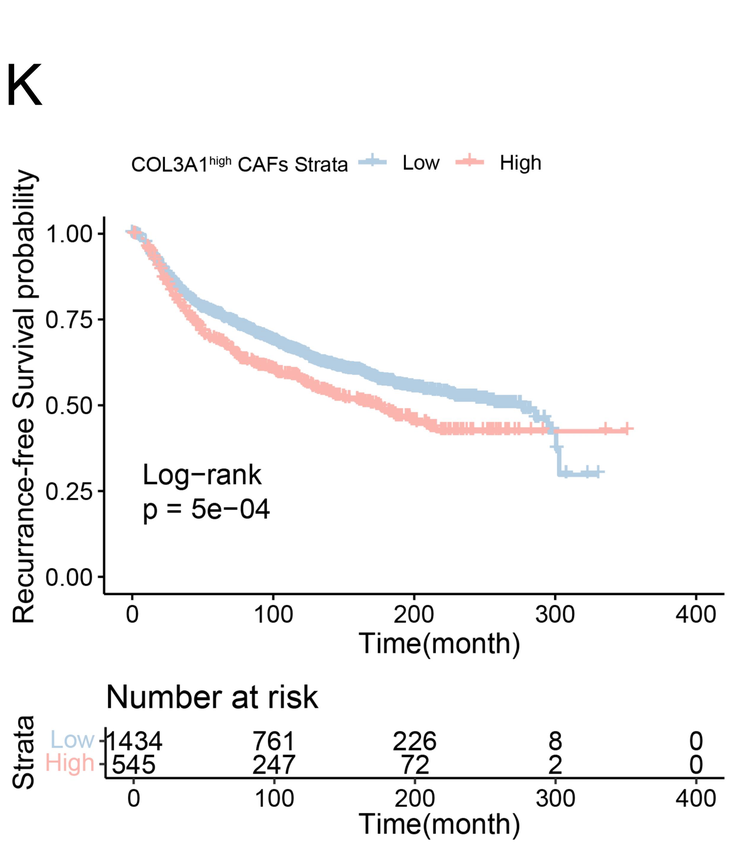
K
COL3A1^high CAFs Strata Low High
Recurrance-free Survival probability
Log−rank
p = 5e−04
Time(month)
Number at risk
Strata
Low 1434 761 226 8 0
High 545 247 72 2 0
Time(month)

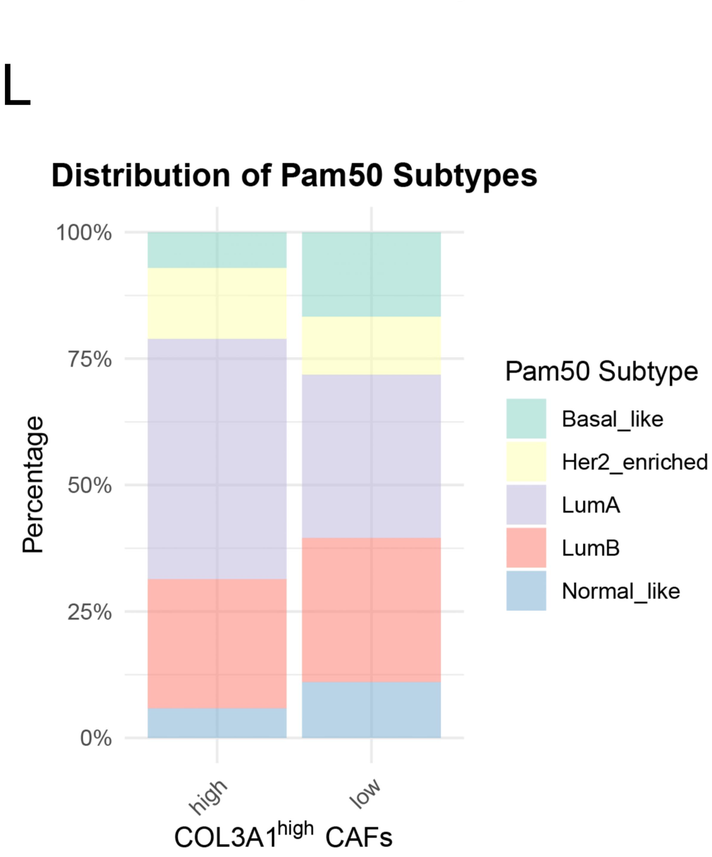
L
Distribution of Pam50 Subtypes
Percentage
100%
75%
50%
25%
0%
high
low
COL3A1^high CAFs
Pam50 Subtype
Basal_like
Her2_enriched
LumA
LumB
Normal_like

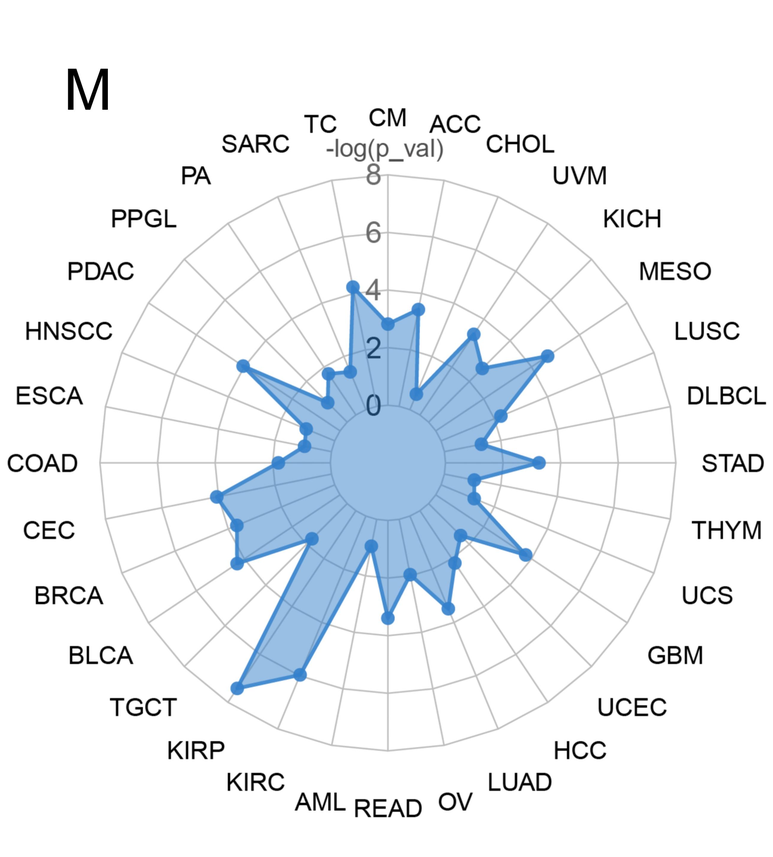
M
-log(p_val)
CM
ACC
CHOL
UVM
KICH
MESO
LUSC
DLBCL
STAD
THYM
UCS
GBM
UCEC
HCC
LUAD
OV
READ
AML
KIRC
KIRP
TGCT
BLCA
BRCA
CEC
COAD
ESCA
HNSCC
PDAC
PPGL
PA
SARC
TC

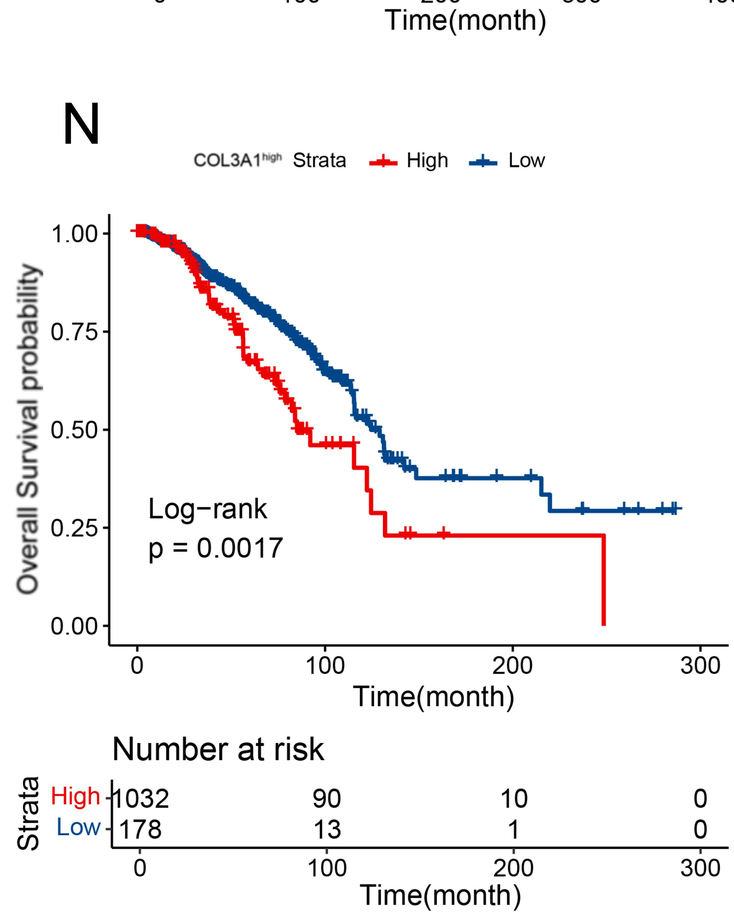
N
COL3A1^high Strata High Low
Overall Survival probability
Log−rank
p = 0.0017
Time(month)
Number at risk
Strata
High 1032 90 10 0
Low 178 13 1 0
Time(month)

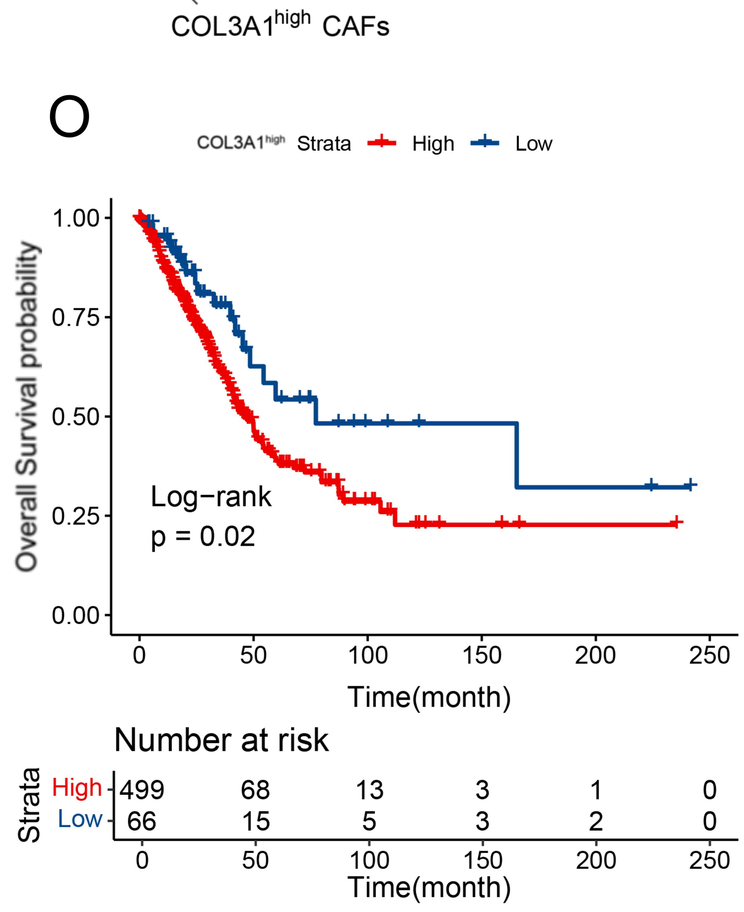
O
COL3A1^high Strata High Low
Overall Survival probability
Log−rank
p = 0.02
Time(month)
Number at risk
Strata
High 499 68 13 3 1 0
Low 66 15 5 3 2 0
Time(month)

A

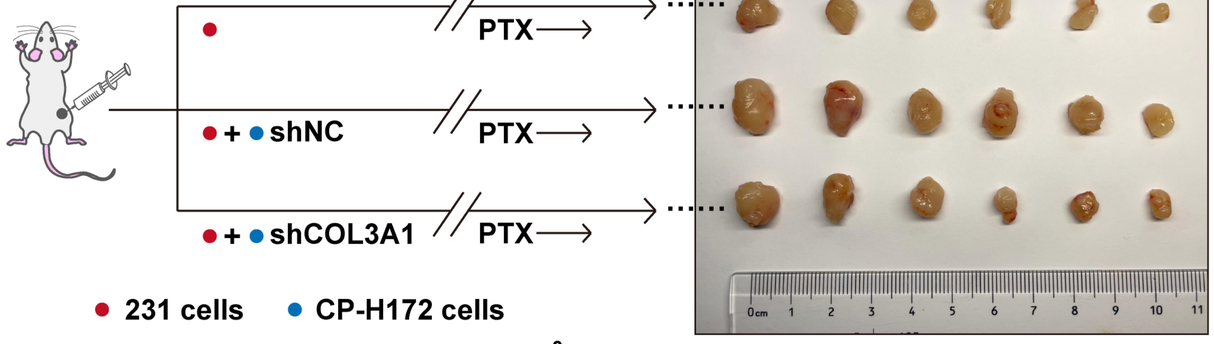

B

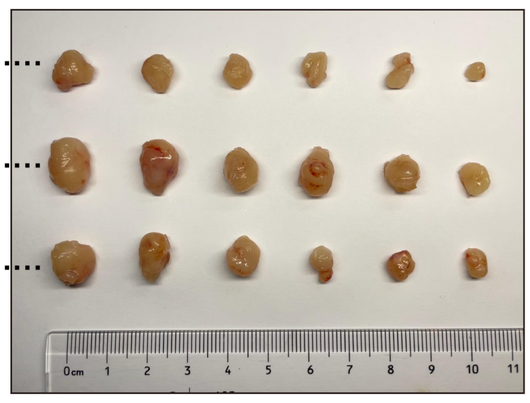

C

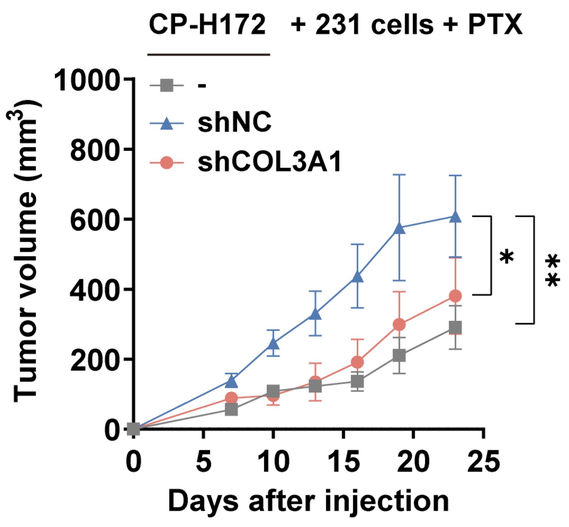

D

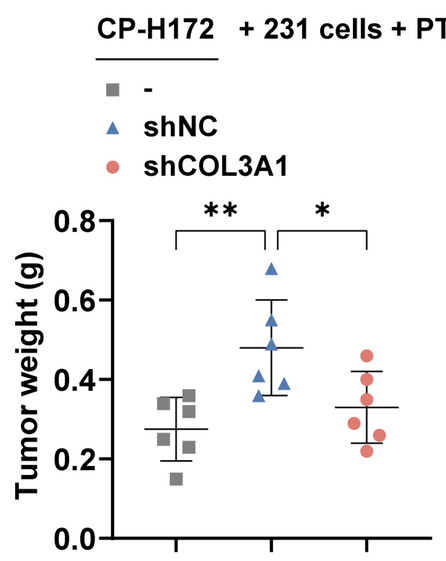

E

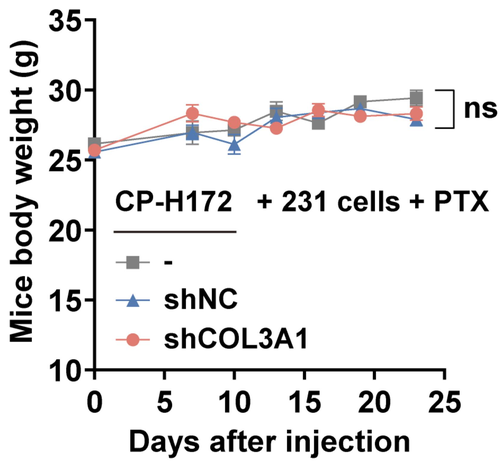

F

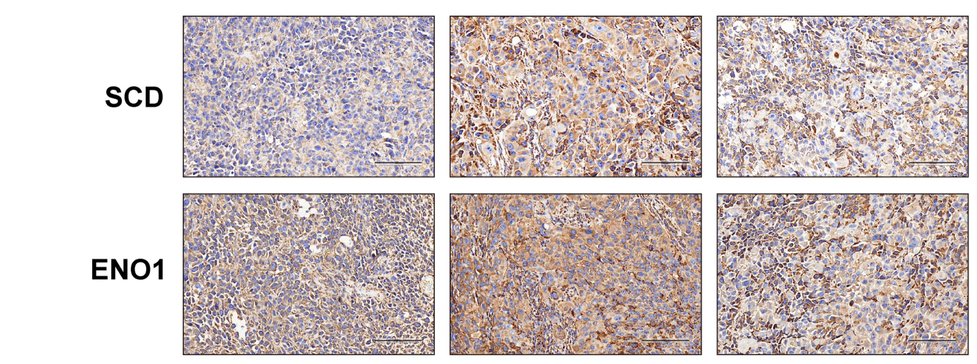

G

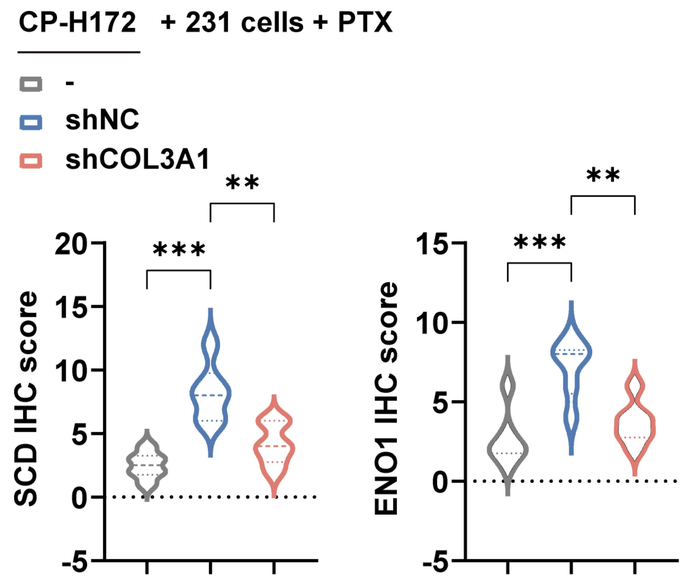

H

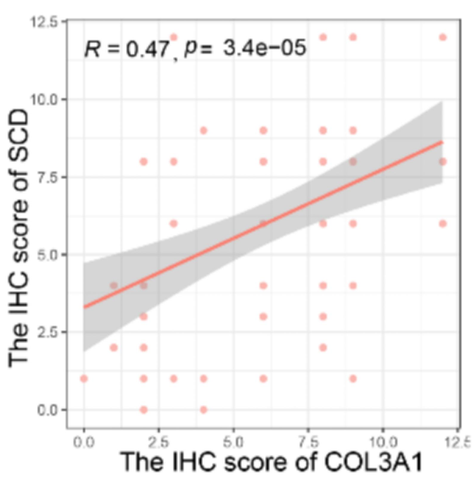

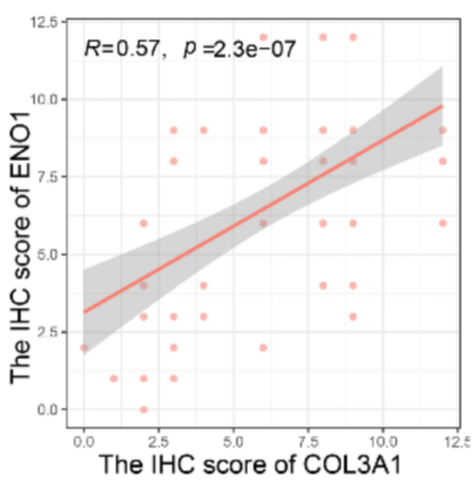

I

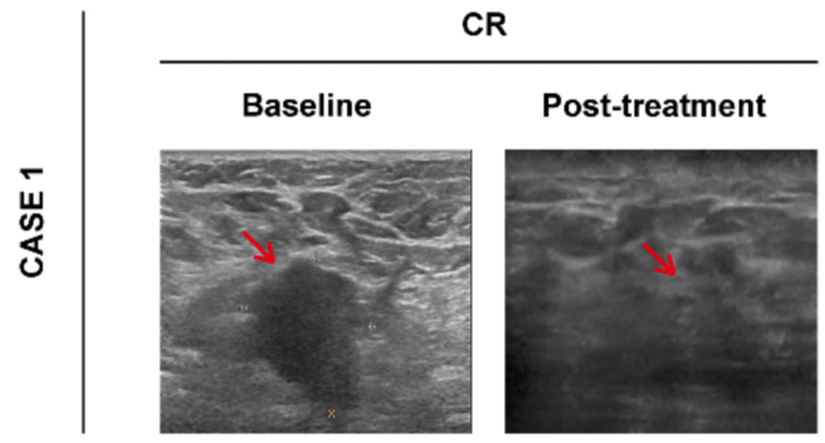

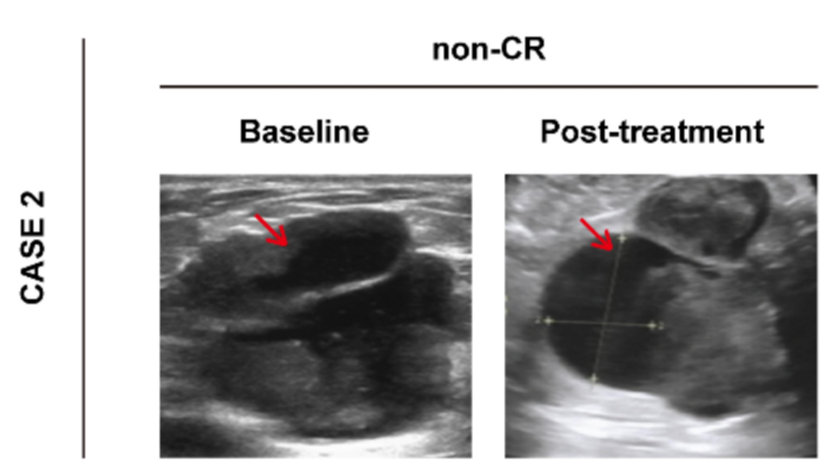

J

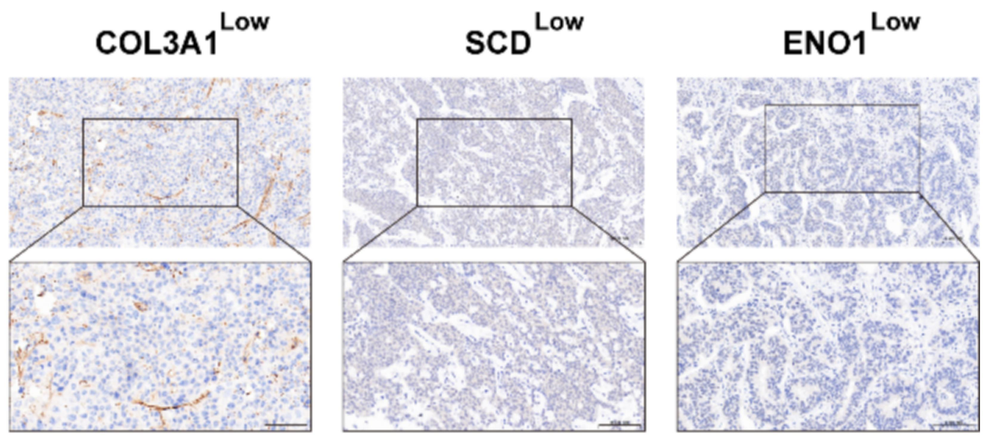

K

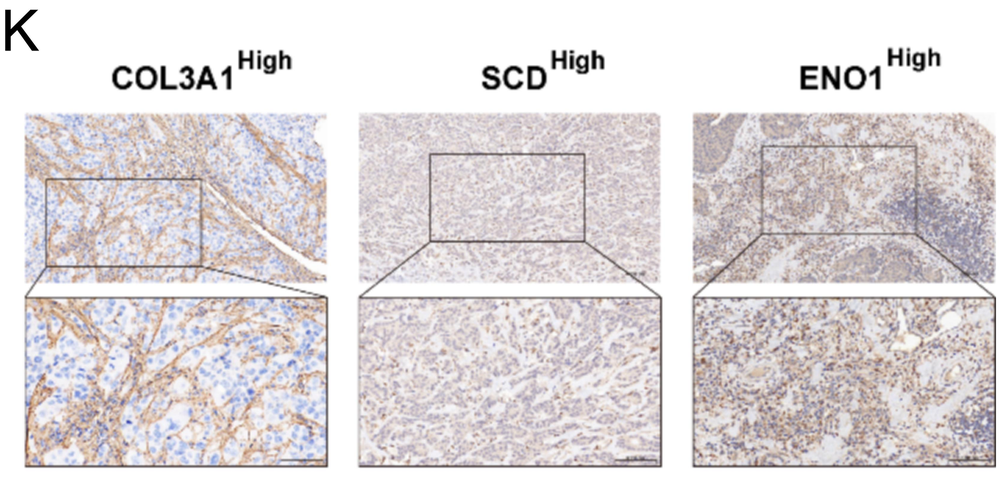

L

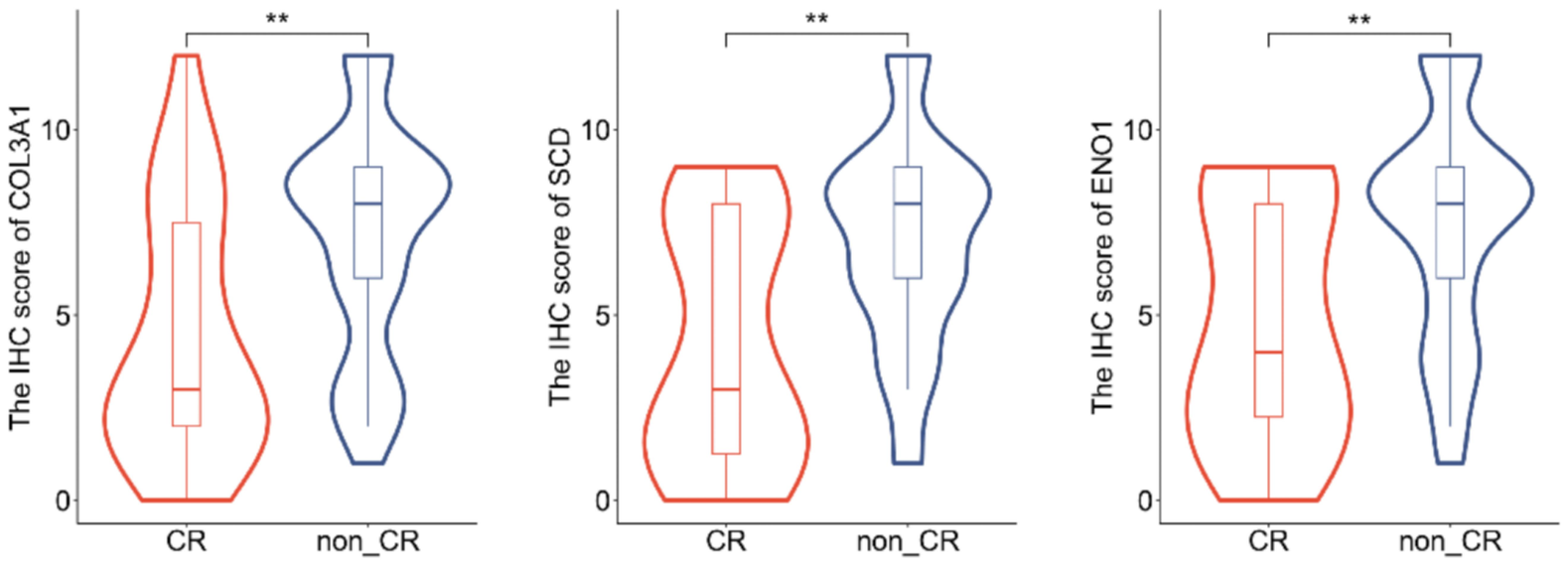

M

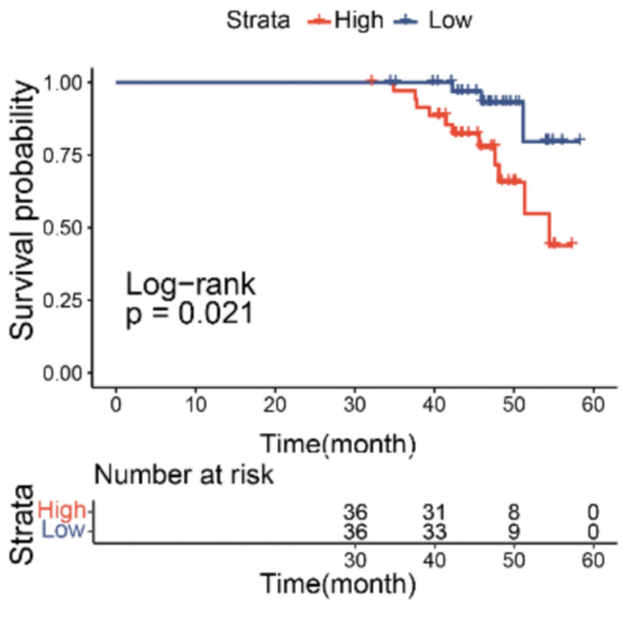

Exploration

bulk RNAseq

Breast cancer

scRNAseq

Spatial transcription

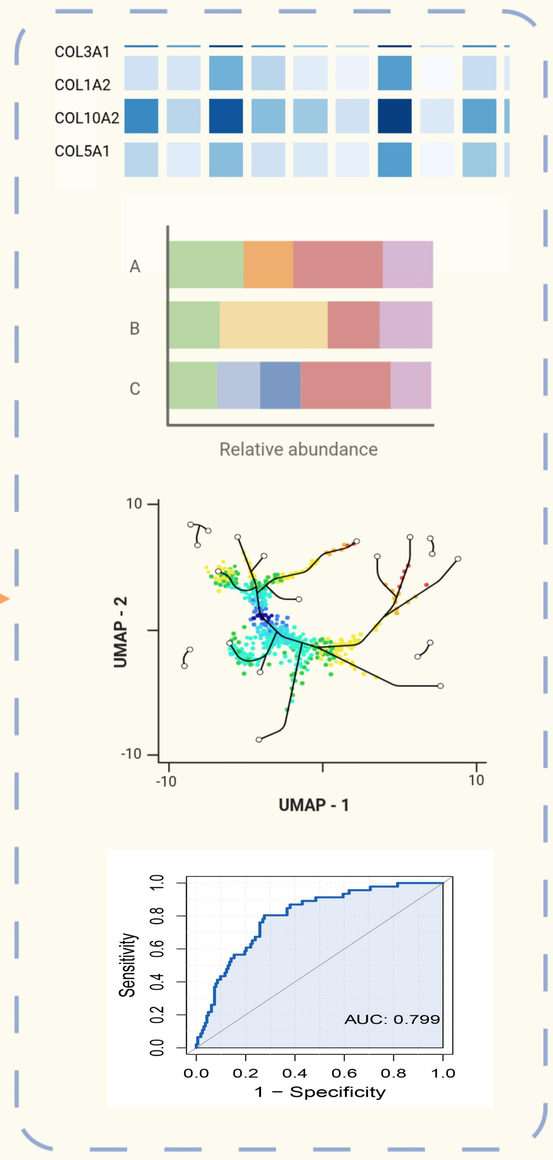

Validation

cell

mouse

Clinical corhart

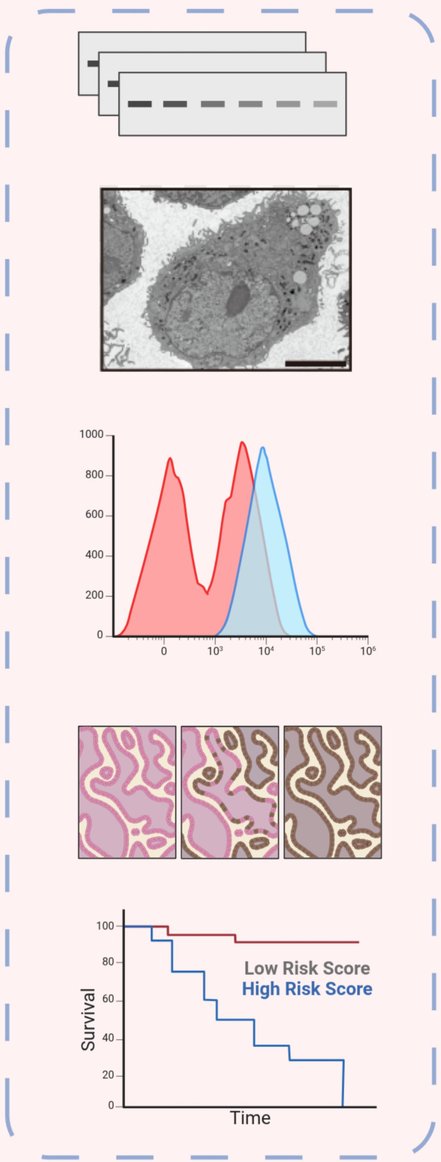

Molecular Mechanism